

UNIVERSITY OF OKLAHOMA

GRADUATE COLLEGE

MAGNETO-EXCITON AND STRAIN STUDIES

IN InSb QUANTUM WELLS

A Dissertation

SUBMITTED TO THE GRADUATE FACULTY

in partial fulfillment of the requirement for the

Degree of

DOCTOR OF PHILOSOPHY

By

TAROSHANI D. KASTURIARACHCHI

Norman, Oklahoma

2006

UMI Number: 3242293



UMI Microform 3242293

Copyright 2007 by ProQuest Information and Learning Company.
All rights reserved. This microform edition is protected against
unauthorized copying under Title 17, United States Code.

ProQuest Information and Learning Company
300 North Zeeb Road
P.O. Box 1346
Ann Arbor, MI 48106-1346

MAGNETO-EXCITON AND STRAIN STUDIES
IN InSb QUANTUM WELLS

A DISSERTATION APPROVED FOR THE HOMER L. DODGE DEPARTMENT
OF PHYSICS AND ASTRONOMY

BY

Ryan E. Doezema (advisor)

Michael B. Santos (Co-advisor)

Bruce A. Mason

James P. Shaffer

Zhisheng Shi

Acknowledgements

During my years of pursuing the Ph. D. degree at OU, I have had the pleasure to meeting many wonderful people. Without them, my stay here would have been far less enjoyable. So, I would like to thank many people who have made this thesis work a learning and enjoyable experience.

First and foremost, I would like to express my gratitude towards my thesis advisors, Prof. Ryan Doezema and Prof. Michael Santos, for all the advice, support, patient guidance and encouragement during my research. Thank you for your friendship and being wonderful teachers. It was a great pleasure working with you two.

I am very grateful to my committee for their suggestions and encouragement. I am grateful to the all members of the department, faculty and staff for helping me in many different ways.

I would also like to acknowledge post docs and my fellow graduate students, Ning Dai, Xinhui Zhang, Giti Khodaparast, Fred Brown, Robert Meyer, Niti Goel, Madhavi Edirisooriya, Thushari Jayasekera and William Gempel, who I worked with and who provided samples for this work.

I would like to thank the machine shop staff, Joel Young, Bob Littell and Berry Bergeron, for helping to design and make the experimental setup. I will always appreciate Adrienne Wade for her kindness whenever I needed help.

I have shared so much fun and good times with my friends in Norman, that I cannot mention them all by names. I am thankful to all of them and wish them the best of luck.

I am thankful to my parents and brothers for their encouragement, support and prayers throughout my education. They have always encouraged me, and supported me in all undertakings. Gratitude is also expressed to other members of my family who encouraged me during this time.

Finally, I wish to express my appreciation to my husband, Lalith, for his constant encouragement, spiritual support and sacrifices. The completion of seven years of hard work would not be possible without his support. One of the best experiences that we have had in this period was the birth of our son Thisara. He provided perpetual love that helped me in overcoming out frustrating moments during my Ph.D. research. Thank you for being a very good boy and giving me so much joy and a true meaning to my life.

List of Contents

Acknowledgements.....	iv
List of Contents.....	vi
List of Figures.....	ix
List of Tables.....	xiii
0 Introduction	1
1 Background and Theoretical Considerations.....	4
1.1 Introduction.....	4
1.2 Crystal Structure.....	6
1.3 Energy Gap.....	7
1.4 Semiconductor Quantum Wells.....	10
1.5 Theoretical Foundations.....	13
1.6 Sub-bands in undoped Quantum Wells.....	19
1.6.1 Subband Energies for $k_t = 0$	19
1.6.2 Subband Energies for $k_t \neq 0$	20
1.7 Luttinger Model.....	23
2 Excitons in quantum wells.....	25
2.1 The Concept of an Exciton.....	25
2.2 Excitons in Semiconductor Quantum Wells.....	29
2.2.1 Ideal 3D and 2D Excitons.....	29
2.3 Two-Dimensional Hydrogen Model.....	31
2.4 Effect of a Perpendicular Magnetic Field.....	35
2.4.1 Free Carriers.....	35
2.4.2 Excitons in Magnetic Field.....	37

3	Experimental Methods.....	40
3.1	Quantum Well Structure.....	40
3.2	Fourier Transform Infrared Spectroscop(FTIR).....	42
3.2.1	The Basics of FTIR: How the Device Operates.....	42
3.2.2	The Spectrometer.....	46
3.2.3	Multi-Reflection Interference in InSb/AlInSb Quantum Wells.....	50
3.3	Sample Preparation.....	52
3.4	Spectroscopic Derivative.....	53
3.5	Magneto-Optics Experiment Setup.....	56
3.5.1	Spectrometer and FTIR External Light Pipe.....	56
3.5.2	The Superconducting Magnet.....	59
3.5.3	Cooling Down the System.....	60
3.5.4	Warming Up the System.....	61
3.5.5	Detector.....	62
4	High Resolution X-Ray Diffraction (HRXRD).....	64
4.1	Types of HRXRD Scans.....	65
4.2	Determination of Aluminum Composition.....	67
4.2.1	Al Composition from symmetric measurements.....	69
4.2.2	Al Composition from Asymmetric Measurements.....	73
4.3	Determination of Aluminum Concentration using Alloy Gap.....	78
5	Determination of Strain Parameters.....	82
5.1	Strain Effects on the Band Alignment.....	82
5.2	Deformation Potentials.....	86
5.3	Samples.....	91
5.4	Determination of Deformation Potential Parameters (Method of Analysis).....	95

6	Excitons in magnetic fields: Magnetoexcitons.....	105
6.1	Introduction.....	105
6.2	Magnetic Field Limit: Are we in the High-Field or Low-Field Limit?.....	106
6.3	Experiment.....	108
6.4	Magnetoexciton Transitions.....	111
6.5	Theoretical Model.....	114
6.6	Selection Rules.....	117
6.7	Theoretical Results.....	119
6.8	Comparison between Theory and Experiment.....	121
6.8.1	Sample (1): S656.....	121
6.8.2	Sample (2):T017.....	128
6.8.3	Sample (3):T015.....	134
6.9	Parabolic Quantum Wells.....	137
6.9.1	Sample: S578.....	139
	Summary and Future Work.....	144
	References.....	146
	Appendix A: Al Composition from HRXRD data.....	151
	Appendix B: Pidgeon and Brown model Hamiltonians.....	155

List of Figures

Figure 1.1: Zincblende Structure	7
Figure 1.2: Simplified band structure for InSb	9
Figure 1.3: Band-gap energy versus lattice constant at 300K.	10
Figure 1.4: Schematic diagram describing the quantum size effect	12
Figure 1.5: The band-edge energies	18
Figure 1.6: Calculated subband dispersion relations of InSb/AlInSb quantum wells using the Bastard formalism.	22
Figure 2.1: The band structure of a semiconductor with a full valence band and empty conduction band.	26
Figure 2.2: Exciton formation results in the existence of new energy states in semiconductor band gap E_g	28
Figure 2.3: Calculated Landau levels energies for the QW of 30nm width	37
Figure 3.1: Typical layer structure of an undoped multiple quantum well.....	41
Figure 3.2: Schematic of a Michelson interferometer.	43
Figure 3.3: A typical interferogram	45
Figure 3.4: Fourier transform of the interferogram in Figure 3.3	45
Figure 3.5: Peak positions of water vapor and carbon dioxide.....	47
Figure 3.6: Block diagram of FTIR. Dash lines show the optical path	49
Figure 3.7: Illustration of multi-reflection interference.....	50
Figure 3.8: Transmission spectra of 5nm, 20% sample (before wedging)	51
Figure 3.9: Transmission spectrum of an InSb/ $Al_xIn_{1-x}Sb$ MQW with Al concentration of 7.6% and well width of 20nm at 30K and 4.2K.	55
Figure 3.10: Differential transmission spectrum of the same sample.....	56
Figure 3.11: Part of Vacuum can/light-pipe assembly	58
Figure 3.12: Top view of the detector unit.	62
Figure 3.13: Schematic of the experimental setup.....	63
Figure 4.1: Experimental set-up for x-ray diffraction.....	65
Figure 4.2: The experimental (004) rocking curve from a 15nm MQW.	71

Figure 4.3: Rocking curves from (-1, -1, 5) measurements.	74
Figure 4.4: Differential transmission spectra of 15nm well	80
Figure 5.1: Lattice distortion in a strained-layer structure.....	84
Figure 5.2: The heavy-hole and light-hole gaps for strain-free and strained InSb at the center of Brillouin zone (Γ point)	88
Figure 5.3: Differential transmission spectra (not normalized) for 20nm samples with different Al concentration	93
Figure 5.4: Differential transmission spectra.....	94
Figure 5.5: Schematic illustration of heavy hole and light hole gaps.....	95
Figure 5.6: Differential transmission spectrum of an InSb/Al _x In _{1-x} Sb MQW	96
Figure 5.7: Theoretical predicted energies of the HH1-CB1 and LH1-CB1 transitions as a function of Al concentration for 20nm well	100
Figure 5.8: Light and heavy hole energy gap values obtained experimentally after the iteration procedure as a function of strain and barrier Al composition ..	102
Figure 5.9: Light and heavy hole energy gap values as a function of barrier Al composition.....	104
Figure 6.3: (a) Raw transmission spectra at B = 0.5T (b) Temperature differential spectra at B = 0.5T	112
Figure 6.4: Magnetoabsorption spectra of InSb/Al _{0.10} In _{0.90} Sb MQW	113
Figure 6.5: Theoretical predictions for the Landau levels in the conduction band of the sample with well width 15nm and 17% Al in the barrier	119
Figure 6.6: Calculated Landau-level structure for heavy holes in the valence band of an InSb/AlInSb QW structure with 15nm wells	120
Figure 6.7: Schematic potential profiles for electrons, heavy holes and light holes in a 5nm well.....	121
Figure 6.8: Experimental transition energies(points) for sample S656 (5nm well width) plotted against the magnetic field.....	123
Figure 6.9: Experimental magneto-absorption spectra of sample S656 for various magnetic fields	124
Figure 6.10: A series of transmission traces as a function of magnetic field..	125

Figure 6.11: Magnetoexciton spectral line positions in samples S1 and S2.....	127
Figure 6.12: The evolution of the exciton states under applied magnetic field.....	129
Figure 6.13: Observed spectra from a MQW sample of 15nm well width and 10% Al in the barrier for magnetic fields from 3.5T to 6.5T at 4.2K.	130
Figure 6.14: Comparison between the calculated (solid lines) and the experimental transition energies	132
Figure 6.15: Experimental magneto-absorption spectra of sample T017 for various magnetic fields	133
Figure 6.16: The experimental peak positions as a function of magnetic field for the sample with well width 15nm and 17% Al in the barrier.	135
Figure 6.17: Comparison between the calculated (solid lines) and the experimental transition energies	136
Figure 6.18: Schematic of the potential energy profile of a Parabolic QW	139
Figure 6.19: Differential spectrum measured on parabolic QW of width 500Å and 9% Al in the alloy layer at B = 0T	140
Figure 6.20: Circular marks represent the energy of the peak position from transmission spectra	142
Figure 6.21: Transmission spectra for the PQW sample at various magnetic fields. Spin splitting can be clearly seen.....	143

List of Tables

Table 1.1: Room temperature data comparing some parameters of InSb with other commonly use III-V semiconductors	6
Table 4.1: Barrier heights for 15nm quantum wells with different Al composition...	68
Table 4.2: Lattice parameters and Al compositions obtained from (004) x-ray measurement for 10 nm MQW samples	72
Table 4.3: Lattice parameters and Al compositions obtained from (-1-15) x-ray measurement for 20 nm MQW samples.	77
Table 4.4: Values of InSb gap and E_g' at 4.2,77 and 300K.....	79
Table 5.1: Hydrostatic and Shear deformation potential parameters for some selected semiconductors	91
Table 5.2: Comparison of theoretically calculated transition energies with experimentally observed transition energies.....	97
Table 5.3: Calculated electron and hole (heavy and light) subband confinement energies for 15nm well width samples.....	99
Table 6.1: Comparison between different characteristic parameters for the Hydrogen atom, GaAs and InSb.	107

Chapter 0

Introduction

With the availability of mature epitaxial growth technologies, such as molecular beam epitaxy (MBE), it is now possible to grow high-quality layers and heterostructures with controlled thicknesses and sharp interfaces. The fabrication of low-dimensional semiconductor heterostructures has opened a whole range of exciting new perspectives in the development of novel devices and the investigation of quantum-mechanical effects. Furthermore, rapid advancements in epitaxial growth technologies have made possible new kinds of III-V quantum wells that are very attractive for the investigation of unique physical phenomena and for the fabrication of optoelectronic devices. The first step toward understanding the optoelectronic properties of a quantum well device is to investigate the quantum confined electron and hole states in the well. In these studies one can obtain further insight by making use of perturbations such as a magnetic field or the strain in lattice-mismatched quantum wells.

InSb is a narrow gap III-V semiconductor. Among the III-V semiconductors, electrons in InSb have the smallest electron effective mass ($0.014m_0$), largest g factor (-51) and the strongest spin-orbit coupling effects. There have been many efforts devoted to the development of InSb-based devices. The small effective mass leads to a high mobility at room temperature and, consequently, a high sensitivity for Hall sensors[1] and geometrical magnetoresistors[2] made from InSb epilayers.

Mesoscopic magnetoresistors and Hall devices made from InSb quantum wells (QWs) are being developed for use as read heads in ultra-high density hard drives [3] and other applications [4].

The Coulomb interaction between electrons and holes in a semiconductor leads to the formation of excitons. It is well known that the optical properties of semiconductor heterostructures close to the band gap are strongly determined by excitons. The exciton energy is just below the band gap, and it is interesting to study the formation and properties of excitons. We use excitons as a tool to probe various material and structural properties in InSb quantum wells.

This thesis is divided into six chapters and contains the following subjects. In chapter one, we introduce some fundamental concepts and theoretical background, which form the basis for an understanding of the rest of the chapters.

In chapter two, the concept of excitons and their basic properties are introduced. We start with a description of the formation of excitons. Basic properties of excitons in bulk and in quantum wells are considered next. The two-dimensional hydrogen model is introduced. Finally, the effect of a magnetic field on both the free carriers and excitons are presented. The emphasis is on familiarizing the reader with the concepts that will be used through the rest of the thesis.

Chapter three describes the InSb quantum well structure, sample preparation and experimental techniques. Then, a brief description of Fourier Transform spectroscopy is made and the schematic diagram of the FTIR spectrometer as well as related components is given.

In chapter four, the High-Resolution X-ray Diffraction (HRXRD) technique is explained. A detailed discussion on obtaining in-plane and out-of-plane lattice constants using symmetric and asymmetric measurements is also given.

A major obstacle in growing thin films of one semiconductor on another is the lattice mismatch between materials. The lattice parameter mismatch between epilayer and substrate introduces strain. Chapter five explains the study of strain-related material parameters in the strained and nonparabolic InSb /Al_xIn_(1-x)Sb quantum well system. More specifically, a detailed discussion on determining deformation potential parameters using the different strain dependence of the light-and heavy-hole band gaps is given.

Valuable information about the excitons and the carriers confined in the quantum well system can be obtained from optical spectra perturbed by an external magnetic field. In the high field limit, where the cyclotron energy is higher than the exciton binding energy, the magnetic confinement dominates and a Landau-level-like structure is expected to occur. Furthermore, the magnetic field removes the spin degeneracy and gives rise to a splitting of the states. Chapter six investigates optical properties of InSb-AlInSb layered structures in a normal magnetic field. The study leads to an interpretation of the optical transitions in InSb MQW samples. We outline a theory of magneto-optical spectra of valence-to-conduction band transitions in undoped InSb quantum wells.

Finally; we give some conclusions and propose possible ways and methods to continue our investigations.

Chapter 1

Background and Theoretical Considerations

The purpose of this chapter is to review the basic properties of InSb: the material we used in this study and to provide the theoretical background. The first half of the chapter explains the fundamental concepts necessary to understand the low dimensional heterostructures and the second half of the chapter describes the k.p method for calculating the band structure. Concentrating on single InSb/AlInSb quantum wells (QW), we outline the main features of their band structure and introduce the QW subbands as discrete energy levels for the electrons and holes.

1.1 Introduction

Semiconductor nanostructures have received much attention from chemists and physicists in the last decade due to the fact that their electrical and optical properties can be very different from those of bulk semiconductor crystals. The optical and electrical properties of semiconductor nanostructures can be tailored to a large extent by the dimensions of the crystals. The various effects that occur due to spatial confinement of electrons in such structures are of scientific importance. In addition, semiconductor nanostructures are very promising for a number of applications in the opto-electronic industry.

There have been numerous efforts devoted to the development of InSb-based devices. Electrons in InSb have interesting properties that are advantageous for transport device applications. Among III-V semiconductors, InSb has the smallest electron effective mass ($0.014m_0$), largest g-factor (-51), strongly nonparabolic dispersion relation of electrons and the strongest spin-orbit coupling effects. The small effective mass leads to a high mobility at room temperature and, consequently, a high sensitivity for Hall sensors [1] and geometrical magnetoresistors [2] made from InSb epilayers. Mesoscopic magnetoresistors and Hall devices made from InSb quantum wells (QWs) are being developed for use as read heads in ultra-high density hard drives [3] and other applications [4]. Recently Intel and QinetiQ announced InSb QW field-effect transistors with a gate length of 200nm and a high frequency performance equivalent to Si transistors but with 5-10 times lower active power dissipation [5]. The strong spin-orbit coupling effect is evident in low-temperature experiments on InSb quantum wells (QWs), which have demonstrated a strong Rashba effect in asymmetric structures [6] and spin-dependent scattering from the boundaries of mesoscopic structures [7]. Also with the narrowest energy gap among the III-V semiconductors, InSb makes a good candidate for mid-infrared device applications. Table 1.1 lists room temperature values of some parameters for GaAs, GaSb, InAs, and InSb [8].

	GaAs	InAs	GaSb	InSb
Energy gap (eV)	1.424	0.350	0.726	0.17
Lattice constant (Å)	5.653	6.058	6.096	6.479
Effective mass (m^*/m_e)	0.063	0.023	0.041	0.014
Spin-orbit split off energy (eV)	0.34	0.41	0.8	0.8
Intrinsic mobility (cm^2/Vs)	9000	39000	3000	77000
Dielectric constant (ϵ/ϵ_0)	12.9	15.1	15.7	16.8
Lande g-factor	-0.44	-17.5	-7.8	-50.6

Table 1.1: Room temperature data comparing some parameters of InSb with other commonly use III-V semiconductors [8].

1.2 Crystal Structure

InSb is a III-V material that forms a Zincblende structure. The Zincblende structure consists of two interpenetrating face-centered cubic lattices, one displaced from other by a distance $(a/4, a/4, a/4)$ along the body diagonal. Each indium ($5s^25p$) has 4 antimony nearest neighbors ($5s^25p^3$). The indium forms sp^3 hybridized tetrahedral bonds with its antimony neighbors. The tetrahedral bonds between indium and antimony are shown in the Figure 1.1.

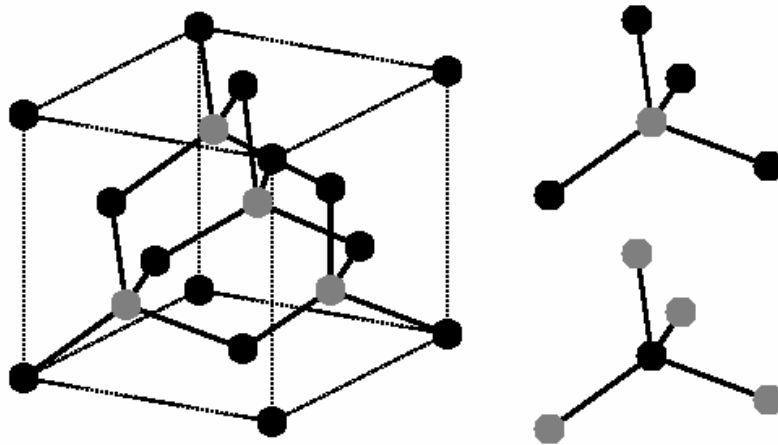


Figure 1.1: Zincblende Structure. The tetrahedral bonds between indium and antimony atom are shown.

1.2 Energy Gap

The ions in a perfect three-dimensional (3D) bulk crystal are arranged in a regular periodic array and thus the electronic structure can be considered as an electron in the presence of a potential with the periodicity of the underlying Bravais lattice. This leads to a description of the electron energy levels as a set of continuous functions having the periodicity of the reciprocal lattice [9]. For semiconductors, this results in the existence of an energy band gap, E_g , between the valence and conduction bands. InSb is a direct gap semiconductor. That means the conduction band edge (the lowest energy position of the conduction band) lies at the same value of wave-vector \mathbf{k} as the valence band edge (the highest energy position of valence band). Figure 1.2 depicts the simplified band structure of InSb at room temperature [8]. The band gap is about

236 meV at 4 K and is about 180 meV at room temperature. Figure 1.3 shows the band gap as a function of the lattice constant for some semiconductors.

The energy band gap tends to decrease as the temperature increases. This behavior can be explained as follows. When temperature increases, the thermal energy increases hence the amplitude of the atomic vibration increases. As a result inter-atomic vibration increases. Because of the thermal expansion of the crystal lattice, inter-atomic spacing increases. An increased inter-atomic spacing decreases the average potential seen by the electron in the material, which in turn reduces the energy gap. The temperature dependence of the energy bandgap, E_g , has been experimentally determined yielding the following expression [10, 11] for E_g as a function of the temperature, T:

$$E_g(T) = E_g(0) - \frac{\alpha T^2}{(T + \beta)}. \quad (1.1)$$

Here α and β are material-dependent parameters.

The variation of energy gap with temperature is linear at high temperature and approximately quadratic at low temperature. This behavior has been observed for many materials. Strain, confinement and alloy composition are the other factors that can affect the values of the energy gap. The effect of strain on the energy gap will be explained in detail in chapter (5).

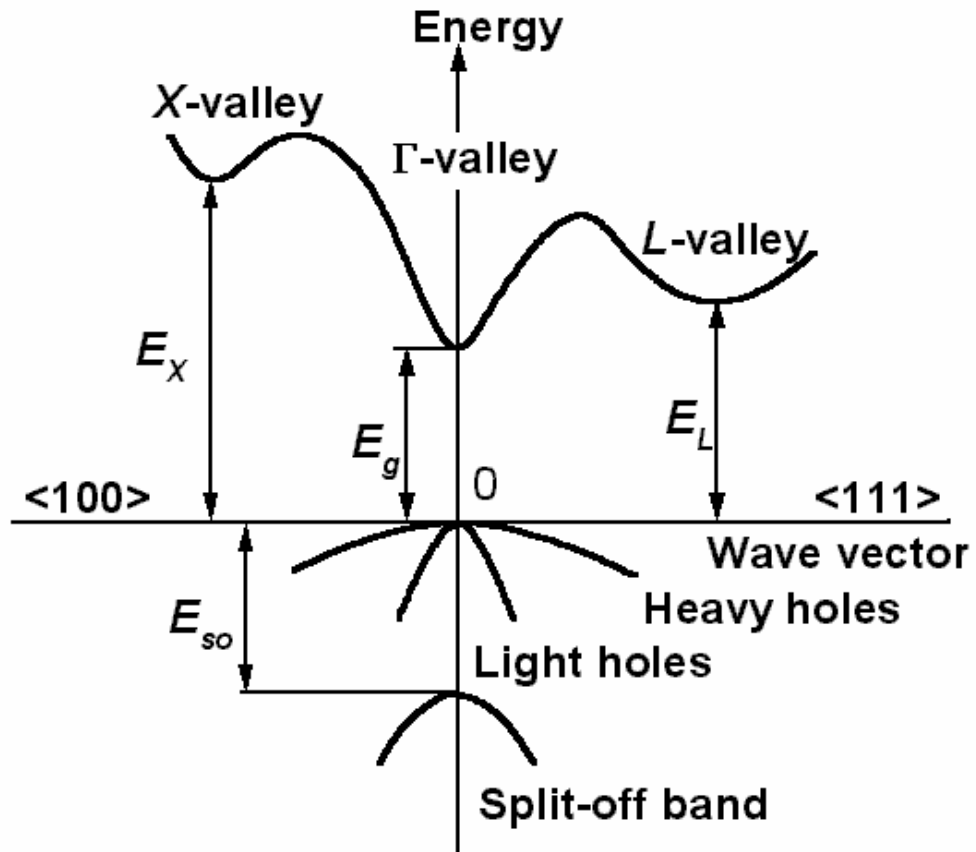


Figure 1.2: Simplified band structure for InSb [8]. $E_g = 0.17\text{eV}$, $E_X = 1.0\text{eV}$, $E_{so} = 0.8\text{eV}$, $E_L = 0.68\text{eV}$.

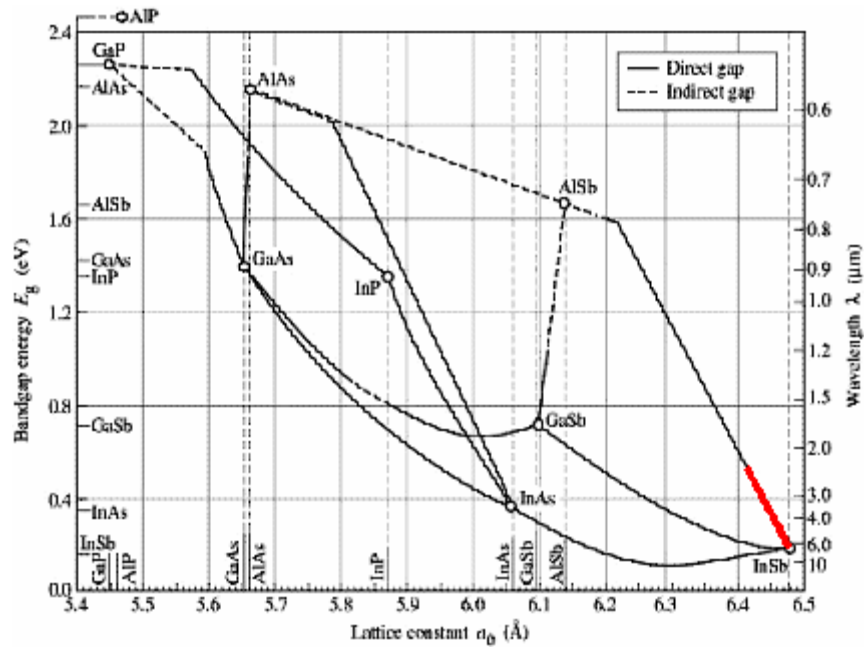


Figure 1.3: Band-gap energy versus lattice constant at 300K for various III-V semiconductors.

1.4 Semiconductor Quantum Wells

The fabrication of low-dimensional semiconductor heterostructures has opened a whole range of exciting new perspectives in the development of novel devices and the investigation of quantum-mechanical effects. All electronic and optical properties of semiconductor devices depend on the band structure. The electronic band structure is modified using basically three closely related concepts: alloying of two or more semiconductors, use of heterostructures to benefit from quantum mechanical confinement effects, and use of built-in strain via lattice-mismatched epitaxy.

A semiconductor quantum well (QW) consists of a thin layer of one type of semiconductor material with a certain band gap energy, sandwiched between two thick layers of another semiconductor material with higher band gap energy [12]. Sandwiching a thin layer of a narrow gap material between two layers of a wide gap material results in type I or type II band alignment of the band edges. If the band alignment is of type I, the thin layer acts as a well for both conduction and valence band. In other words, in type I structures electrons and holes are confined within the same material. In type II structures, the charges are quantized in different materials. A well is regarded as being narrow if its width is less than the electron de Broglie wavelength. In a conduction band well, electrons are confined by a barrier of height equal to the conduction band offset. Similarly, in the valence band, holes may be confined in a quantum well of depth equal to the valence band offset. Energy-band configurations in an InSb/ $\text{Al}_x\text{In}_{1-x}\text{Sb}$ quantum well of 15nm width are depicted schematically in Figure 1.4. In Figure 1.4, V_s and V_p refer, respectively, to the conduction and valence band offsets. The valence band is split into heavy- (HH) and light- (LH) hole bands as a result of the strain arising from the lattice mismatch between the two materials.

By fabricating many such quantum wells (QWs) on top of each other, separated by the barrier material, we construct a multiple quantum well (MQW) structure.

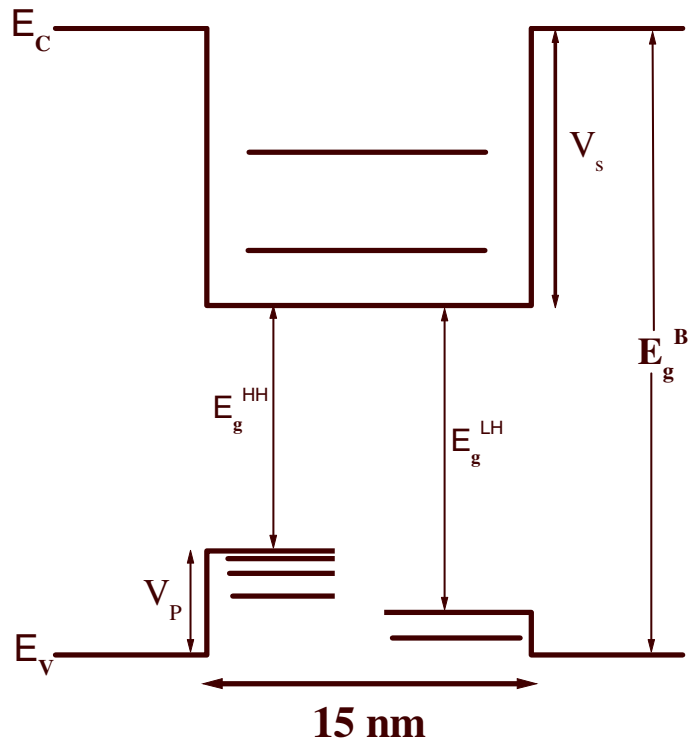


Figure 1.4: Schematic diagram describing the quantum size effect. E_g^{HH} , E_g^{LH} and E_g^B are the band gap of heavy-hole, light hole and barrier layers respectively. The symbols E_c and E_v denote the conduction-and valence-band edges, respectively. Electron, heavy hole and light hole subbands are depicted for 15 nm quantum well.

1.5 Theoretical Foundations

Knowledge of the electronic band structure of a material, or the dependence $E_n(\mathbf{k})$ of the electron energy on the wave vector in various energy bands, is necessary to classify and quantify the electronic and optical properties of a material.

There are many methods for calculating band structure, for example the pseudopotential and tight binding methods. However, most of these methods are computationally complicated.

InSb has a strong non-parabolic band structure. Non-parabolicity in the band structure implies an energy dependent effective mass and g-factor. Kane [13] explained the non-parabolic form of the bands in narrow-gap semiconductors. He used the **k.p** method to calculate the form of conduction and valence bands in the vicinity of the point $\mathbf{k} = 0$ in InSb [13]. The **k.p** method is one of the most useful numerical tools for calculations of semiconductor band structures and has been successfully employed in bulk materials for decades. This method is based on perturbation theory in the vicinity of band extrema and is briefly described below.

In the one-electron approximation the energy spectrum of an electron in a crystal can be explained using the Schrödinger equation:

$$\left[\frac{-\hbar^2}{2m_0} \nabla^2 + V(\vec{r}) \right] \psi(\vec{r}) = E(\vec{k}) \psi(\vec{r}). \quad (1.2)$$

For an electron in a crystal we describe the interaction with core ions by a potential $V(\vec{r})$.

Because of the periodicity of the lattice $V(\vec{r} + \vec{R}) = V(\vec{r})$.

where $\vec{R} = n_1\vec{a}_1 + n_2\vec{a}_2 + n_3\vec{a}_3$, $\vec{a}_1, \vec{a}_2, \vec{a}_3$ are the lattice vectors and n_1, n_2, n_3 are integers.

The Bloch theorem tells us that the solution of the Schrödinger equation associated with the Hamiltonian of the above equation can be written in the form

$$\psi_{n\vec{k}}(\vec{r}) = e^{i\vec{k}\cdot\vec{r}} u_{n\vec{k}}(\vec{r}). \quad (1.3)$$

Here n is the index of the energy band and \vec{k} is the wave vector. $u_{n\vec{k}}(\vec{r})$ has the crystal periodicity. Using the above expression and neglecting the spin-orbit interaction, the Schrödinger equation describing the motion of the electrons becomes

$$\left[\frac{p^2}{2m_0} + \frac{\hbar}{m_0} \vec{k} \cdot \vec{p} + V(\vec{r}) \right] u_{n\vec{k}}(\vec{r}) = \left[E_n(\vec{k}) - \frac{\hbar^2 k^2}{2m_0} \right] u_{n\vec{k}}(\vec{r}). \quad (1.4)$$

Here $\frac{\hbar}{i} \nabla = \vec{p}$ and m_0 is the free electron mass.

Equation 1.4 is the $\mathbf{k} \cdot \mathbf{p}$ Hamiltonian in the absence of spin-orbit interaction and results in a two-band model, which includes the conduction band (CB) and the valence band (VB) [14].

For narrow gap semiconductors, inclusion of spin-orbit coupling is important. Therefore, the two-band model must be extended by introducing spin-orbit coupling, i.e. by taking into account the interaction of the electron with spin $\frac{1}{2}$ moving in the

electric field generated by the underlying lattice. The corresponding band created is referred to as the split-off band. Formally, the spin-orbit interaction is of relativistic origin and can be ultimately written as $\Delta = \lambda l \cdot s$, here λ is a multiplicative constant known as spin-orbit coupling, l is the angular momentum of the charged particle and s is its spin. After some manipulation, one can obtain the spin-orbit interaction term as

$$\frac{\hbar}{4m_0^2c^2}[\nabla V \times \vec{p}] \cdot \sigma$$

Now, with an understanding of the spin-orbit interaction, the **k.p** Hamiltonian with the spin-orbit interaction takes the following form [14]:

$$\left[\frac{p^2}{2m_0} + \frac{\hbar}{m_0} \vec{k} \cdot \vec{p} + V(\vec{r}) + \frac{\hbar}{4m_0^2c^2} [\nabla V \times \vec{p}] \cdot \sigma + \frac{\hbar^2}{4m_0^2c^2} \nabla V \times \vec{k} \cdot \sigma \right] u_{nk}(\vec{r}) = [E_n(\vec{k}) - \frac{\hbar^2 k^2}{2m_0}] u_{nk}(\vec{r}) \quad (1.5)$$

Here σ denotes the Pauli spin matrices. The last term on the left-hand side (k-dependent spin-orbit interaction term) is small compared with the other term.

The secular equation of this Hamiltonian gives [14]

$$E' = 0 \quad (1.6)$$

$$E'(E' - E_g)(E' + \Delta) - k^2 P^2 (E' + 2\Delta/3) = 0. \quad (1.7)$$

Here $E' = E - \frac{\hbar^2 k^2}{2m_0}$ and Δ is the split-off energy.

Equation (1.7) gives three solutions. Since k^2 is very small, the second term can be neglected.

$$E' = 0, E' = E_g, \text{ and } E' = -\Delta.$$

These solutions assume the top of the valence band as zero point energy. Inclusion of spin-orbit interaction removes the degeneracy in the valence band resulting in heavy-hole, light-hole and the split-off bands. The typical band structure near the band edges is shown in Figure 1.5. The parameter P is a measure of the coupling between the conduction band and the valence band, which is given by

$$P = -i \frac{\hbar}{m_0} \langle S | p_z | Z \rangle. \quad (1.8)$$

This matrix element is usually expressed in terms of energy as $E_p = \frac{2m_0}{\hbar^2} P^2$.

Reported values of E_p for InSb ranges from 23.2 to 24.4 ± 0.6 eV [11, 15, 16].

Expanding the above secular equation in small values of k leads to the following parabolic dispersion relations (energy vs. wave vector):

$$E_{CB} = E_g + \frac{\hbar^2 k^2}{2m_0} + \frac{k^2 P^2 (E_g + 2\Delta/3)}{E_g (E_g + \Delta)} \quad (1.9)$$

$$E_{HH} = \frac{\hbar^2 k^2}{2m_0} \quad (1.10)$$

$$E_{LH} = \frac{\hbar^2 k^2}{2m_0} - \frac{2k^2 P^2}{3E_g} \quad (1.11)$$

$$E_{SO} = -\Delta + \frac{\hbar^2 k^2}{2m_0} - \frac{k^2 P^2}{3(E_g + \Delta)} \quad (1.12)$$

Here Δ is the spin-orbit split-off energy and P is the Kane's parameter. As a result of ignoring remote band effects, the above dispersion relations are isotropic in k . The effective masses at the band edge, $k = 0$, are

$$\frac{1}{m_{CB}^*} = \frac{1}{m_0} + \frac{4P^2}{3E_g} + \frac{2P^2}{3(E_g + \Delta)} \quad (1.13)$$

$$\frac{1}{m_{HH}^*} = \frac{1}{m_0} \quad (1.14)$$

$$\frac{1}{m_{LH}^*} = \frac{1}{m_0} - \frac{4P^2}{3E_g} \quad (1.15)$$

The terms in the above effective mass expressions indicate the interactions between the bands [17]. Also according to the above equations, we can see that the heavy hole band is dispersionless. But when we add higher band effects, we will find a more realistic heavy hole dispersion.

The dispersion relations given by equations (1.9) to (1.12) are nonparabolic, meaning that the effective mass increases with increasing energy or, equivalently, k .

From equation (1.7), the energy-dependent conduction band effective mass is:

$$\frac{1}{m_{CB}^*} = \frac{2P^2}{3} \left(\frac{2}{E' + E_g} + \frac{1}{E' + E_g + \Delta} \right). \quad (1.16)$$

As mentioned earlier, effects of higher bands are not included in this model. We used the Kane model to calculate the subband energies in quantum wells.

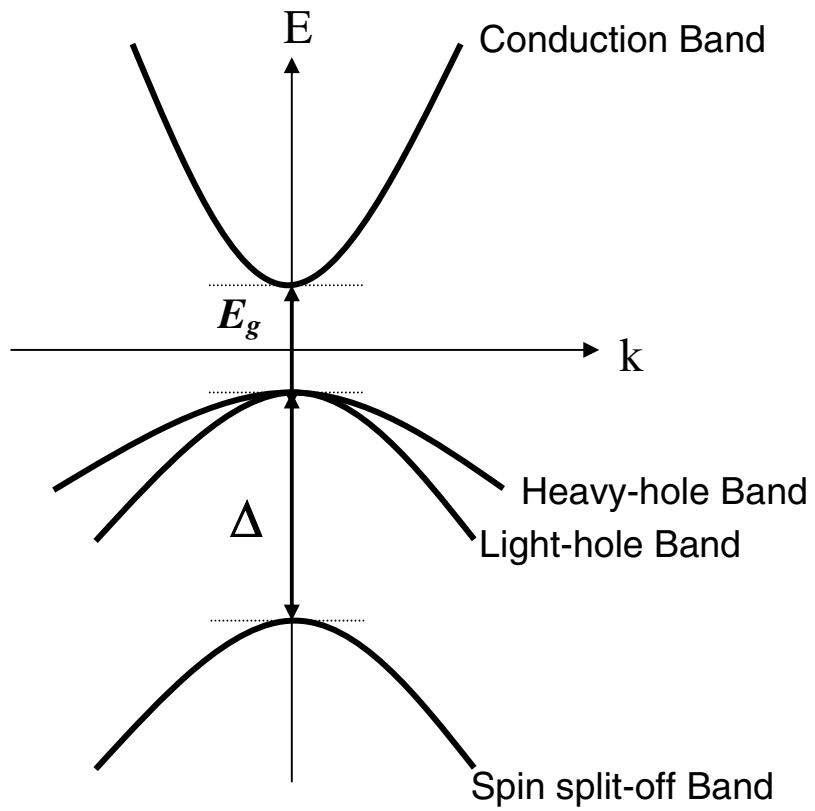


Figure 1.5: The band-edge energies ($E_g, 0, 0, -\Delta$) for the conduction, heavy-hole, light-hole and split-off bands.

1.6 Subbands in Undoped Quantum Wells

1.6.1 Subband energies for $k_x = 0$

The Hamiltonian of the square quantum well is given by [17]:

$$\left[p_z \frac{1}{2m(E, z)} p_z + V_s(z) \right] f(z) = Ef(z). \quad (1.17)$$

Here $m(E, z)$ is the energy dependent effective mass, $V_s(z)$ is the potential well for the electron and $f(z)$ is the confined-state envelope function of the electron. Functions $f(z)$ and $\frac{1}{m(E, z)} \frac{df(z)}{dz}$ are continuous at the boundary (i.e. well/barrier interface).

Effective mass has an explicit position dependence in the presence of band bending.

The solutions of the square QW are well known with the dispersion relation for both odd and even solutions in the well:

$$\cos(k_w L) - \frac{1}{2} \left[-\xi + \frac{1}{\xi} \right] \sin(k_w L) = 0. \quad (1.18)$$

where $\xi = \frac{m_b(E)k_w}{m_w(E)k_b}$ and $m_b(E)$ and $m_w(E)$ are the energy dependent effective mass

in the barrier and well respectively.

$$\frac{1}{m_w} = \frac{2P^2}{3} \left[\frac{2}{E + E_{gw}} + \frac{1}{E + E_{gw} + \Delta_w} \right] \quad (1.19)$$

$$\frac{1}{m_b} = \frac{2P^2}{3} \left[\frac{2}{E - V_s + E_{gb}} + \frac{1}{E + E_{gb} + \Delta_b} \right] \quad (1.20)$$

E_{gw} and E_{gb} are the band gaps in the well and barrier respectively and Δ_w and Δ_b are the split off energies in the well and barrier.

The wave vectors in the well and barrier for electrons and light holes are given in the Kane model:

$$k_w^2 = \frac{E(E + E_{gw})(E + E_{gw} + \Delta_w)}{\hbar^2 P^2 (E + E_{gw} + \frac{2}{3} \Delta_w)}. \quad (1.21)$$

$$k_b^2 = \frac{(E - V_s)(E - V_s + E_{gb})(E - V_s + E_b + \Delta_b)}{\hbar^2 P^2 (E - V_s + E_{gb} + \frac{2}{3} \Delta_b)}. \quad (1.22)$$

For heavy holes, the dispersion relation is parabolic. The wave vectors for the well and barrier given by;

$$k_w = \sqrt{-2m_{hhw}(E_{gw} + E)/\hbar}. \quad (1.23)$$

$$k_b = \sqrt{-2m_{hbb}(E_{gw} + E + V_p)/\hbar}. \quad (1.24)$$

Here m_{hhw} and m_{hbb} are heavy hole masses for the well and barrier. V_s and V_p are the conduction and valence band offsets and are defined in Figure 1.4.

1.6.2 Subband energies for $k_t \neq 0$

Following equations give the wave vectors in the well and barrier when $k_t \neq 0$ [18]

$$k_w^2 = \frac{E(E + E_{gw})(E + E_{gw} + \Delta_w)}{\hbar^2 P^2 (E + E_{gw} + \frac{2\Delta_w}{3})} - k_t^2 \quad (1.25)$$

$$k_b^2 = k_t^2 - \frac{(E - v_s)(E - v_s + E_{gb})(E - v_s + E_{gb} + \Delta_b)}{\hbar^2 P^2 (E - v_s + E_{gb} + \frac{2\Delta_b}{3})} \quad (1.26)$$

The bound states are the solutions of the following dispersion relation.

$$\cos(k_w L) + \frac{1}{2} \left[\frac{k_b m_w}{m_b K_w} - \frac{k_w m_b}{m_w K_b} - \frac{k_t^2}{k_w k_b} \frac{(\xi_w - \xi_b)^2}{m_w m_b} \right] \sin(k_w L) = 0 \quad (1.27)$$

Here

$$\frac{1}{\xi_w} = \frac{2P^2}{3} \left[\frac{1}{E + E_{gw}} - \frac{1}{E + E_{gw} + \Delta_w} \right] \quad (1.28)$$

$$\frac{1}{\xi_b} = \frac{2P^2}{3} \left[\frac{1}{E - V_s + E_b} - \frac{1}{E + E_{gb} + \Delta_b} \right]$$

Figure 1.6 (a) and (b) shows the calculated subband energies using the above Bastard formalism.

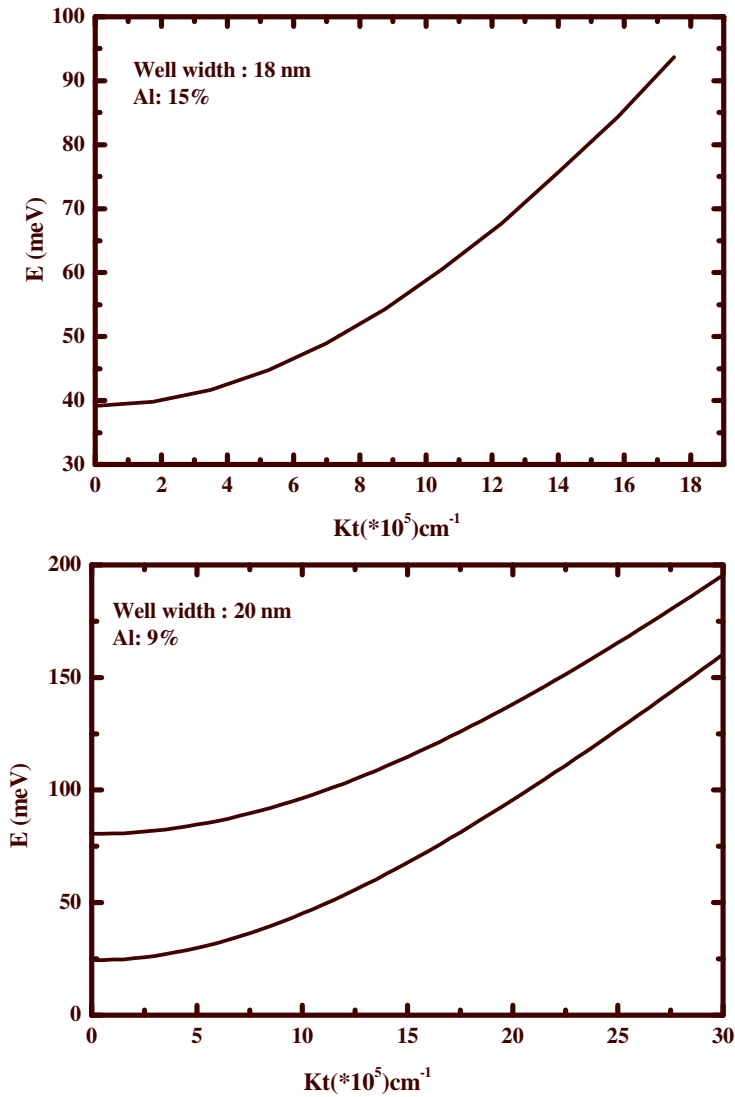


Figure 1.6: Calculated subband dispersion relations of InSb/AlInSb quantum wells using the Bastard formalism. Figure (a) represents the first subband energy for 18nm quantum well with 15% Al in the barrier. Figure (b) shows the first and second subband energies for the 20nm well with 9% Al in the barrier

1.7 Luttinger Model

As mentioned earlier, the Kane model does not include the effect of higher bands. As a result, the Kane model does not produce the correct effective mass for heavy holes. We use the Luttinger model to define the heavy hole effective mass more accurately. In this model the warping of the energy surfaces is taken into account. The details of the Luttinger model can be found in several different references such as Ref. [19, 20]. In this model the valence band dispersion relation obtained by diagonalizing the Luttinger Hamiltonian and is given by:

$$E(k) = \frac{\gamma_1 \hbar^2 k^2}{2m_0} \pm \frac{\hbar^2}{m_0} \left[\gamma_2^2 k^4 + 3(\gamma_3^2 - \gamma_2^2)(k_x^2 k_y^2 + k_y^2 k_z^2 + k_z^2 k_x^2) \right]^{1/2}. \quad (1.29)$$

In the above equation, the (+) sign is for light holes and the (-) sign is for heavy holes. Here γ_1 , γ_2 and γ_3 are the Luttinger parameters, which can be found in Landolt-Börnstein [15]. The z-axis and x-y axes are perpendicular and parallel to the interface, respectively.

In the Luttinger model, a diagonal approximation is often used in the literature. In this approximation all off-diagonal terms are neglected. The dispersion relation for light heavy and heavy holes can be rewritten using Luttinger's valence band Hamiltonian as:

$$E_{\pm} = \frac{\hbar^2}{2m_0} (\gamma_1 \pm 2\gamma_2) k^2. \quad (1.30)$$

Using this dispersion relation, the band edge effective masses of heavy holes and light holes for the direction of quantization becomes:

$$m_{hh}^* = \frac{m_0}{(\gamma_1 - \gamma_2)}$$

and

$$m_{lh}^* = \frac{m_0}{(\gamma_1 + 2\gamma_2)}.$$

According to the Luttinger equation, Eq. (1.29), the k dispersion in a [001] direction perpendicular to z is given by: $E_{\pm} = \frac{\hbar^2}{2m_0}(\gamma_1 \pm \gamma_2)k^2$. Here the (+) sign is for light holes and the (-) sign is for heavy holes. Thus, the masses for the motion in the xy-plane within the Luttinger model are

$$m_{hh}^* = \frac{m_0}{\gamma_1 + \gamma_2}$$

and

$$m_{lh}^* = \frac{m_0}{\gamma_1 - \gamma_2}.$$

The heavy hole band has a lighter mass (steeper curvature) and light hole band has a heavier mass (shallower curvature) for the in-plane motion. According to the above discussion we can see that the heavy hole effective mass is larger than the light hole mass in the z-direction but smaller in the perpendicular plane.

Chapter 2

Excitons in quantum wells

This chapter introduces the key ideas and concepts related to excitons that are necessary for the rest of the thesis and are organized as follows. In section 2.1 the effects of the Coulomb interaction that leads to the formation of excitons are explained. Then quantum well excitons and the two-dimensional hydrogen model are explained. Finally, a brief description of the motion of excitons in a magnetic field is given.

2.1 The concept of an exciton

It is well known that in an ideal case and at low temperature all the electrons in the crystal occupy the “valence band”. The question is what will happen if we excite one of these valence electrons? When light illuminates a semiconductor with photon energy greater than the band gap energy, an electron can be promoted to the conduction band leaving a hole in the valence band. Since the electron and hole are oppositely charged, they bind due to their mutual coulomb interaction forming an electron-hole pair, i.e. the exciton. Figure 2.1 shows how exciton effects arise (in 3D). The electron-hole pair forms a bound state, which is described by an envelope function. Excitons can be roughly divided into two types. The first type of excitons, studied in this thesis, is the one introduced by Wannier for semiconductors [21]. Because of the large static dielectric constant in semiconductors, the Coulomb interaction between electron and hole is greatly reduced, and their mean separation is

much larger than the lattice spacing. In other words, the envelope function extends over several hundred Angstroms. In this case the binding is sufficiently weak and one has a Mott-Wannier exciton. In a three-dimensional semiconductor the exciton binding energy may be small at room temperature and excitonic effects are not important. However, with decreasing temperature and/or with decreasing dimensionality (such as quantum wells, wires and dot) excitonic effects become important, and dominate the optical response at energies around the band-gap energy. In the second case, the hole and electron are tightly bound and sit on the same site; then one has a Frenkel exciton. In this case envelope function is confined to a few unit cells.

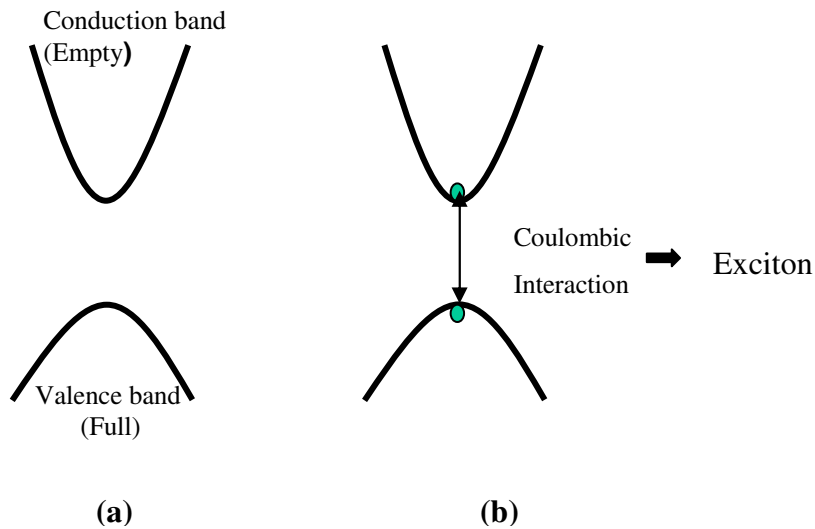


Figure 2.1: (a) The band structure of a semiconductor with a full valence band and empty conduction band. There are no allowed states in the gap. (b) The Coulombic interaction between the electron and hole that would modify the band picture.

The total charge of this two-particle system (electron-hole pair) is zero. As a consequence, this neutral exciton (X_0) can transport energy, but no charge. The formation of excitons results in the existence of new energy states in the semiconductor band gap slightly lower than the conduction band edge by an amount equal to the exciton binding energy. When the electron and hole recombine, the semiconductor emits a photon with energy equal to the X_0 total energy. The X_0 energy states in a (direct) semiconductor with parabolic conduction band are pictured schematically in Figure 2.2 [22]. The exciton is often considered to be the semiconductor analogue of the hydrogen atom [23]. Under the influence of the host semiconductor, that is the effect of the effective electron mass and the dielectric constant, the exciton binding energy is about thousand times smaller than in H, and the Bohr radius is about one hundred times larger. As a consequence the exciton is much more sensitive to the effect of externally applied electric and magnetic fields. The charge neutrality of excitons also affects the influence of an external magnetic field on their motion. The behavior of excitons in magnetic field depends on the strength of the magnetic field. A theoretical description of hydrogenic excitons in magnetic fields of arbitrary strength is given by Akimoto and Hasegawa [24]. A full discussion of the magnetic field dependence of excitons is carried out in the chapter 6.

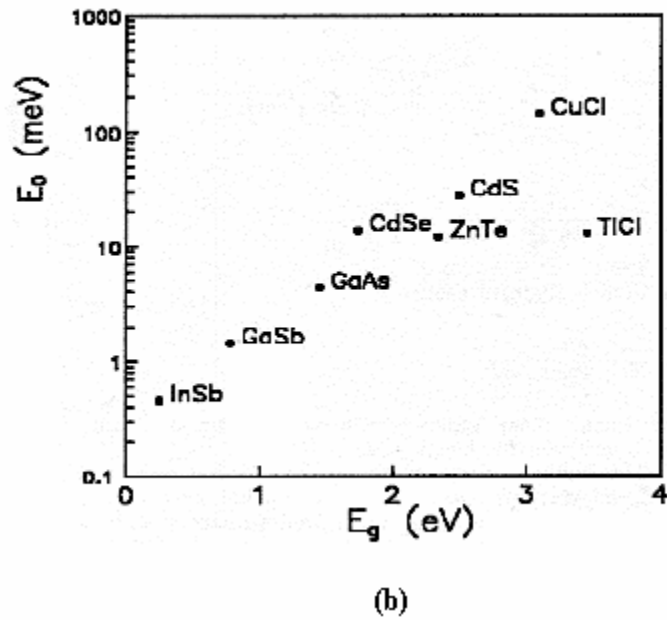
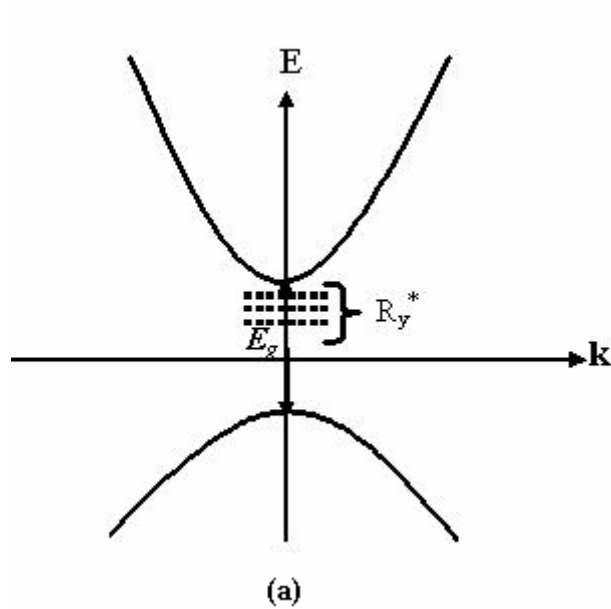


Figure 2.2: (a) Exciton formation results in the existence of new energy states in semiconductor band gap E_g . (b) Binding energy E_b for different host semiconductor bulk materials [22].

2.2 Excitons in Semiconductor Quantum Wells

2.2.1 Ideal 3D and 2D excitons

The optical properties of low-dimensional semiconductor heterostructures are dominated by excitons. The ability to fabricate low-dimensional semiconductor heterostructures, where electrons and holes can be strongly confined within small region, has given exciton research an important technological aspect. The motivation for exciton studies is based on interest in material characterization, pure physics, and optical information processing.

In order to determine the energy spectrum of the exciton, we write the Hamiltonian equation for two particles of mass m_e^* and m_h^* having opposite and equal charge, embedded in a medium with dielectric constant ε .

$$\left[\frac{-\hbar^2}{2m_e^*} \nabla^2 + \frac{-\hbar^2}{2m_h^*} \nabla^2 - \frac{e^2}{\varepsilon |r_e - r_h|} - E \right] \varphi(r_e, r_h) = 0 \quad (2.1)$$

After separation in the center of mass and relative orbital motion of the electron-hole pair and solving the orbital Schrödinger equation, one obtains a series of discrete bound exciton states ($n = 1, 2, \dots$) located below the band gap with the binding energies

$$E^{3D} = \frac{\mu e^4}{2\hbar^2 \varepsilon^2 n^2} = \frac{\mu}{m_e \varepsilon n^2} R_y = \frac{R_y^*}{n^2} \text{ with } R_y^* = \frac{\mu R_y}{m_e \varepsilon^2} \quad (2.2)$$

where R_y^* denotes the Rydberg energy and μ is the reduced effective mass. $R_y = 13.6eV, n = 1, 2, \dots$

In the case of a perfect crystal the electron and hole pair can move freely through the semiconductor bound by their coulomb interaction, which depends on their relative separation. The effective exciton Bohr radius, a_B^* which is the averaged separation between the electron and hole, is given by [12]

$$a_B^* = \varepsilon \frac{m_e}{\mu} a_B. \quad a_B = 0.529 \text{ \AA}, \quad \varepsilon = 12.5 \text{ for GaAs}$$

where $\mu = \frac{m_e^* m_h^*}{m_e^* + m_h^*}$. For GaAs $m_e^* \approx 0.067 m_e$, $m_h^* \approx 0.34 m_e$ and $a_B^* \sim 120 \text{ \AA}$.

The exciton dispersion relation, $E_X(n, \vec{K})$ for bulk semiconductors is given by

$$E_X(n, \vec{K}) = E_g - \frac{R_y^*}{n^2} + \frac{\hbar^2 \vec{K}^2}{2(m_e^* + m_h^*)}. \quad (2.3)$$

Here \vec{K} is the wave vector of exciton and $\vec{K} = \vec{k}_e + \vec{k}_h$. As explained earlier, the center of mass describes the motion of the excitons as a whole with respect to the semiconductor lattice, while the term in relative coordinates is very similar to the problem of Hydrogen atom. Excitons are therefore generally regarded as hydrogen-like complexes embedded in the semiconductor, resulting in modified energy and length scales expressed in terms of the effective Rydberg and Bohr radius.

2.3 Two-dimensional hydrogen model

The solutions of the exciton problem in layered semiconductor structures was first presented by Shinada and Sugano [25] and they obtained energy levels for 2D excitons in zero magnetic field. In order to overcome the problem that the Coulomb interaction couples the electron-hole pair motion in the growth direction and in the plane perpendicular, they used an infinite effective mass for the motion along growth axis. Using this approach, they treated the hypothetical case of an ideally 2D exciton. In this section we discuss the two-dimensional hydrogen model.

The Schrödinger equation for a two-dimensional hydrogen atom:

$$\frac{-\hbar^2}{2\mu} \left(\frac{\partial^2}{\partial x^2} + \frac{\partial^2}{\partial y^2} \right) \phi - \frac{e^2}{\epsilon \sqrt{(x^2 + y^2)}} \phi = E \phi. \quad (2.4)$$

The envelope function describes the relative motion of an interacting electron and hole pair. When polar coordinates are used, the wave function satisfying equation (2.4) can be separated into a radial part and angular part. The solution is of the form

$$\phi(r) = \frac{1}{\sqrt{2\pi}} R(r) e^{im\phi}. \quad (2.5)$$

Here m is an integer. The radial function $R(r)$ satisfies the equation

$$\left[\frac{-\hbar^2}{2\mu} \left\{ \frac{1}{r} \frac{d}{dr} \left(r \frac{d}{dr} \right) - \frac{m^2}{r^2} \right\} - \frac{e^2}{\epsilon r} \right] R(r) = ER(r). \quad (2.6)$$

For $E < 0$, the solution of equation (2.6) corresponds to bound states and a discrete energy spectrum is obtained [25, 26, and 14].

Using a change of variables, $\gamma^2 = -\frac{R_y}{E}$, $\rho = \frac{1}{\gamma} \left(\frac{2r}{a_B} \right)$

We obtain

$$\left(\frac{d^2}{d\rho^2} + \frac{1}{\rho} \frac{d}{d\rho} - \frac{m^2}{\rho^2} + \frac{\gamma}{\rho} - \frac{1}{4} \right) R(\rho) = 0. \quad (2.7)$$

As $\rho \rightarrow \infty$, we find that dominant terms above are

$$\left(\frac{d^2}{d\rho^2} - \frac{1}{4} \right) R(\rho) = 0 \quad (2.8)$$

Therefore, we set

$$R(\rho) = e^{-\rho/2} h(\rho) \left[\frac{d^2}{d\rho^2} + \frac{(1-\rho)}{\rho} \frac{d}{d\rho} + \frac{1}{\rho} \left(\gamma - \frac{1}{2} - \frac{m^2}{\rho} \right) \right] h(\rho) = 0. \quad (2.9)$$

As $\rho \rightarrow 0$, dominant terms are

$$\left(\frac{d^2}{d\rho^2} + \frac{1}{\rho} \frac{d}{d\rho} - \frac{m^2}{\rho^2} \right) h(\rho) = 0. \quad (2.10)$$

Therefore, $R(\rho)$ behaves like $\rho^{|m|}$.

Making the substitution $h(\rho) = \rho^{|m|} f(\rho)$, we obtain

$$\left[\rho \frac{d^2}{d\rho^2} + (2|m|+1-\rho) \frac{d}{d\rho} + \left(\gamma - \frac{1}{2} - |m| \right) \right] f(\rho) = 0. \quad (2.11)$$

By comparing the above with the definition of the confluence hypergeometric function $F(\alpha, \beta; \rho)$

We obtain $f(\rho) = F\left(\left|m\right| + \frac{1}{2} - \gamma, 2\left|m\right| + 1; \rho\right)$

This requires $\left|m\right| + \frac{1}{2} - \gamma$ be a negative integer, i.e., $\gamma \geq \left|m\right| + \frac{1}{2}$ and $n \geq \left|m\right| + 1$ therefore

γ is related to n as follows:

$$\gamma = \left(n - \frac{1}{2}\right)$$

Consequently, the energy eigenvalues of equation (2.4) are

$$E_n = -\frac{R_y^*}{\left(n - \frac{1}{2}\right)^2}. \quad \text{Here } n = 1, 2, 3, \dots \quad (2.12)$$

In the 2D case the eigen energies of the exciton Hamiltonian are given by [22]

$$E^{2D} = E_g + E_{n_e} + E_{n_h} - \frac{R_y^*}{\left(n - \frac{1}{2}\right)^2} + \frac{\hbar^2(k_x^2 + k_y^2)}{2(m_e^* + m_h^*)}. \quad (2.13)$$

The carrier confinement strongly modifies the properties of excitons in low dimensional structures with respect to the bulk. From the above equations we can see that with decreasing dimensionality the exciton binding energy increases. Restricting the comparison of 3D and 2D excitons to the exciton ground state, yields the following results [22]:

- (i) The binding energy in 2D is four times larger than in bulk material and in the limit of a purely two-dimensional case the effective Rydberg $R_{2D} = 4R_{3D}$. Consequently, in quantum well structures excitonic resonances can be observed even at room temperature.
- (ii) In 3D, the oscillator strength $f \propto 1/n^3$ and in 2D the oscillator strength $f \propto 1/(n-1/2)^3$. Hence, the oscillator strength of 2D excitons is strongly enhanced with respect to the 3D value. In a quantum well the electron and hole levels are separately quantized in discrete subbands and this quantization increases both the overlap between electron and hole and their attraction, which results in turn in a reduction of the two-dimensional Bohr radius. Reduction of Bohr radius leads to increase the oscillator strength of the exciton.
- (iii) The 2D exciton Bohr-radius given by the ground state wave function is two times smaller than in the 3D case.

In a real quantum well the exciton wave function penetrates the barrier layers and has a finite extent in the growth direction. Therefore the system is not truly two-dimensional and the exact 2D limit (well width $\ll a_B$) can only be approached hypothetically in an infinitely deep quantum well. The exciton binding energy therefore depends on the well width and depth and has a value between that of the 3D and 2D limits. In the limit of very wide quantum wells, excitons look like bulk, in both its binding energy and Bohr radius and in the limit of very narrow wells, the exciton become two-dimensional in nature.

2.4 Effect of a perpendicular magnetic field

2.4.1 Free carriers

We now focus on the quantum mechanical properties of charges in a QW when applying a magnetic field perpendicular to the plane of the QW. In particular, the presence of a magnetic field causes an additional magnetic confinement of the charges and can be described as follows. We restrict the discussion to electrons in the conduction-band QW, but a similar approach can be used for holes in the valence-band QW. When a magnetic field is applied perpendicular to the QW plane, the Hamiltonian describing free electrons in the plane using Landau gauge becomes:

$$H = \frac{1}{2m} (\nabla_x - eB_y)^2 + \frac{1}{2m} \nabla_y^2 + \frac{1}{2m} \nabla_z^2 + V(z). \quad (2.14)$$

A detailed explanation of the derivation of this Hamiltonian can be found elsewhere [27].

The Hamiltonian commutes with ∇_x therefore the wave function can be written as:

$$\varphi = e^{ikx} f(z)\phi(y). \quad (2.15)$$

Ultimately we obtain the Schrödinger equation:

$$\nabla_y^2 \Phi(y)f(z) + \left[\frac{2mE}{\hbar^2} - \frac{m^2 \omega_c^2}{\hbar^2} (y - y_0)^2 \right] \Phi(y)f(z) - \left[\nabla_x^2 f(z) + V(z)f(z) \right] \Phi(y) = 0 \quad (2.16)$$

With $y_0 = \frac{\hbar k_x}{eB}$ and the cyclotron frequency $\omega_c = \frac{eB}{m}$.

The above Schrödinger equation is the same as that for a harmonic oscillator constrained to move along the y-axis and centered on y_0 . Therefore, the eigenvalues

of above equation are given by discrete energy levels $E_n = \hbar\omega_c(n + \frac{1}{2})$, which are commonly referred to as *Landau levels*. Consequently, an electron confined in a QW in the presence of a uniform magnetic field perpendicular to the QW plane has, neglecting the spin, discrete energy levels given by

$$E = \left(n + \frac{1}{2}\right)\hbar\omega_c + E_m. \quad (2.17)$$

If we add electron spin to the picture, the total energy of the Landau-quantized system is

$$E_{n,m} = E_m + \left(n + \frac{1}{2}\right)\hbar\omega_c \pm \frac{1}{2} g^* \mu_B B. \quad (2.18)$$

Equation 2.18 can be interpreted in the following way: Each QW state E_m has associated with it a ladder of Landau levels separated by energy $\hbar\omega_c$ and each Landau level is split in two spin components by the Zeeman splitting. Calculated conduction band Landau levels are shown in Figure 2.3. Fig 2.3 is called fan diagram, which is an energy spectrum versus magnetic field plot for different Landau levels. In Figure 2.3 solid (dashed) lines represent spin up (down) states. This calculation takes into account the strong energy dependence of the g -factor and of the effective mass. In the classical picture, the electron with $n = 0$ moves in a circular orbit with frequency ω_c

and a radius given by the magnetic length: $l = \sqrt{\frac{\hbar}{eB_z}}$.

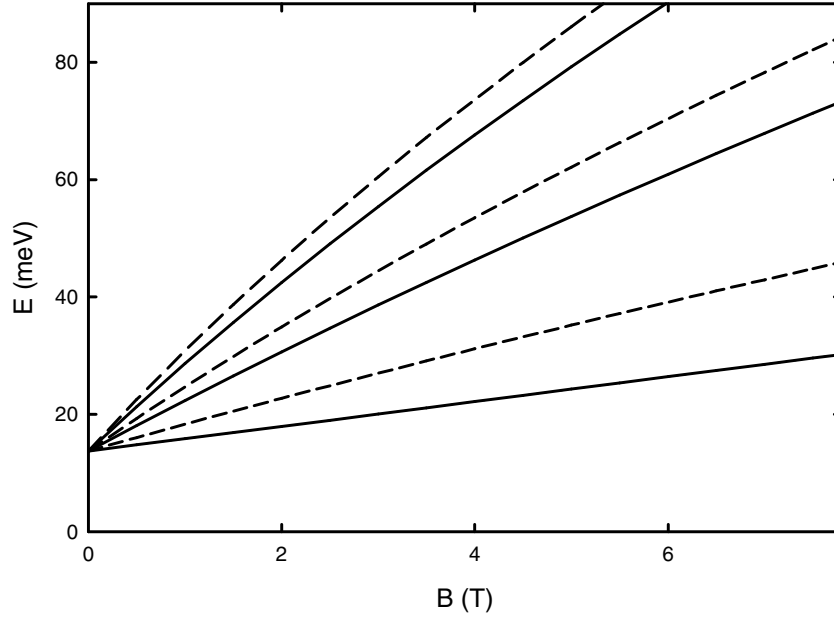


Figure 2.3: Calculated Landau levels energies for the QW of 30nm width and 15% Al in the barrier as a function of magnetic field. The solid lines (dashed lines) represent spin up (down) states.

2.4.2 Excitons in Magnetic Field

As explained earlier, in addition to the QW confinement, a second confinement can be introduced by applying an external magnetic field, B . In particular, the magnetic field increases the neutral exciton binding energy by squeezing the electron-hole wave function and so reducing the inter-particle distance.

In the previous section we explained how electrons described by “free” states are affected by a magnetic field. But what happens if the electrons are in a “bound”

state? How are these states affected by a magnetic field? These issues are addressed in this section.

To be definite, we concern ourselves with quasi-two dimensional finite quantum wells where electron and hole motion is quantized in the [001] direction. The Hamiltonian of an exciton associated with either the HH or LH band in the quantum well can be expressed as [28, 29]

$$\left[\frac{P^2}{2\mu} + e \left(\frac{1}{m_h} - \frac{1}{m_e} \right) \vec{A} \cdot \vec{P} + \frac{e^2}{2\mu} \vec{A} \cdot \vec{A} - \frac{e^2}{4\pi\epsilon r} - \frac{2e\hbar}{m_h + m_e} \vec{K} \cdot \vec{A} \right] \Phi(r) = E_r \Phi(r). \quad (2.19)$$

Here μ is the reduced effective mass and \vec{A} is the vector potential due to the magnetic field and \vec{K} is the wave vector of exciton. If we choose the Lorentz gauge (symmetric gauge) such that

$$\vec{A} = \frac{1}{2} \vec{B} \times \vec{r} \quad \text{and if B is in z direction, then } \vec{A} = \frac{-B}{2} (y, -x, 0)$$

The various magnetic field dependent terms of the above equation can be explained as follows.

- The second term in the Hamiltonian can be written as:

$$\frac{e}{2} \left(\frac{1}{m_h} - \frac{1}{m_e} \right) \vec{B} \cdot \vec{L}$$

Which is the Zeeman term and makes no contributions so as long as we concern ourselves with an exciton of S- symmetry (i.e. $m = 0$).

- The third term is the diamagnetic operator: $\frac{e^2}{8\mu}(\vec{B} \times \vec{r})^2$.
- The term involving the scalar product of \vec{K} with \vec{A} describes the coupling of the center-of-mass motion of the exciton to the magnetic field. For sufficiently small \vec{K} , the term $\left(\frac{eh}{m_e + m_h}\right)(\vec{K} \times \vec{B} \cdot \vec{r})$ can be neglected.

Therefore, equation (2.19) now takes the form

$$\left(\frac{P^2}{2\mu} - \frac{e^2}{4\pi\epsilon r} + \frac{e^2 B^2}{8\mu}(x^2 + y^2)\right)\Phi(r) = E\Phi(r). \quad (2.20)$$

As a measure of the strength of the magnetic field, we introduce γ which is equal to $\frac{\hbar\omega_c}{2R_y^*}$. Here $\hbar\omega_c$ is the cyclotron energy, $\frac{\hbar eB}{\mu}$, and R_y^* is the excitonic Rydberg energy.

In terms of γ the equation for the exciton in magnetic field is:

$$\left[-\nabla^2 - \frac{2}{\gamma} + \frac{\gamma^2}{4}(x^2 + y^2)\right]\Phi(r) = E\Phi(r). \quad (2.21)$$

In the low-field limit of $\gamma \ll 1$, the Coulomb energy dominates and the magnetic field can be treated as a perturbation. In the high-field limit of $\gamma \gg 1$, where electrons and holes are under cyclotron motion, the perturbation from the Coulomb interaction generates bound states belonging to Landau levels. In this limit we can use the conventional treatment of Landau states.

Chapter 3

Experimental Methods

In this chapter, the samples studied and the equipment and techniques that were employed in these experiments are presented. In section 3.2, the principles of a Fourier transform spectrometer are described. The observation of excitons at zero magnetic field and the method of analysis are explained in section 3.4.

3.1 Quantum well structure

Our samples were grown by molecular beam epitaxy (MBE) on (001) semi-insulating GaAs substrates. There is no suitable non-InSb substrate that could fit the lattice parameter of InSb. In this situation, because of its chemical stability and high resistivity, semi-insulating GaAs is used as a substrate material. The samples were nominally undoped with a background density of ionized impurities on the order of 10^{15} cm^{-3} [30, 31]. In order to reduce mismatch dislocations (there is a 14% mismatch between the GaAs and InSb lattices), a thick buffer layer was grown prior to the growth of a quantum well structure. The buffer layer consists of a sequential growth of a $0.1 \mu\text{m}$ AlSb layer followed by a $1 \mu\text{m}$ alloy layer, a ten-period $25\text{-}\text{\AA}$ - $\text{Al}_x\text{In}_{1-x}\text{Sb}$ / $25\text{-}\text{\AA}$ -InSb superlattice, and finally a $2 \mu\text{m}$ alloy layer again. The quantum well is sandwiched between $\text{Al}_x\text{In}_{1-x}\text{Sb}$ barriers with typical x values ranging from 5 to 20%. An InSb cap prevents the oxidation of $\text{Al}_x\text{In}_{1-x}\text{Sb}$ surface. The typical layer structure describing the samples used in this study is shown in Figure 3.1.

InSb cap layer	~100Å
8% AlInSb layer	~500Å
InSb layer	100Å
8% AlInSb spacer	500Å
InSb well	200Å
8% AlInSb spacer	500Å
8% AlInSb layer	~2.0 μm
8% AlInSb/InSb SLS10*(25Å+25Å)	
8% AlInSb buffer	1μm
AlSb nucleation layer	~10000Å
GaAs (001) substrate	

Figure 3.1: Typical layer structure of an undoped multiple quantum well (sample S948). The sample contains 40 InSb wells separated by 50nm-thick AlInSb barrier layers.

3.2 Fourier Transform Infrared Spectroscopy

Fourier Transform Infrared (FTIR) spectroscopy is a characterization and research technique widely used in many fields. It has the advantages of high spectral resolution, good signal-to-noise ratios, and the ability to measure a broad region of the spectrum in a short amount of time. In FTIR spectroscopy, all of the wavelengths are measured simultaneously with one detector. This allows the FTIR spectrometer to produce a spectrum quickly in order to combine multiple scans for a higher signal-to-noise ratio.

3.2.1 The Basics of FTIR Spectroscopy: How the device operates

A typical FTIR spectrometer is comprised of an infrared light source, a beam splitter, a fixed mirror, a moving mirror, a detector, a He-Ne laser, and a sample compartment. A He-Ne laser is collinear with the IR beam, which is invisible to human eyes.

The most important component of an FTIR spectrometer is the Michelson interferometer. Schematically it is illustrated in Figure 3.2. An interferometer consists of stationary and moving mirrors and a beam splitter in the middle. The beam splitter divides the incoming infrared beam into two components. One beam reflects off a flat mirror, which travels typically a few millimeters from the beam splitter. The two components are then reflected back and are recombined at the beam splitter. Because the path that one beam travels is a fixed length and the other is constantly changing as

its mirror moves, the signal which exits the interferometer is the result of these two beams “interfering” with each other. Consequently, the resulting signal is called an interferogram, which has every infrared frequency “encoded” into it. In other words the interferogram is a digital plot of light intensity versus mirror position. When the interferogram signal is transmitted through or reflected off the sample surface, specific frequencies are absorbed by the sample. The infrared signal after interaction with the sample is uniquely characteristic of the sample. This means that the detected interferogram contains the basic information on frequencies and intensities characteristic of a spectrum but in a form that is not directly interpretable.

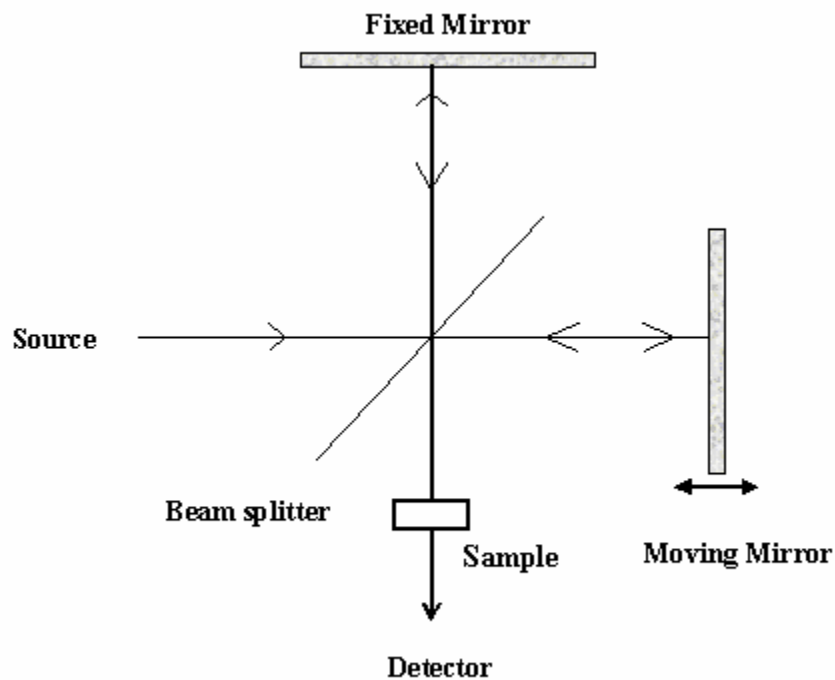


Figure 3.2: Schematic of a Michelson interferometer.

The beam finally arrives at the detector and is measured by the detector. The output from the detector is fed to a computer, which performs the Fourier transform calculation and converts the interferogram $I(\delta)$ into a single beam spectrum. This transformation is expressed mathematically as [32, 33]:

$$I(\nu) = C \int_{-\infty}^{+\infty} [I(\delta) - \frac{1}{2} \bar{I}(0)] \cos(2\pi\nu\delta) d\delta. \quad (3.1)$$

Here δ is the optical path difference or optical retardation, C is a constant and $I(0)$ is the signal intensity at $\delta = 0$. However, equation (3.1) requires that the optical path difference extend between the limits $(-\infty, \infty)$. This is practically impossible because the mirror scan is limited to a finite range $(-L, L)$. Here L is the displacement of the moving mirror. Thus, the spectrum is related $I(\delta)$ by means of the Fourier integral

$$I(\nu) = C \int_{-L}^{+L} [I(\delta) - \frac{1}{2} \bar{I}(0)] \cos(2\pi\nu\delta) d\delta. \quad (3.2)$$

This integral is carried out in a computer that is interfaced to the spectrometer, and the output, $I(\nu)$, is the absorption spectrum of the sample.

In practice, to maximize the signal-to-noise ratio, several hundred to several thousand interferograms are obtained and averaged before the Fourier transform is performed. Examples of a typical interferogram with no sample and its corresponding intensity spectrum are shown in Figure 3.3 and 3.4. A single beam spectrum is a plot of raw detector response versus wave number.

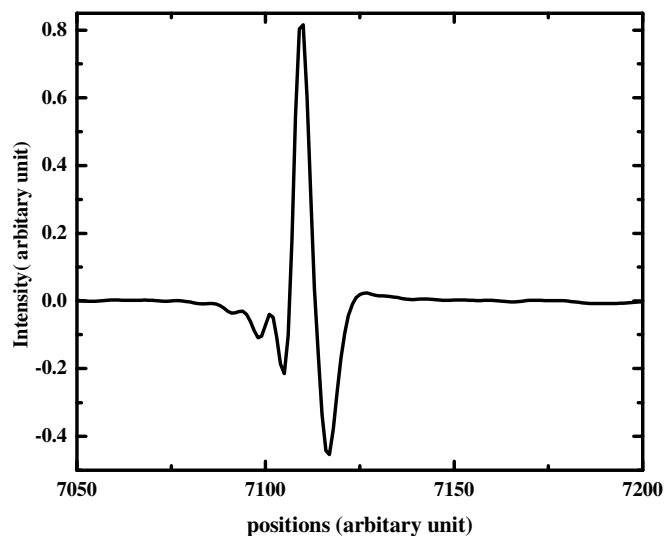


Figure 3.3: A typical interferogram taken with a globar source, a KBr beamsplitter and a DTGS room temperature detector using a IFS66v/s spectrometer under vacuum environment with no sample.

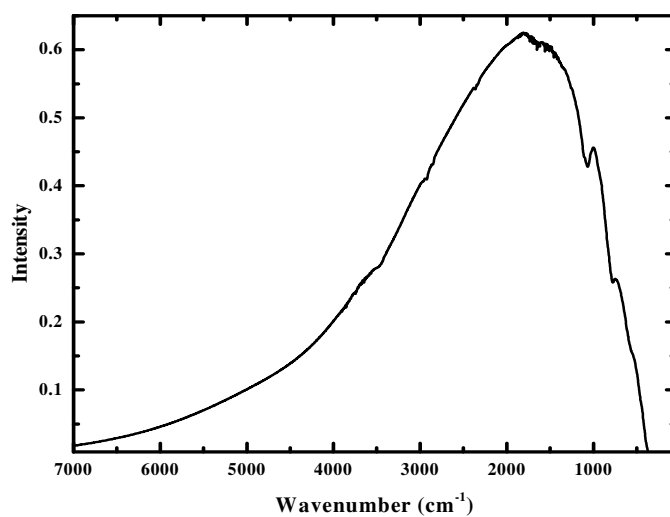


Figure 3.4: Fourier transform of the interferogram in Figure 3.3. Evacuation of the optics eliminates interference from atmospheric gases such as water vapor and carbon dioxide. The absorption feature between 1050cm^{-1} and 1200cm^{-1} is due Si impurities in the globar.

Generally, there are two methods of controlling the optical path length difference of the interferometer, continuous scan mode and step-scan mode. For our measurements we used the continuous scan mode. In this mode, the velocity of the moving mirror is held constant. The sinusoidal interference pattern generated by a reference HeNe laser is used to control the optical path length difference of the moving mirror. In step-scan mode, the moving mirror is controlled to a sequence of fixed positions and held there so that the optical path difference remains step-wise constant.

3.2.2 The Spectrometer

We used a Bruker Equinox 55 spectrometer for zero field optical measurements. It is equipped with an air-cooled mid-infrared source and it covers the spectral range from 7500-370 cm^{-1} . The spectrometer is configured with two detectors; a DTGS (deuterated triglycine sulfate) room temperature detector and an InSb liquid-nitrogen cooled detector. The instrument spectral resolution is about 0.5cm^{-1} . The resolution of a Micheson interferometer is the inverse of the path length traveled by the moving mirror; thus to obtain a 0.5 cm^{-1} resolution, the mirror must travel 2cm. This spectrometer cannot be evacuated, therefore in our spectra we see features due to water vapor and carbon dioxide. Nitrogen gas is used for the air bearings of the moving mirror and to purge spectrometer of water vapor. Purging helps to reduce the intensities of water based peaks but does not significantly affect

the intensity of carbon dioxide peaks. Figure 3.5 shows the peak positions of water vapor and Carbon dioxide.

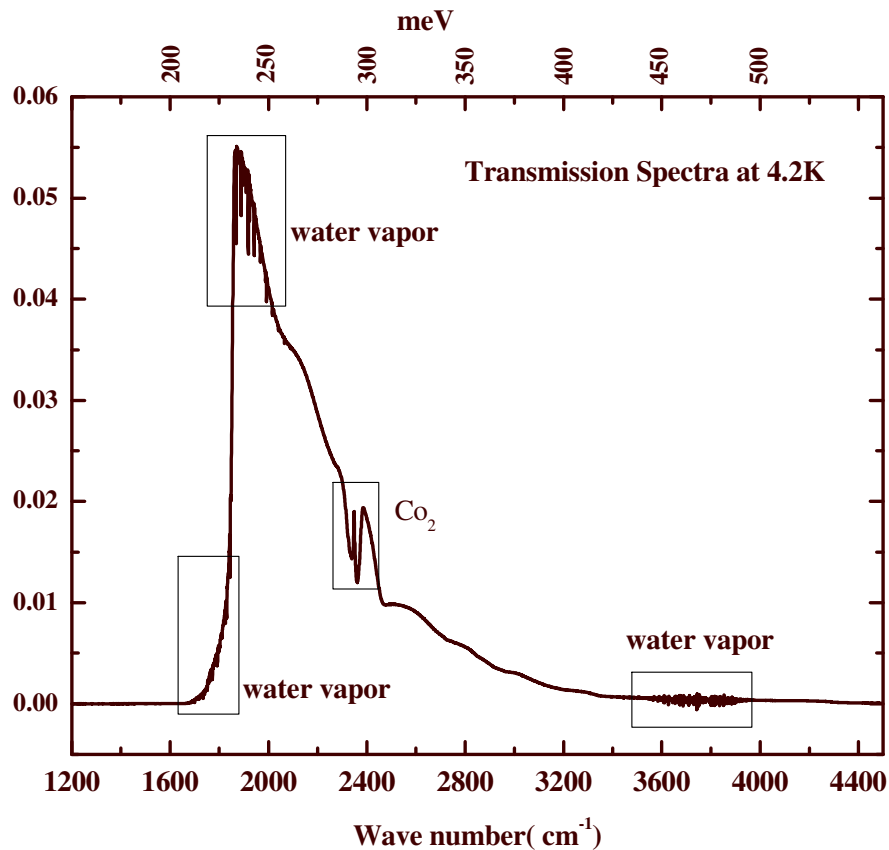


Figure 3.5: Peak positions of water vapor and carbon dioxide. Characteristic bands around $3960\text{-}3480\text{ cm}^{-1}$ and $2000\text{-}1300\text{ cm}^{-1}$ are ascribed to atmospheric water vapor, and the band at $2390\text{-}2280\text{ cm}^{-1}$ is attributed to carbon dioxide [34].

For our experiment we used a KBr (potassium bromide) beam splitter that is very sensitive to moisture, dust and other types of environmental contamination. Therefore it is very important not to touch any part of the beamsplitter other than the

handle. Touching any other part can damage or completely ruin the beamsplitter. Also it should be stored in the beamsplitter storage box whenever it is not being used in the spectrometer. The desiccant cartridge in the storage box should be replaced whenever the indicator in the capsule turns pink.

As shown in Figure 3.6, IR light from the source is collected by a parabolic mirror and then directed to the interferometer using a flat mirror. There is another parabolic mirror, which diverts the beam coming out from the interferometer. Then the beam is focused on the sample position and finally directed to the detector.

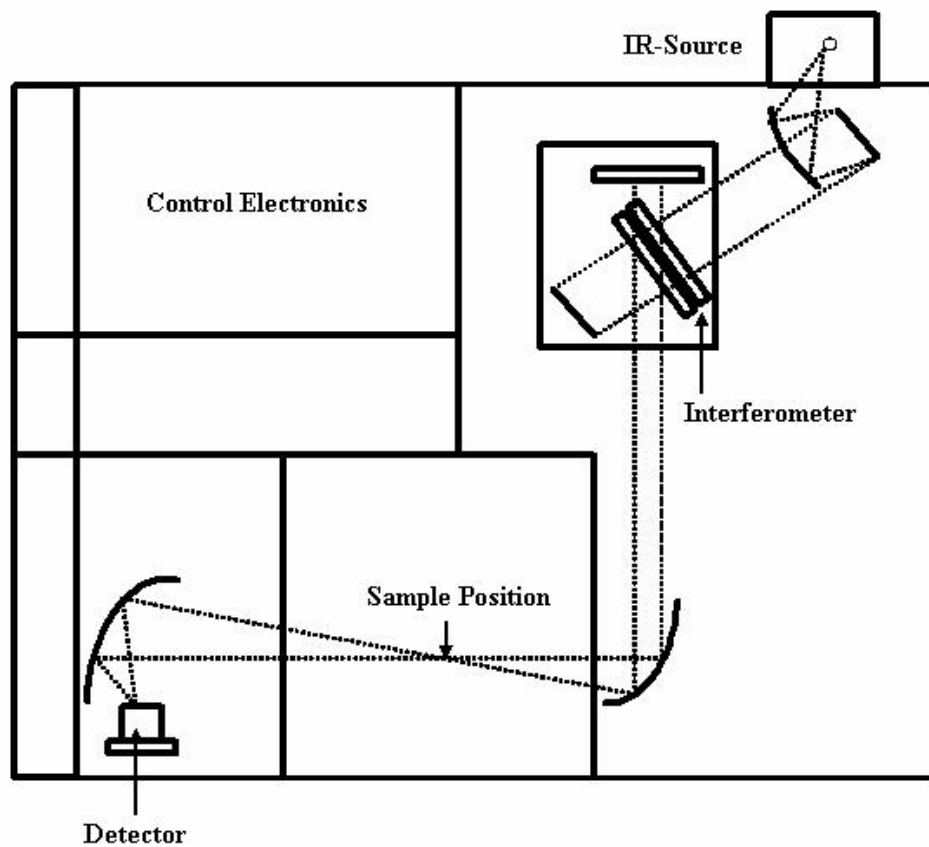


Figure 3.6: Block diagram of FTIR. Dash lines show the optical path [34].

3.2.3 Multi-reflection interference in InSb/AlInSb quantum wells

Interference fringes due to the interference between multiple reflections between the surfaces of a thin film can be seen in our samples. Figure 3.7 shows such multi-reflection interference on a thin film. The beams reflected by the top and bottom surfaces of the thin film interfere with each other.

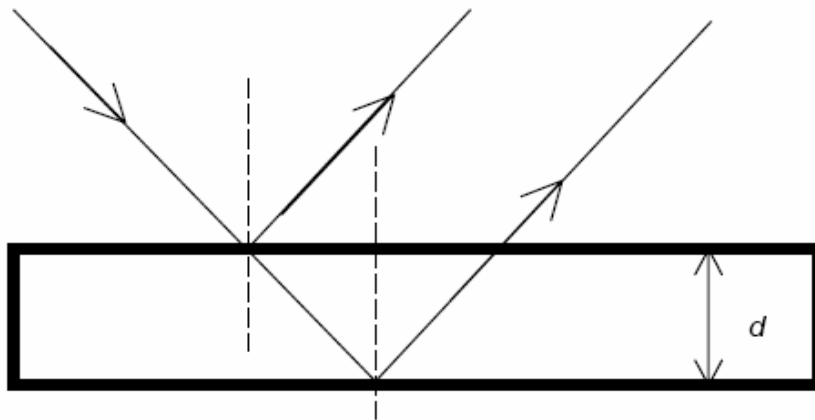


Figure 3.7: Illustration of multi-reflection interference.

For normal incidence, the relation for two adjacent interference maxima is given by

$$2nd = \lambda_m \left(m + \frac{1}{2}\right)$$
$$2nd = \lambda_{m+1} \left(m + \frac{1}{2} + 1\right)$$

Here d is the thickness of the film and λ_m and λ_{m+1} are the wavelengths (film) corresponds the m^{th} and $m+1^{\text{th}}$ peak.

Periodicity of the interference fringes is $\Delta\nu = \left(\frac{1}{\lambda_{m+1}} - \frac{1}{\lambda_m}\right) = \frac{1}{2nd}$. Here $\Delta\nu$ is the difference between two adjacent oscillation peaks. Since the wavelength depends on the index of refraction $\lambda(\text{film}) = \lambda(\text{vacuum})/n_r$. Here n_r is the refractive index of the film and $n_r = \sqrt{\varepsilon}$, where ε is the dielectric constant. From the periodicity of the interference fringes, we can calculate the thickness of the thin film that causes the multi reflection interference. As an example, considering the case shown in Figure 3.8, we find d as $5.2\mu\text{m}$, which is about the thickness of the whole layer.

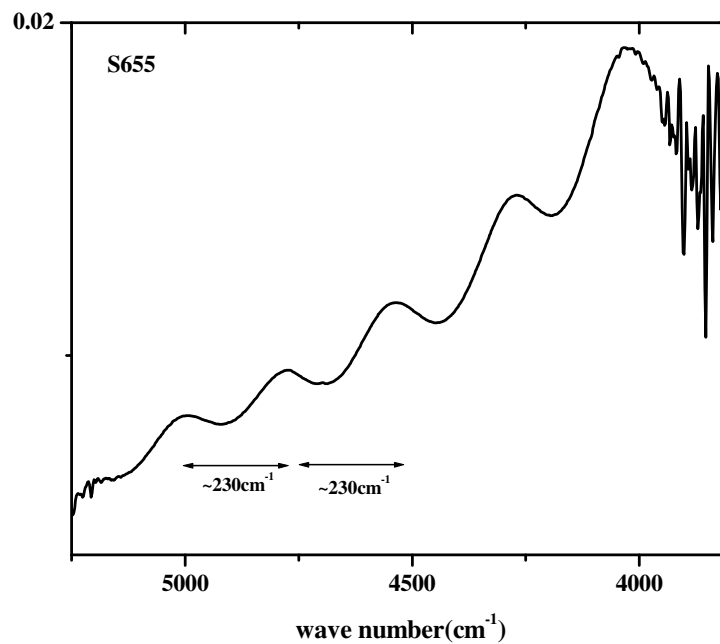


Figure 3.8: Transmission spectra of 5nm, 20% sample (before wedging). Fabry-Perot interference is clearly seen.

The interference can be reduced by making the sample surfaces non-parallel or with an anti-interference coating [35]. Our samples are wedged at 4° or, the top surface of the sample coated with an antireflection NiCr film. The procedure for wedging is explained in the next section. Also multiple-well-layer structure in the sample is important, as it can enhance absorption and reduce the relative intensity of Fabry-Perot interference.

3.3 Sample Preparation

Wedging the Samples

Prior to performing the optical measurements, samples were wedged to suppress Fabry-Perot interference. In the wedging process, first the samples are mounted using white paraffin wax on a clean glass slide, which is then mounted on an either 2° or 4° mounting block. The mounting block attaches to a South Bay Technology hand-lapping fixture (model 155) by means of a threaded knob. A small amount of Silicon Carbide powder (600grit/14.5 micron) is then mixed with water on flat glass piece. The sample and fixture are rubbed over the mixture for a few minutes to effect the wedging.

The mounting block with the sample is placed on a heated hotplate to remove the sample from the glass slide. Finally, the sample is placed in boiling trichloroethylene for 2 minutes, boiling acetone for 4 minutes, and finally boiling

methanol for 4 minutes. The purpose of above procedure is to remove any remaining wax. We used dry N₂ gas to dry the sample.

Next the sample is mounted in a cryostat (Janis Research Co.) that is then pumped overnight using a diffusion pump. Prior to cooling the sample, it is important to pump at least down to 10⁻⁴ Torr with a good diffusion pump to avoid condensation on the sample surface. Next the cryostat is mounted in the sample compartment in which the mount is adjustable to ensure that the sample is in the beam path. Sample transmission spectra are taken at different temperatures from room temperature to 4.2K. The temperature is measured through a connection to a Lakeshore Cryotronics, Inc. model 321-autotuning-temperature controller. Below 77K, we used a needle valve in the liquid helium transfer tube to control the temperature. This flow rate valve provides better temperature stabilization than the heater in the cryostat.

3.4 Spectroscopic Derivative

In order to employ the exciton theory explained in chapter 2 to analyze experimental transmission spectra, it is important first to accurately determine the resonance energy of excitonic features. On our raw FTIR spectra, the exciton peaks can be rather weak. To highlight weak excitonic peaks, we present the data in a differential form where we take the difference of two spectra measured at different temperatures and then normalize the difference spectrum by the average of the spectra. The energy gap of InSb (and of Al_xIn_{1-x}Sb) increases as temperature

decreases so that the spectra measured at different temperatures differ essentially in the region where the transition occurs. Thus, a difference spectrum highlights the transition lines while the unwanted background is suppressed. The differential spectrum is made possible by the temperature dependence of the InSb band gap. However, one should be careful when choosing the temperatures to take a difference. At higher temperatures, variation of the energy gap with temperature is linear. At low temperatures, the energy gap as a function of temperature saturates so that, from 30 to 4.2K, the energy gap of InSb increases only by 1 meV. On the other hand, from 80K to 4.2K, the energy gap difference is about 8 meV thus the band gap is strongly depends on temperature at higher temperatures. In the low temperature range, a difference of about 20K-25K yields sharp features. The normalized difference spectrum can therefore be viewed as a derivative spectrum, which is close to a mathematical derivative of the original spectrum but has a much better signal-to-noise ratio. Figure 3.9 shows the raw spectra of a 20nm sample at 4K and 30K. The excitonic feature of the transmission spectra is visible as well-defined dips on the spectra. Clearly, there is little difference between the spectra at different temperatures except where the interband transitions occur. Figure 3.10 demonstrates the differential transmission spectra of the same sample, which exhibits the enhanced features. The differential enhancement technique gives the negative derivative of the transmission curve. Thus, we mark the inflection point as the excitonic peak position due to the differential spectra [36].

We use HH, LH and CB to represent heavy hole, light hole and conduction-band states respectively. As shown in the Figure 3.10, the observed transitions are labeled as HH1-CB1, HH2-CB2 and LH1-CB1. The assignments of the transmission peaks are made by comparison with a four-band model calculation [17]. Due to the strain in the system and the different effective masses of heavy holes and light holes ($0.27m_0$ and $0.014m_0$), the LH1-CB1 transition is well above the HH1-CB1 transition in energy.

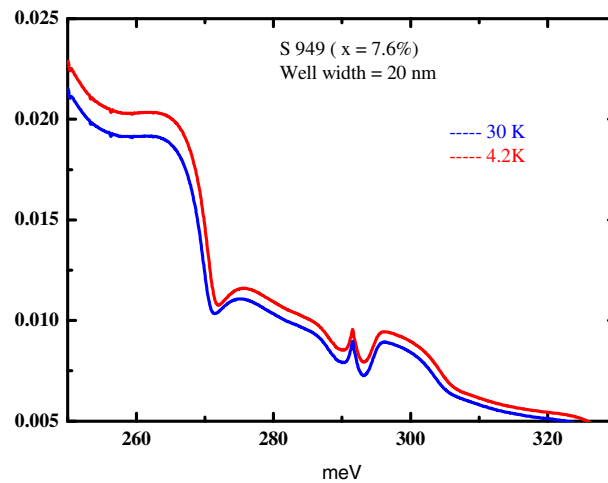


Figure 3.9: Transmission spectrum of an InSb/Al_xIn_{1-x}Sb MQW with Al concentration of 7.6% and well width of 20nm at 30K and 4.2K.

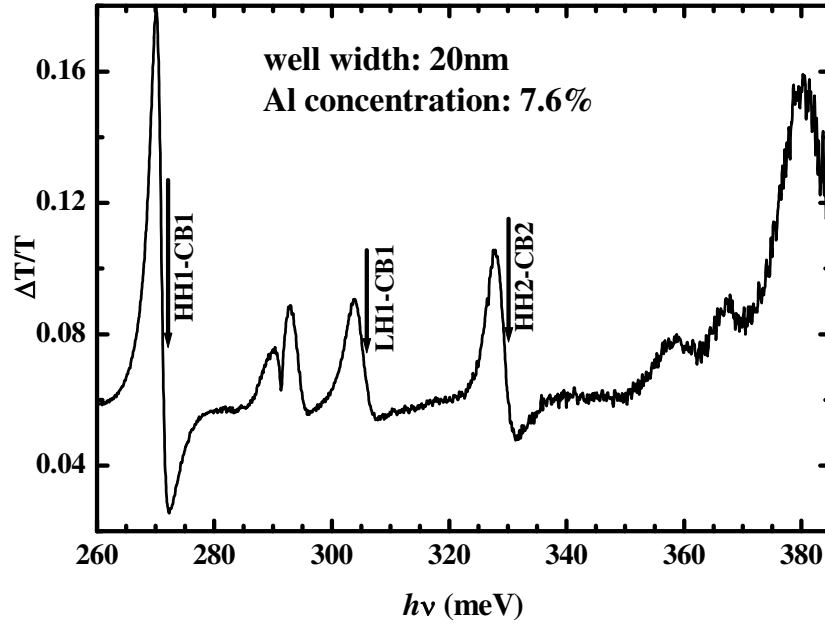


Figure 3.10: Differential transmission spectrum of the same sample in figure (3.9). The transmission difference, $T_{\text{MQW}}(4.2\text{K}) - T_{\text{MQW}}(22\text{K})$ relative to the average transmission T is plotted vs. photon energy. The features at 285-295 meV are artifacts due to carbon contamination on the sample surface.

3.5 Magneto-Optics Experiment Setup

3.5.1 Spectrometer and FTIR external light pipe

For the magneto-optics experiments we used a IFS 66V/S FTIR from Bruker Optics. This spectrometer consists with water-cooled mid infrared (MIR) source (glowbar) and water-cooled far infrared (FIR) source (Hg lamp). For the MIR experiments we used a KBr beam splitter with a spectral range $7500\text{-}370\text{ cm}^{-1}$. In

addition, this system has 1 μm and 6 μm thickness multilayer beamsplitters (680-30 cm^{-1}) and a 50 μm Mylar beamsplitter (spectral range 55-15 cm^{-1}) which are suitable for FIR experiments. The manufacture recommends that the MIR source (glowbar) should be left on at all times, so that it is available at all times and is always at a stable operating temperature. The estimated lifetime for the FIR source is about 400 hours. Therefore, the FIR source should probably only be turned on approximately 30 minutes before data collection. As shown in Figure 3.13 light is directed via a mirror box and light pipe. In our current set up, the mirror box and the external light pipe section that connects to the exit port cannot be evacuated. Therefore for this experiment we were not able to use the spectrometer's vacuum facility. We are constructing a new assembly for future work.

The light pipe used for the magneto-optics experiment is constructed from stainless steel and its entire interior surface is coated with gold. Polished gold has a reflectance coefficient of about 0.98 for infrared light. Before reaching the sample, the FIR light passes through three Winston cones (parabolic cones) which help to reduce the number of reflections and concentrate the light on the sample. The general structure of the light pipe/sample holder assembly is given in Figure 3.11. We used a CaF_2 window with a 1 inch diameter and 3° wedge to seal the top of the light pipe. The spectral range for CaF_2 is 0.1 -10 μm and it transmits 90% of light. For far infrared transmission experiments, the CaF_2 window can be replaced by a white polyethylene window. An additional step was taken to block the He-Ne laser beam illuminating the sample. To accomplish this, a Si window was stacked on top of the

CaF₂ window. Si is transparent to the IR radiation in the region of interest in these experiments.

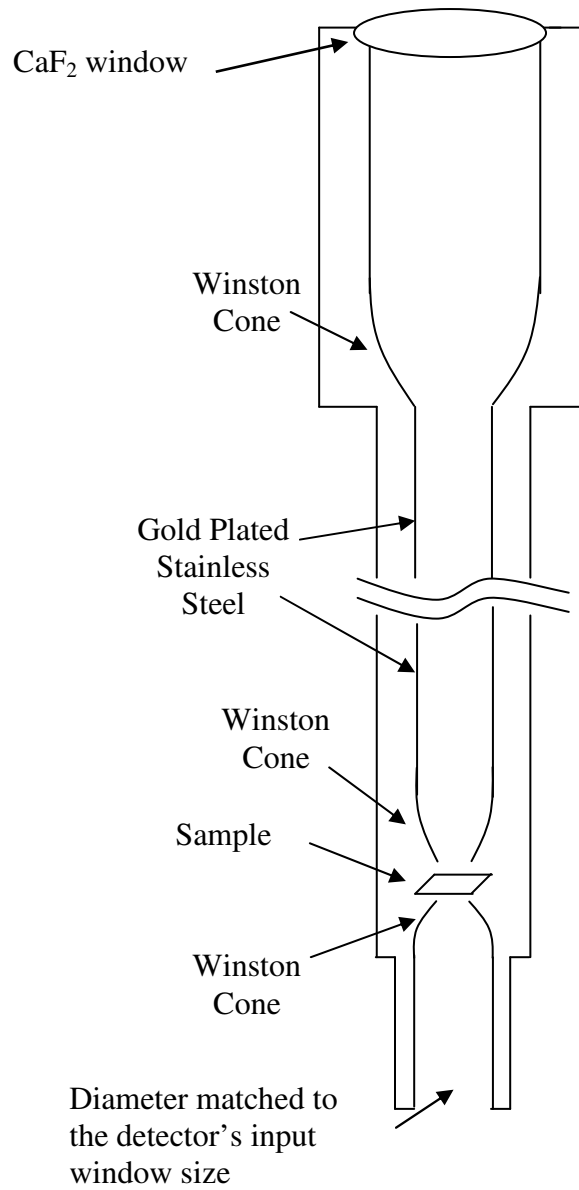


Figure 3.11: Part of Vacuum can/light-pipe assembly for the FTIR experimental setup.

3.5.2 The Superconducting Magnet

The magnet used for the magneto-optics experiments is located inside a cryogenic dewar. It is a Cryomagnetic Inc. Superconducting (NbTi) magnet that provides the maximum field of 7.7 Tesla at 4.2 K. The set maximum field, sweep rate and the sweep direction are controlled by a programming unit connected to the magnet power supply. To measure the strength of the field, the voltage across a shunt on the back of the power supply is measured and then converted to field units (969.3 Gauss/Ampere).

Steps in operating the magnet to avoid quenches are as follows:

- The power supply to the magnet should only be turned off when the magnetic field is zero.
- The direction of the magnet field can be changed using the switch box located in the far infrared lab. This should only be done when the power supply is off.
- The sweep rate should not exceed 0.1T per second. The sweep rate can be changed using a sensitive potentiometer.
- At low sweep rates, typically less than 0.05 Amp/sec, the programmer does not change the sweep direction. In this situation, one can first set the sweep rate to a higher value (but still not greater than 0.1 Tesla/sec) and then adjust it to a lower rate once the sweep direction has changed as desired.
- In order to operate the magnet at high fields, a sufficient amount of liquid Helium is required (typically a liquid helium level of 5cm above the top of the magnet).

- The magnet leads are vapor cooled. Therefore the holes on top of the leads should not be covered during magnet operation.

3.5.3 Cooling Down the System

Before pre-cooling the system one needs to make sure that the magnet is dry and the dewar's vacuum jacket is well evacuated. Then the magnet and the dewar can be pre-cooled by filling the dewar with liquid nitrogen the night before the experiment. About thirty liters of liquid nitrogen are required. The purpose of pre-cooling is to reduce the amount of helium needed to cool to 4K. The resistance of the magnet is monitored to track the cooling. The magnet resistance is about 600Ω at room temperature and drops to $70-77\ \Omega$ when it reaches to liquid nitrogen temperature (77K).

When the magnet is pre-cooled, the liquid nitrogen is removed by pressurizing the dewar with helium gas to force the liquid out through transfer tube. For this purpose it is especially important that the tube reach all the way to the bottom so that all the liquid nitrogen is removed. The next step is to fill the system with liquid Helium. Initially our system requires 25-30 liters of liquid helium in order to achieve a liquid helium level of 20cm as measured from the top of the magnet. During the initial liquid helium transfer, the resistance of the magnet should be monitored to observe when it drops to zero. It is important to perform this transferring process at a slow rate. Normally it takes about one hour for the initial transfer.

The vacuum can/light pipe assembly needs pre-cooling too. We first pump the assembly with a diffusion pump to at least 10^{-4} Torr. Then, the assembly is immersed in liquid nitrogen dewar for at least about twenty minutes. Finally, a small amount of helium exchange gas is inserted into the can. After that the vacuum can/light pipe assembly is placed inside the liquid helium filled magnet dewar and the experiment can be proceed.

3.5.4 Warming Up the System

Warming up the magnet can be done in two ways. The simplest method is to allow the remaining liquid helium in the magnet dewar to boil off and permit the magnet to warm up on its own. This method is attractive if there is no rush to use the setup again. If, however, a faster warm up is required, dry nitrogen gas can be circulated through the dewar, but only after the magnet has reached a temperature above 77 K (or approximately 100 Ω magnet resistance). Waiting until a reading of 100 Ω will prevent any nitrogen ice from forming at the base of the dewar. A heat gun can be used to warm up the vacuum can / light pipe. Note, caution must be taken to avoid an excessive amount of hot air near the indium seal at the base of the vacuum can between the vacuum can and the gold colored detector casing. After warming up the vacuum can/light pipe assembly for a while, we open a valve to release the helium gas.

3.5.5 Detector

An Indium Antimonide detector (Model: J10D-FP600765-R04M) from Judson Technologies was used in the magneto-optical experiments discussed above. The detector's operating temperature is in the range 4.2K-77K with the spectral range of 1.0 to 5.5 μm . InSb detectors are photovoltaic and generate a current when exposed to infrared radiation. A top view of the detector element is shown in Figure 3.12. The active area of the detector is 4mm diameter. The detector unit is sealed inside the vacuum can using indium wire. Before making the indium seal, the surface of the flange on the vacuum can and the flange on the detector should be cleaned using Methanol. A small amount of vacuum grease is applied on the indium wire before putting it in the indium groove. The eight 4-40 screws should be tightened in a symmetric star pattern in order to make the seal between the detector unit and the vacuum can. The assembly should then be checked for any leaks using a leak detector. The output of the detector is connected to a Judson preamplifier (PA-9) that is specifically matched to the InSb detector to provide maximum sensitivity, gain and bandwidth.

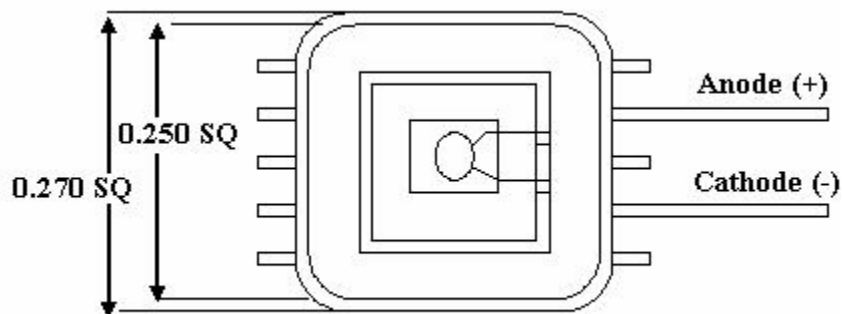


Figure 3.12: Top view of the detector unit.

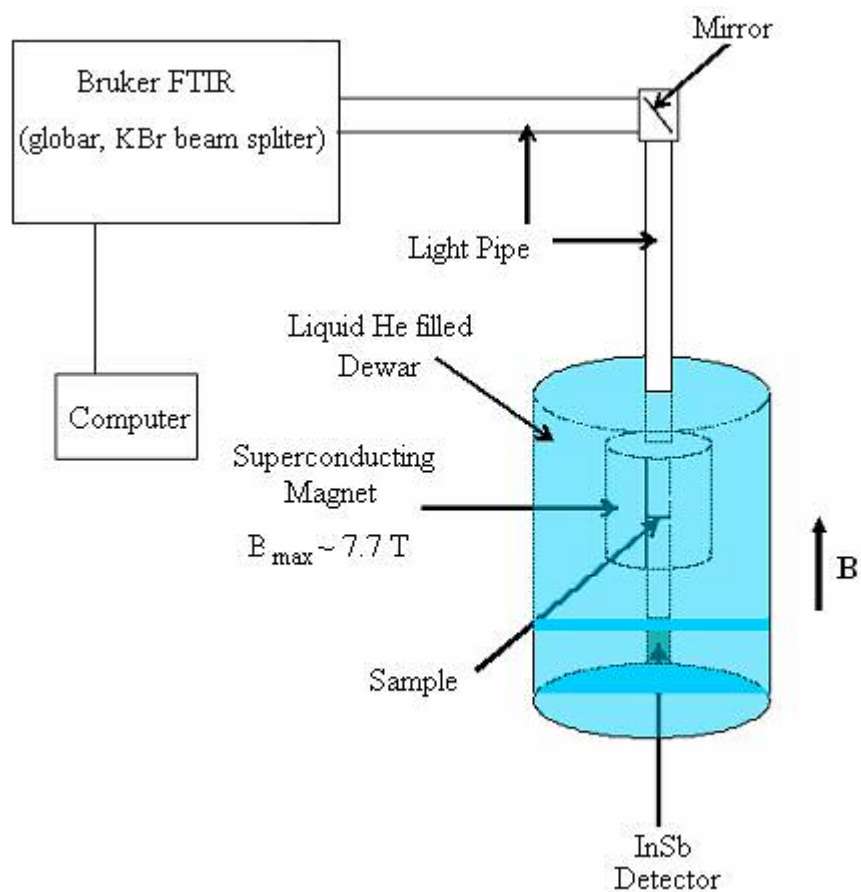


Figure 3.13: Schematic of the experimental setup. The sample is illuminated by a glowbar source via an internally gold-plated light pipe arrangement connected to the exit port of the FTIR.

Chapter 4

High Resolution X-Ray Diffraction

High resolution X-ray diffraction (HRXRD) is a standard method for the structural analysis of semiconductor thin films and heterostructures. The technique can be rapidly performed and usually does not damage the specimen. The diffraction pattern provides information on about the composition of an alloy layer, layer thickness, the built-in strain, and interface quality.

Figure 4.1 shows the experimental set up for a diffraction experiment. According to the figure, ω is the incident angle of the x-ray beam with respect to the sample surface and 2θ is the angular position of the detector with respect to the incident beam. The angular position 2θ is zero when a detector is positioned directly across from the x-ray source. The angles ϕ and ψ can be adjusted by rotating the sample about the y-axis and x-axis, respectively, to allow for a wide variety of diffraction planes. Results discussed in this thesis were carried out using a Philips HR-2 High Resolution Diffractometer with a four reflection Ge (220) incident beam monochromator and incident beam power of 1200 W. The unobstructed beam gives a detector count rate of 350,000 counts/second. All the scans and sample alignment were controlled using Philips PC-MRD epitaxy software. The minimum step size for ω and 2θ are 0.00025° and 0.001° , respectively. The incident x-ray wavelength is 1.54059 \AA , corresponding to the $\text{CuK}\alpha_1$ transition.

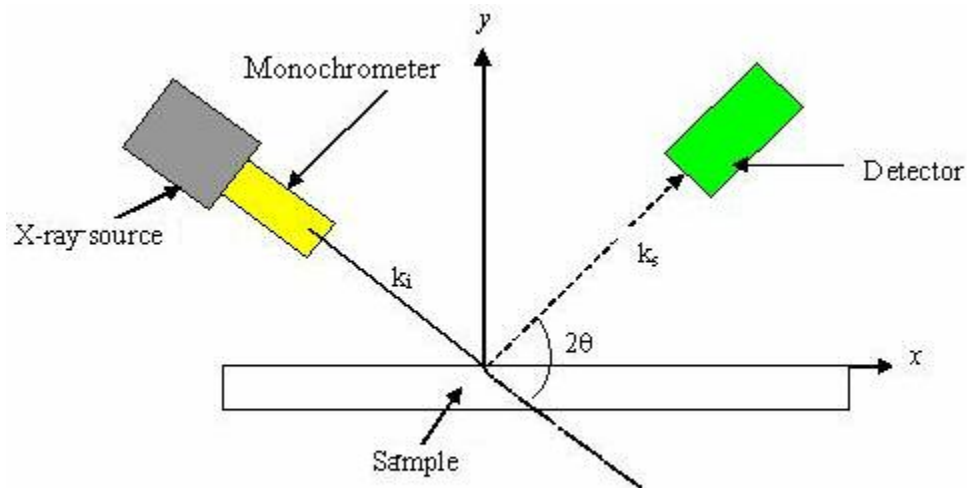


Figure 4.1: Experimental set-up for x-ray diffraction. A monochromatic x-ray beam with wavelength $\lambda = 1.5406\text{\AA}$ is projected onto a sample. k_i and k_s are incident and reflected wave vectors respectively. k_i is a constant for a given experiment, but ω and 2θ can be varied. The sample can also be rotated about the x-axis (ψ) and y-axis (ϕ).

4.1 Types of HRXRD Scans

Intensity data can be collected along four different diffractometer axes. The corresponding angles are

- Ω : rotation of the sample holder about the goniometer axis (z-axis)

- 2θ : rotation of the detector about the goniometer axis (z-axis)
- ψ : rotation of the sample about a horizontal axis parallel to the face of the sample stage (x-axis)
- ϕ : rotation of the sample about a horizontal axis perpendicular to the face of the sample stage (y-axis)

Generally Ω scans are performed for calibration of the apparatus and to determine the alloy composition. Scanning 2θ while leaving Ω fixed measures diffraction from different sets of lattice planes but with a fixed angle of incidence of the x-ray beam on to the sample. The ψ and ϕ axes movements are used to bring the P-vector (which is the direction normal to the sample surface) and S vector (which is any other vector of the sample which is not parallel to the P vector and lies in the horizontal plane) into the diffracting plane. In addition to the above scans, there are another two commonly use-coupled scans, in which the values of two axis parameters are varied simultaneously. These are $\Omega/2\theta$ and $2\theta/\Omega$ scans. For both scans the Ω drive is used to increase the angle between the incident beam and the reflecting planes and the 2θ drive is used to drive the detector around at double the speed. Both scans are identical in terms of diffractometer movement but the data collected is stored in a different way. Data files for $\Omega/2\theta$ scans contain intensity as a function of Ω and $2\theta/\Omega$ scans contain intensity as a function of 2θ . In our measurements we used $\Omega/2\theta$ scans.

4.2 Determination of Aluminum Composition

It is well known that the composition of a semiconductor alloy is a parameter of paramount importance because it determines the physical properties not only of the alloys but also of the epitaxial structures in which the alloys are incorporated. The physical properties of our InSb/Al_xIn_{1-x}Sb quantum wells depend on x, the aluminum concentration in the barrier layer. The amount of Al in the barrier affects the barrier height and the strain of the well. Table (4.1) shows the calculated barrier heights (V_s) for quantum wells with different Al compositions in the alloy layer. The barrier heights are calculated using the relation $V_s = (E_g^B - E_g^{well}) \times offset$ and offset has been obtained experimentally for InSb QW and is about 62% [37]. Here V_s , E_g^B and E_g^{well} are defined in Figure 1.4. For a given well width, the confinement of the electrons and holes in the quantum well can be tuned by varying the Al concentration, x. Therefore, an accurate determination of x in the alloy layer is important. Among the various techniques for the determination of the Al composition of the alloy layer, HRXRD is the most popular due to its high accuracy and nondestructive character. The aluminum concentration can be initially calibrated using the technique of RHEED (Reflection High-Energy Electron Diffraction) oscillations during molecular beam epitaxy.

Sample	Al Composition (nominal)	Barrier Height (meV)
T018	7%	87
T017	10%	115
T016	14%	174
T015	17%	212

Table 4.1: Barrier heights for 15nm quantum wells with different Al composition.

For this study we carried out both symmetric and asymmetric measurements. Symmetric reflections are from lattice planes parallel to the surface. They mainly contain information on sample parameters perpendicular to the surface like perpendicular lattice constants and layer thickness. Asymmetric reflections are from lattice planes that make an angle with the surface. These reflections contain information on both in-plane and perpendicular sample parameters and can be used to study strain relaxation of epitaxial layers.

The in-plane lattice parameter is the same as the perpendicular lattice parameter for fully relaxed layers and the in-plane lattice parameter is the same as the substrate lattice parameter for a fully strained layer. The perpendicular lattice parameter can be derived from a symmetric rocking curve.

In our samples, the InSb wells are strained to the lattice constant of the 2-3 μm $\text{Al}_x\text{In}_{1-x}\text{Sb}$ buffer layer. Therefore, the InSb wells are compressively strained by an amount that depends on the $\text{Al}_x\text{In}_{1-x}\text{Sb}$ composition. A detailed discussion of strain will be carried out in chapter (5).

4.2.1 Al composition from symmetric measurements

The Zincblende crystal structure of InSb and GaAs is discussed in Chapter 1. $\text{Al}_x\text{In}_{1-x}\text{Sb}$ is random alloy with a Zincblende structure and 100% of the basis pairs are Al and Sb and 100(1-x) of the basis pairs are In and Sb. We studied twelve samples with aluminum concentration of 4% through 20%. For each sample, intensity data were collected at four azimuthal angles in 90° intervals from 0° to 270°. For Zincblende structures, the strongest diffraction spots occur when h, k and l are all odd integers, such as (-1 -1 5) or all even integers with h+k+l divisible by four, such as (0 0 4). Figure (4.2) shows an example of an intensity plot as a function of angle of incidence of the (004) plane. The R and S peaks correspond to the $\text{Al}_x\text{In}_{1-x}\text{Sb}$ and GaAs layers. The thickness of the AlInSb layer is $\sim 2\mu\text{m}$. The broad peak is a set of unresolved MQW satellite peaks with expected spacing of 0.07°. The following section explains the procedure for determining the lattice parameter and alloy composition of the alloy layer.

The tetragonal lattice parameter perpendicular to the layer plane is given by

$$d = \frac{n\lambda}{2\sin(\theta_{\text{AlInSb}} + \Delta\theta)}. \quad (4.1)$$

Here θ_{AlInSb} is the peak position corresponding to the alloy layer and $\Delta\theta$ is the correction term that we make to the GaAs peak, which can be expressed as follows:

$$\Delta\theta = \theta_{GaAs}(\text{known}) - \theta_{GaAs}(\text{measured}) \quad (4.2)$$

Where $\theta_{GaAs}(\text{known})$ is the calculated value obtained by the solution of equation $2d\sin\theta = n\lambda$ using the known lattice constant of GaAs ($d = 5.6535 \text{ \AA}$) and $\theta_{GaAs}(\text{measured})$ is the measured angular position of the GaAs peak. By substituting $n = 4$, $\lambda = 1.5406 \text{ \AA}$, and $d = 5.6535 \text{ \AA}$ we obtain $\theta_{GaAs}(\text{known}) = 33.02^\circ$. An offset of $\sim 0.1^\circ$ is common because the sample, which is mounted on the goniometer using double-sided tape, is not perfectly flat against the stage. The next step is to determine the composition value from the relaxed lattice parameters under the assumption of Vegard's law [38]. Vegard's law postulates a linear relationship between the relaxed lattice constant and the composition x , and can be expressed as:

$$a_{(Al_xInSb_{(1-x)})} = a_{InSb}(1-x) + a_{AlSb}x. \quad (4.3)$$

Where a_{alloy} , a_{InSb} and a_{AlSb} are the lattice parameters for alloy, InSb and AlSb respectively. By substituting $a_{InSb} = 6.4794 \text{ \AA}$, $a_{AlSb} = 6.136 \text{ \AA}$ [15] in equation 4.3, the alloy composition can be calculated. Calculated parameters for the four different (004) scans corresponding to sample rotations of $\Phi = 0^\circ, 90^\circ, 180^\circ$, and 270° are listed in Table (4.2). The calculated lattice constant (a_{alloy}) is nearly equal between the four scans.

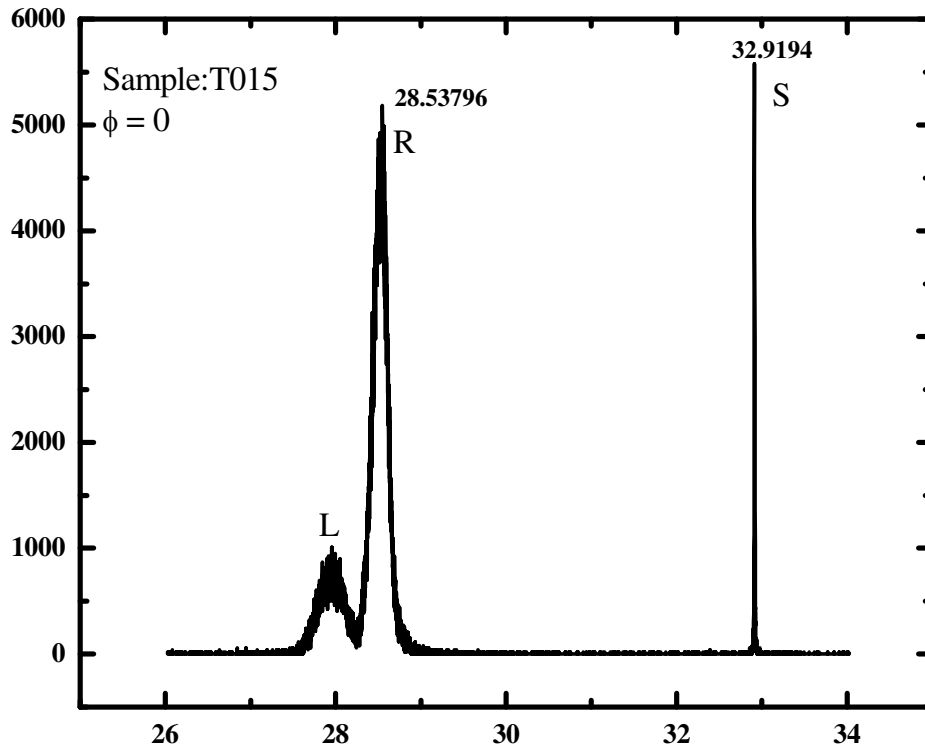


Figure 4.2: The experimental (004) rocking curve from a 15nm MQW sample with 50 nm barrier layers. The S and R peaks correspond to the GaAs substrate and $\text{Al}_x\text{In}_{1-x}\text{Sb}$ buffer layers, respectively. The L peak is a set of unresolved MQW satellite peaks with expected spacing of 0.07° .

Sample name and nominal Al %	Diffraction Plane and sample orientation	Calculated out-of-plane lattice parameter (Å)	Average Al (%)
S809 (x = 8%)	(004), $\phi = 0^\circ$ (004), $\phi = 180^\circ$ (004), $\phi = 90^\circ$ (004), $\phi = 270^\circ$	6.4527 6.4533 6.4537 6.4556	(a)7.7
			(b)7.2
S810 (x = 12%)	(004), $\phi = 0^\circ$ (004), $\phi = 180^\circ$ (004), $\phi = 90^\circ$ (004), $\phi = 270^\circ$	6.4357 6.4360 6.4354 6.4344	(a)12.6
			(b)12.9
S812 (x = 16%)	(004), $\phi = 0^\circ$ (004), $\phi = 180^\circ$ (004), $\phi = 90^\circ$ (004), $\phi = 270^\circ$	6.4237 6.4237 6.4240 6.4220	(a)16.2
			(b)16.4
S813 (x = 20%)	(004), $\phi = 0^\circ$ (004), $\phi = 180^\circ$ (004), $\phi = 90^\circ$ (004), $\phi = 270^\circ$	6.4054 6.4062 6.4112 6.4027	(a)21.4
			(b)21.0

Table 4.2: Lattice parameters and Al compositions obtained from (004) x-ray measurement for 10 nm MQW samples. In the fourth column, (a) represents the average composition value determined from $\phi = 0^\circ$ and $\phi = 180^\circ$ scans and (b) corresponds to the average composition value obtained from $\phi = 90^\circ$ and $\phi = 270^\circ$ scans.

4.2.2 Al composition from asymmetric measurements

When we derive the Al composition from symmetric reflections, we assume that the layer is fully relaxed. In the case of fully relaxed layers, it is sufficient to measure one of the lattice constants, usually c , to calculate the Al content. For strained layers this is no longer true. In this situation, a change of the lattice constants due to biaxial stress must be taken into account. To separate the influence of strain and composition on the lattice constants, both in-plane and out-of-plane lattice parameters, a and c , have to be determined. In the strained films, c and a are connected via the Poisson ratio.

We carried out $(-1\ -1\ 5)$ asymmetric reflection measurements to determine in-plane and out-of-plane lattice parameters. Measurements were taken at $\phi = 0^\circ$ and $\phi = 180^\circ$ for each sample. For our samples, the alloy peak and the substrate peak are separated far. Therefore each asymmetric “scan” needed two separate scans: one for the epi layer and one for the substrate. Figure 4.3 shows a typical rocking curve recorded from one of the multiple quantum well structures studied. In Figure (4.3a), the left peak corresponds to the quantum well structure and the right peak is due to the alloy layer. Figure 4.3b shows the peak due to the GaAs substrate. From these two peaks we then obtain the peak separation (between alloy and substrate) which is the most important parameter for the calculation.

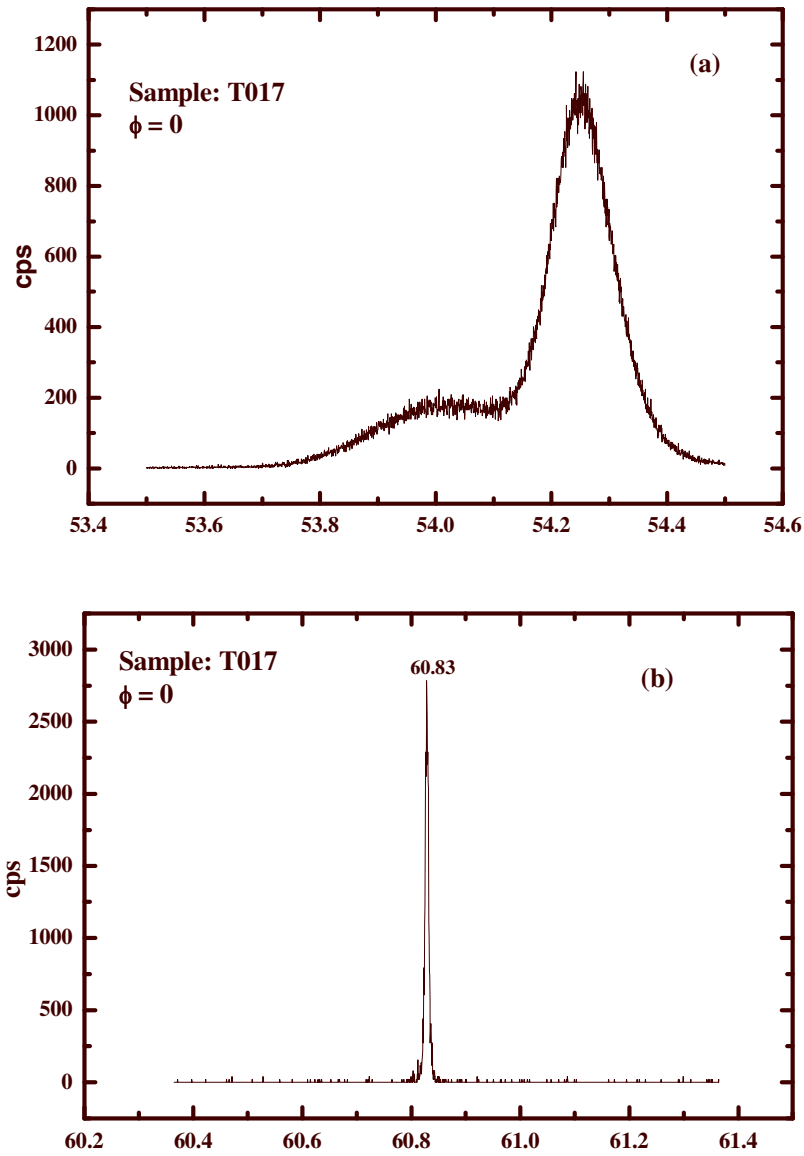


Figure 4.3: Rocking curves from (-1, -1, 5) measurements.

A tilt of the entire epitaxial structure with respect to the substrate can occur in semiconductor epitaxial growth if the substrate surface is slightly misoriented from [001] [39]. The presence of misfit dislocations and the finite thickness are responsible for a broadening of the layer peaks. The next paragraph explains the procedure of calculating tilt angle and lattice parameters using peak separation. One can find a detailed explanation of this calculation elsewhere [40].

The spacing d , the Bragg angle (θ) and the tilt angle for an HHL reflection (ϕ) are given by

$$\frac{1}{d} = \frac{2 \sin \theta}{\lambda} = \sqrt{\left(\frac{2H^2}{a^2} + \frac{L^2}{c^2} \right)} \quad (4.3)$$

and

$$\cos \phi = \frac{L/c}{\sqrt{\left(\frac{2H^2}{a^2} + \frac{L^2}{c^2} \right)}} \quad (4.4)$$

From equations (4.3) and (4.4) we obtain

$$c = \frac{\lambda L}{2 \sin \theta * \cos \phi} \quad \text{and} \quad a = \frac{cH}{L} \sqrt{2} * \cot \phi \quad (4.5)$$

First, the substrate Bragg angle (θ_S) and the tilt of the (-1 -1 5) plane (ϕ_S) with respect to the (001) surface are calculated by setting $a = c = 5.6535 \text{ \AA}$ (i.e. the lattice parameter of GaAs) and $\lambda = 1.54056 \text{ \AA}$. From the calculation we obtain $\theta_S = 45.0688^\circ$ and $\phi_S = 15.7932^\circ$. As mentioned earlier, we measure the separation between the layer

and the substrate peak at $\phi = 0^\circ$ and $\phi = 180^\circ$ positions. The Bragg angle difference between the layer and substrate is given by the average of the peak positions. Hence the Bragg angle for the layer can be expressed as:

$$\theta_L = [(\theta_S^\circ) - (\text{Peak separation})].$$

When there is a tilt between the layer and substrate planes the tilt (α) is given by half the difference in the two peak separations [40].

$$\text{i.e. tilt angle}(\alpha) = \frac{1}{2} [(\text{Peak separation at } \phi = 180^\circ) - (\text{Peak separation at } \phi = 0^\circ)]$$

As the layer has a larger d spacing, the tilt of the layer plane with respect to the (001) surface (ϕ_L) is greater than that for the substrate and is given by:

$$\phi_L = [(\phi_S = 15.7932^\circ) + \alpha].$$

Then, from $c = \frac{\lambda L}{2 \sin \theta_L * \cos \phi_L}$ and $a = \frac{cH}{L} \sqrt{2} * \cot \phi_L$ we determine the lattice parameters a and c .

The fully relaxed lattice parameter of the layer, a_L (relaxed), is the value that we need to use in Vegard's law to find the composition of the layer. a_L (Relaxed) can be expressed in terms of a , c and Poisson ratio ν [41]

$$a_L = c \left[1 - \left(\frac{2\nu}{1+\nu} \right) \left(\frac{c-a}{a} \right) \right]. \quad (4.6)$$

The Poisson ratio is defined using the elastic constants C_{ij} as:

$$\nu = \frac{C_{12}}{C_{11} + C_{12}}. \text{ For InSb } C_{11} = 6.669 \text{ and } C_{12} = 3.645 \text{ [15]. Results obtained for}$$

20nm MQW samples from asymmetric measurements are listed in Table (4.3). The

percentage relaxation (R %) is calculated using $R = \left(\frac{a - a_0}{a_L - a_0} \right) \times 100$. Where a_0 is the

lattice parameter of the substrate, i.e. GaAs in our case, and a_L is defined in equation

4.6.

Sample Name	Nominal Al %	Lattice parameters (Å)	Calculated a_L(Å)	Calculated R%	Calculated Al %
S948	5	c = 6.4706 a = 6.4607	6.4654	99.4	4.1
S949	8	c = 6.4566 a = 6.4500	6.4531	99.6	7.6
S953	11	c = 6.4453 a = 6.4424	6.4438	99.8	10.3
S954	14	c = 6.4357 a = 6.4329	6.4343	99.8	13.1

Table 4.3: Lattice parameters and Al compositions obtained from (-1-15) x-ray measurement for 20 nm MQW samples.

4.3 Determination of Aluminum concentration using alloy gap

Previously, N. Dai et al. [36] carried out studies of alloy band gap as functions of aluminum concentration and temperature. In that study, they measured the band gap of bulk $\text{Al}_x\text{In}_{1-x}\text{Sb}$ with an FTIR spectrometer and the lattice constants (or, equivalently, the Al composition) using XRD. They reported a linear relationship for the band gaps and it is given by

$$E_g(\text{alloy}) = E_g(\text{InSb}) + E'_g \Delta a, \quad (4.7)$$

where E'_g ($\text{eV}/\text{\AA}^\circ$) is the measured slope and $\Delta a = (a_{\text{alloy}} - a_{\text{InSb}})$. The value of Δa was deduced from the separation between the peaks of the alloy and InSb in a rocking curve. From this separation one can determine the aluminum concentration through Vegard's law. Application of Vegard's law for the InSb/ AlSb alloy system:

$$a(\text{alloy}) = a_{\text{InSb}}(1-x) + a_{\text{AlSb}}x \quad \text{with} \quad a_{\text{InSb}} = 6.479 \text{ \AA}, \quad a_{\text{AlSb}} = 6.136 \text{ \AA}$$

$$\text{Yields} \quad \Delta a = 0.343x \text{ \AA} \quad (4.8)$$

From equations (4.7) and (4.8) we obtain

$$E_g(\text{alloy}) = E_g(\text{InSb}) + E'_g(0.343)x. \quad (4.9)$$

Therefore, using equation (4.9) one can determine the Al composition from the position of the measured absorption edge of the alloy.

Temperature (K)	E_g (InSb) (eV)	E_g' (eV/Å)
4.2	0.240±0.002	6.01±0.03
77	0.234±0.002	6.01±0.03
300	0.183±0.002	5.76±0.03

Table 4.4: Values of InSb gap and E_g' at 4.2,77 and 300K.

Using the above procedure we determined the alloy composition for 10nm, 15nm and 20nm MQW samples. Figure 4.4 represents the differential transmission spectra for 15nm sample with 7% Al in the barrier (sample T018). As discussed in reference 6, the position of the alloy absorption edge was determined by the high-energy point of steepest slope. Other features in the spectra will be discussed in chapter (5). Alloy gaps and composition values for the studied 15 nm samples are tabulated in Table 4.5.

Sample name	Nominal Al (%)	Observed alloy band gap (meV)	Calculated Al (%)
T018	7	382	6.9
T017	10	451	10.2
T016	14	535	14.3
T015	17	603	17.6

Table 4.5: Alloy gaps and Al concentration values for the 15nm MQW samples.

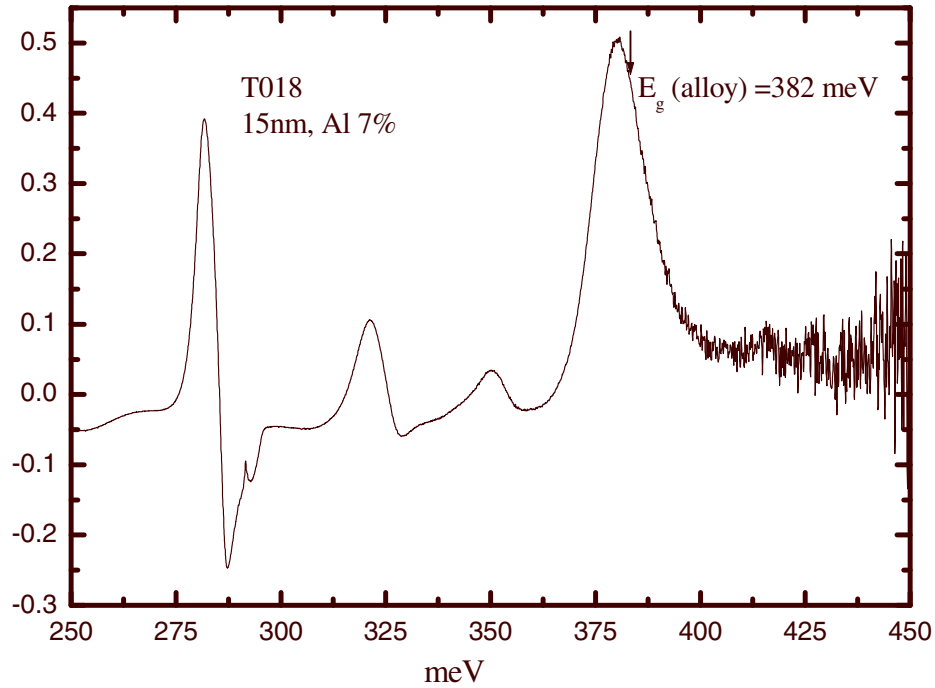


Figure 4.4: Differential transmission spectra of 15nm well. Absorption due to the alloy gap is clearly seen. The other peaks are due to exciton transitions.

Al compositions obtained from asymmetric and symmetric diffraction planes and from using alloy gap values are summarized in Table 4.6. Uncertainties in the measurements are based on the uncertainty in the assignment for peak maxima. Thus, the minor discrepancy in the determined concentration values from three different measurements is due to the width of the peaks, which makes determination of maxima difficult. However, the composition values obtained from x-ray diffraction

measurements and from FTIR measurements are within 10% of those determined from the growth conditions (nominal value).

Sample Name	Al % Nominal	Al % Calculated		
		From (-1,-1,5) Reflection	From (0,0,4) Reflection	From FTIR data (using alloy gap)
T018	7	6.7	6.4	7.0
T017	10	9.7	9.7	10.2
T016	14	15.0	14.3	14.3
T015	17	17.8	18.6	17.9

Table 4.6: Al composition obtains from three different measurements for samples with well width 15nm.

In summary, the composition of the alloy layer was obtained using HRXRD and FTIR measurements. Al composition obtained from three different measurement techniques agrees well with the attempted (nominal) alloy composition value.

Chapter 5

Determination of Strain Parameters

In this chapter, we study the effects of residual strain in InSb epitaxial films using the spectroscopic method. We use interband exciton transitions in InSb/Al_xIn_{1-x}Sb multi quantum-well samples to determine the heavy-hole and light-hole energy gaps as the strain is varied using Al concentrations up to 20%. The gaps are compared to deformation-dependent calculations of the energy gaps in the presence of biaxial strain to obtain a measure of the deformation potentials a and b .

5.1 Strain effects on the Band Alignment

One of the semiconductor heterostructures most widely studied in the past is GaAs/ Al_xGa_{1-x}As. Since this material system is nearly lattice matched, no limitations by the growth with respect to the well thickness or the Al concentration in the barrier occur. However, the application of AlGaAs/GaAs quantum well structures in optoelectronic devices is somewhat limited. In 1982 Osborn [42] proposed that the strained-layer structure might display new electronic and optical properties not seen in the unstrained materials. Since then, strained-layer technology, science, and applications have become a field of activity for many laboratories. The removal of the lattice constant matching constraint considerably increased the number of material systems that could be considered for obtaining quantum wells (QWs) and Superlattices (SLS). Moreover, III-V compound semiconductors have been

increasingly important during the last decade as materials for optoelectronics and high-speed device application. Motivated by the demand for optoelectronics devices, new binary, ternary or even quaternary material systems like InAs/GaAs, InAs/InP, InGaAs/GaAs, InGaAs/InP, InGaAsP/InP have been studied [43-47]. Except in particular composition, these material systems all have in common that they are not lattice matched. Different alloys in the heterostructures have different atomic spacing, hence different lattice constants. Due to the different lattice constant of well and barrier material, the atomic arrangement in the unit cell of the well material is distorted and the well material has incorporated strain. Strain can be either tensile or compressive depending on whether the lattice constant of the well material is smaller or larger than the barrier material. This is illustrated in Figure 5.1. According to the Figure 5.1b, an InSb layer with a lattice constant a_L is grown on a AlInSb layer with a lattice constant a_s . In this situation, the InSb layer is strained such that the lattice constant along the plane of the layer is equal to a_s .

The strain can have strong effects on the electrical and optical properties of the epilayer. The strain affects key material properties of semiconductor including energy gap and effective mass of an electron.

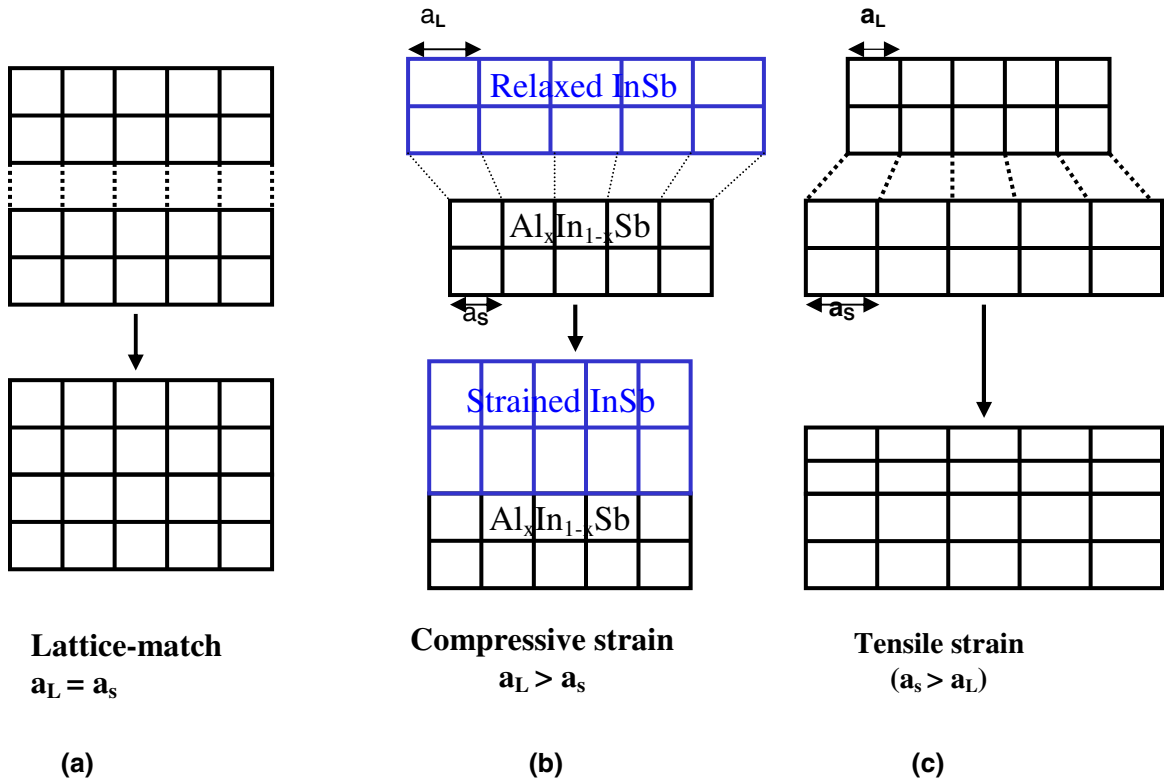


Figure 5.1: Lattice distortion in a strained-layer structure. (a) Lattice-match (b) compressive strain (c) tensile strain

Generally, the strain tensor depends on the crystal symmetry and the substrate orientation during growth. With the [001] direction as the growth direction a simple strain tensor is obtained, since the off-diagonal elements vanish ($\epsilon_{xy} = \epsilon_{xz} = \epsilon_{yz} = 0$).

The remaining strain components are defined as [48]

$$\epsilon_{xx} = \epsilon_{yy} = \epsilon_{\parallel} = \frac{a_s - a_L}{a_L} \quad \text{and} \quad (5.1)$$

$$\varepsilon_{zz} = \varepsilon_{\perp} = -2 \frac{C_{12}}{C_{11}} \varepsilon_{\parallel} \quad (5.2)$$

Here ε_{\parallel} and ε_{\perp} represent the strain components parallel and perpendicular to the interface, which are related by the elastic constants C_{12} and C_{11} .

For our samples $a_s = a_{\text{alloy}} = a_{\text{InSb}} (1-x) + a_{\text{AlSb}} (x)$ (according to the Vegard's law) and $a_L = a_{\text{InSb}}$. Where a_{InSb} and a_{AlSb} are lattice parameters of bulk InSb and bulk AlSb.

Because strain accumulates with increasing thickness, layers cannot be grown coherently up to any extent [49]. From the so-called critical layer thickness on, strain cannot be accommodated in an elastic deformation of the unit cell anymore and the lattice relaxes by the incorporation of dislocations. At this point the lattice constant of the film relaxes toward the unstrained value. Since dislocations severely degrade the morphological and optical quality of the strained layer [48], the thickness of strained quantum wells has to be kept below the critical layer thickness, which decreases as the lattice mismatch increases. The model of Matthews and Blakslee predicts the equilibrium critical thickness for a mismatch epitaxial layer [50]. Using their treatment one can determine how thick an epilayer can be grown before relaxation begins. Following above model, T. D. Mishima *et al.* predict the critical thickness for InSb/Al_{0.09}In_{0.91}Sb system as $\sim 300 \text{ \AA}$ [51].

5.2 Deformation Potentials

Background

As discussed earlier, the strain can have strong effects on the electrical and optical properties of the epilayer. The strain affects key material properties of the semiconductor including the energy gap and effective mass of an electron. Near $k=0$ the modifications of the electronic structure under the presence of strain can be described by deformation potential theory. The parameters, which describe the relationship between the lattice strain and the electronic band structure, are known as deformation potentials, and the accurate measurements of these quantities are important for understanding the band structure of semiconductor devices. In general, the strain induced by the lattice-mismatched epitaxial growth can be decomposed into uniaxial and hydrostatic contributions. The isotropic or hydrostatic component of strain in a material changes the volume of the crystal without disturbing the crystal symmetry. The band gap of the strained material is increased by the hydrostatic component, which leads to an energy shift of both the conduction band and valence band edges. The energy shifts induced by the hydrostatic strain components can be expressed as [52, 53]

$$\delta E_{H,c} = a_c \left(\frac{\Delta\Omega}{\Omega} \right) \text{ and } \delta E_{H,v} = a_v \left(\frac{\Delta\Omega}{\Omega} \right). \quad (5.3)$$

Here a_c and a_v are the hydrostatic deformation potentials for the conduction and valence bands and $\left(\frac{\Delta\Omega}{\Omega} \right)$ is the fractional volume change.

$$\left(\frac{\Delta\Omega}{\Omega}\right) = (\varepsilon_{xx} + \varepsilon_{yy} + \varepsilon_{zz}) = (2\varepsilon_{xx} + \varepsilon_{zz}) = \left(2 - 2\frac{C_{12}}{C_{11}}\right)\varepsilon_{//}. \quad (5.4)$$

ε_{xx} and ε_{zz} are defined in equations (5.1) and (5.2) and $C_{12} = 0.5 C_{11}$. For compressive strain, the in-plane strain is negative.

On the other hand, uniaxial or the shear components of the strain split the valence band and reduce the crystal symmetry. For the strain-free case the conduction band minimum is formed by two-fold degenerate states $|J=1/2, \pm 1/2\rangle$. The valence band structure is decomposed by a four-fold states $|J=3/2, M_J = \pm 3/2, \pm 1/2\rangle$ at the top of the valence band, and the spin-orbit split-off band $|J=1/2, \pm 1/2\rangle$. As mentioned earlier, strain modifies both the conduction and valence band structures. The valence band undergoes the most dramatic change in character. The shear strain component induces a splitting between the heavy-hole and light-hole energy bands. Figure 5.2 illustrates the band diagram for the strain-free and strain cases.

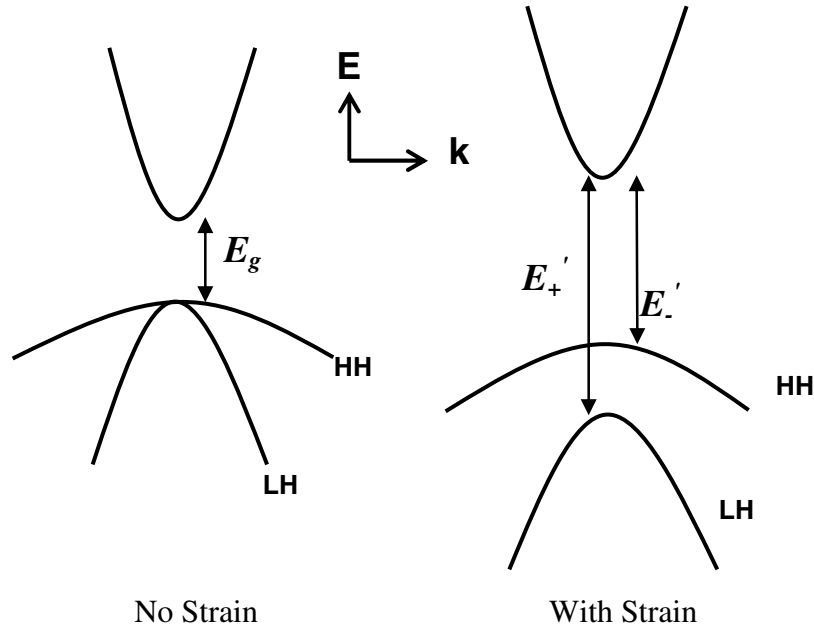


Figure 5.2: The heavy-hole and light-hole gaps for strain-free and strained InSb at the center of Brillouin zone (Γ point). Note that the gaps increase and that the degeneracy of the heavy hole and the light hole bands is lifted under biaxial compressive strain.

The energy shifts due to in-plane strain can be described in terms of the deformation potentials and elastic constants C_{ij} . In Zinc-blende semiconductors, the hydrostatic deformation potentials a_c (conduction band), a_v (valence band), and the shear deformation potential b are used. a_c and a_v are hydrostatic components of the energy shift on the conduction band and valence bands, respectively. In terms of the above quantities, the shifts in band energies have three main components: $\delta E_{H,c}$ and $\delta E_{H,v}$ for hydrostatic effects, and $\delta E_S^{(001)}$ for shear effects on the conduction and

valence bands. These terms describe the new conduction and valence band gaps by [52, 53, and 54]

$$E_g^{hh} = E_0 + \delta E_{H,c} + \delta E_{H,v} + \delta E_S^{(001)} \quad (5.5)$$

$$E_g^{lh} = E_0 + \delta E_{H,c} + \delta E_{H,v} + \frac{\Delta_0}{2} \left(1 - \frac{\delta E_S^{(001)}}{\Delta_0}\right) - \frac{\Delta_0}{2} \left[1 + 2 \frac{\delta E_S^{(001)}}{\Delta_0} + 9 \left(\frac{\delta E_S^{(001)}}{\Delta_0}\right)^2\right]^{\frac{1}{2}}. \quad (5.6)$$

where $\delta E_{H,c} = a_c \left(2 - 2 \frac{C_{12}}{C_{11}}\right) \varepsilon_{//}$, $\delta E_{H,v} = a_v \left(2 - 2 \frac{C_{12}}{C_{11}}\right) \varepsilon_{//}$, $\delta E_S^{(001)} = -b \left(1 + 2 \frac{C_{12}}{C_{11}}\right) \varepsilon_{//}$,

Δ_0 is the spin-orbit splitting at $k = 0$, and E_0 is the unstrained band gap. Expanding

the last term of equation (2) to first order in $\frac{\delta E_S^{(001)}}{\Delta_0}$ yields the following expressions:

$$E_g^{hh} = E_- = E_0 + \left[a \left(2 - 2 \frac{C_{12}}{C_{11}}\right) - b \left(1 + 2 \frac{C_{12}}{C_{11}}\right)\right] \varepsilon_{//} \quad (5.7)$$

$$E_g^{lh} = E_+ = E_0 + \left[a \left(2 - 2 \frac{C_{12}}{C_{11}}\right) + b \left(1 + 2 \frac{C_{12}}{C_{11}}\right)\right] \varepsilon_{//} - \frac{9}{4\Delta_0} b^2 \left(1 + 2 \frac{C_{12}}{C_{11}}\right)^2 \varepsilon_{//}^2. \quad (5.8)$$

Here a is the sum of the conduction and valence band deformation potentials i.e. $a = a_c + a_v$ and $\varepsilon_{//}$ is the in-plane strain given by:

$$\varepsilon_{//} = \frac{\delta a}{a} = \frac{a_{strained} - a_{bulk}}{a_{bulk}} = \left(\frac{a_{InSb} (1-x) + a_{AlSb} x - a_{InSb}}{a_{InSb}} \right) = x \left(\frac{a_{AlSb} - a_{InSb}}{a_{InSb}} \right). \quad (5.9)$$

By using thermal expansion data [15] we find the 0 K values for $a_{InSb} = 6.473 \text{ \AA}$ and $a_{AlSb} = 6.132 \text{ \AA}$. Using Vegard's law, valid for $\text{Al}_x\text{In}_{1-x}\text{Sb}$, one finds that the in-plane strain at 0 K is given by $\varepsilon_{//} = (-0.0527) x$, where x is the Al concentration. We note

that for a compressive strain ε is negative and for InSb, both “ a ” and “ b ” are negative. Therefore both heavy hole and light hole gaps are increased.

Most of the reported deformation potential values (“ a ” and “ b ”) for well-studied semiconductors are from theoretical calculations [15]. The agreement among the numbers obtained from different methods of model calculations and experiments is poor. Table 5.1 shows the reported hydrostatic (a) and shear (b) deformation potential parameters for some selected Zincblende type semiconductors. These parameters have been measured by a variety of optical and transport experiments [54]. For InSb, reported “ a ” values ranges from 7.3 to 10.3 eV and there is only one reported “ b ” value [15]. The major obstacle in experimentally determining deformation potentials in semiconductors is the difficulty in controlling strain in the material system. Therefore one needs to have a material system in which strain can be determined accurately along with the ability to measure some parameters that are strain-dependent through the deformation potentials. The strained InSb/AlInSb quantum wells provide an ideal setting for measuring the deformation potentials.

	a (eV)	b (eV)
GaAs	-9.77	-1.7
	-6.70	-2.0
	-8.46	-2.0
	-9.43	
	-6.36	
InAs	-6	-1.8
	-5.7	
	-5.9	
	-6.9	
GaSb	-8.3	-1.8
	-8.28	-2.0
	-8.2	
	-7.9	
	-8.3	
AlSb	-5.9	-1.35
	-2.0	
	-0.9	
InSb	-7.7	-2.05
	-7.6	
	-7.5	
	-8.0	
	-10.3	

Table 5.1: Hydrostatic and Shear deformation potential parameters for some selected semiconductors [54, 15].

5.3 Samples

Our samples are multi quantum-well (MQW) InSb/AlInSb heterostructures grown by molecular beam epitaxy (MBE) on (001) semi-insulating GaAs substrates. In order to reduce mismatch dislocations (there is 14% mismatch between GaAs and InSb lattices), a thick buffer layer is grown prior to the growth of the quantum well structure. The buffer layers contained AlSb, GaSb, $\text{Al}_x\text{In}_{1-x}\text{Sb}$ with graded x , and/or an InSb/ $\text{Al}_x\text{In}_{1-x}\text{Sb}$ strained layer superlattice. A 2-3 μm $\text{Al}_x\text{In}_{1-x}\text{Sb}$ layer, which is

almost completely relaxed, was grown just prior to the MQW layers. The InSb wells are strained to the lattice constant of the 2-3 μm $\text{Al}_x\text{In}_{1-x}\text{Sb}$ layer. Therefore, the InSb wells are compressively strained by an amount that depends on the $\text{Al}_x\text{In}_{1-x}\text{Sb}$ composition. For the measurements described here, we have chosen a sequence of 25 to 40 nominally undoped InSb MQWs with different well thicknesses (10nm, 15nm, and 20nm). The alloy barriers are 50nm thick. The samples had nominal aluminum concentrations of $x = 0.08$ to 0.20 for the 10 nm samples, $x = 0.07$ to $x = 0.17$ for 15 nm samples and $x = 0.05$ to $x = 0.14$ for 20 nm samples. With the change of Al concentration in the barrier layers, the strain in the quantum well system can be tuned continuously. Samples with higher aluminum concentrations were not grown because it was necessary that all the layers were within the region where strain is accommodated by elastic deformation rather than misfit dislocations.

Figure 5.3 shows the differential transmission spectra of 4 samples measured at low temperature ($\Delta T = 4.2\text{K}-30\text{K}$). These four samples have the same well thickness (20nm), the same barrier thickness (50nm) and different Al composition in the barrier ($x = 0.05, 0.08, 0.11, 0.14$). One remarkable feature is that the spectroscopic position of the HH1-CB1 exciton transition shifts to higher energy as x_{Al} increases from 0.05 to 0.14, showing a strain effect. Also we can see that the spectra of HH1-CB1 resonances show broadening. Possible causes for this broadening can be explained as follows. Generally, exciton peaks are broadened due to structural effects (inhomogeneous) and finite lifetime effects (homogeneous). Structural or inhomogeneous effects are temperature independent. The causes for inhomogeneous

broadening are interface roughness, alloy potential fluctuations, point and dislocation defects, and background impurity broadening [29]. Acoustic phonon scattering and optical phonon scattering are the sources for homogeneous broadening. The excitons in our samples are localized in InSb quantum well. Therefore, the compositional fluctuation can be neglected. Thus, we expect that the major contributions to inhomogeneous broadening coming from the interfacial roughness and ionized impurities [55].

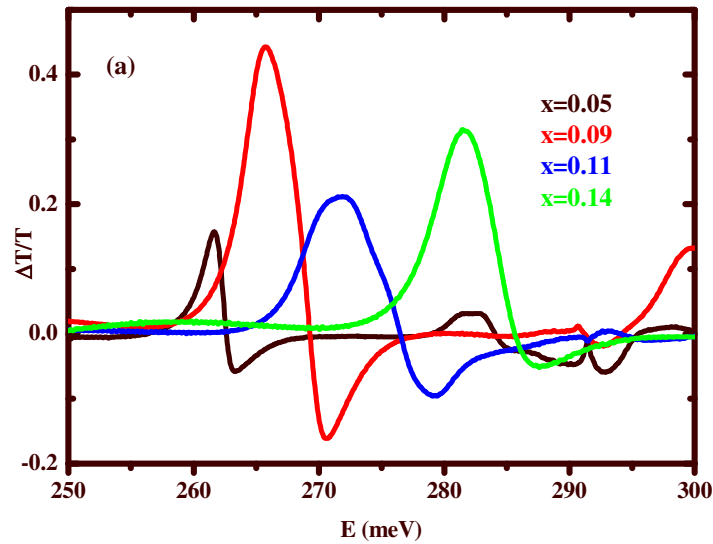


Figure 5.3: Differential transmission spectra (not normalized) for 20nm samples with different Al concentration. When the Al composition increases, the exciton absorption peak shifts to higher energy.

Figure 5.4 shows the differential transmission spectra for InSb/Al_{0.14}In_{0.86}Sb multiple quantum wells with well widths of 15nm and 20nm. Each sample shows two series of strong peaks, one involving heavy-hole sub-bands and other light-hole subbands. Due to the quantum confinement effect, the splitting energies between HH1-CB1 and LH1-CB1 transitions, ΔE_{HL} , decrease as the well width increases. For an example, in Figure 5.4, ΔE_{HL} is 73 meV for 15nm and 59meV for 20nm sample.

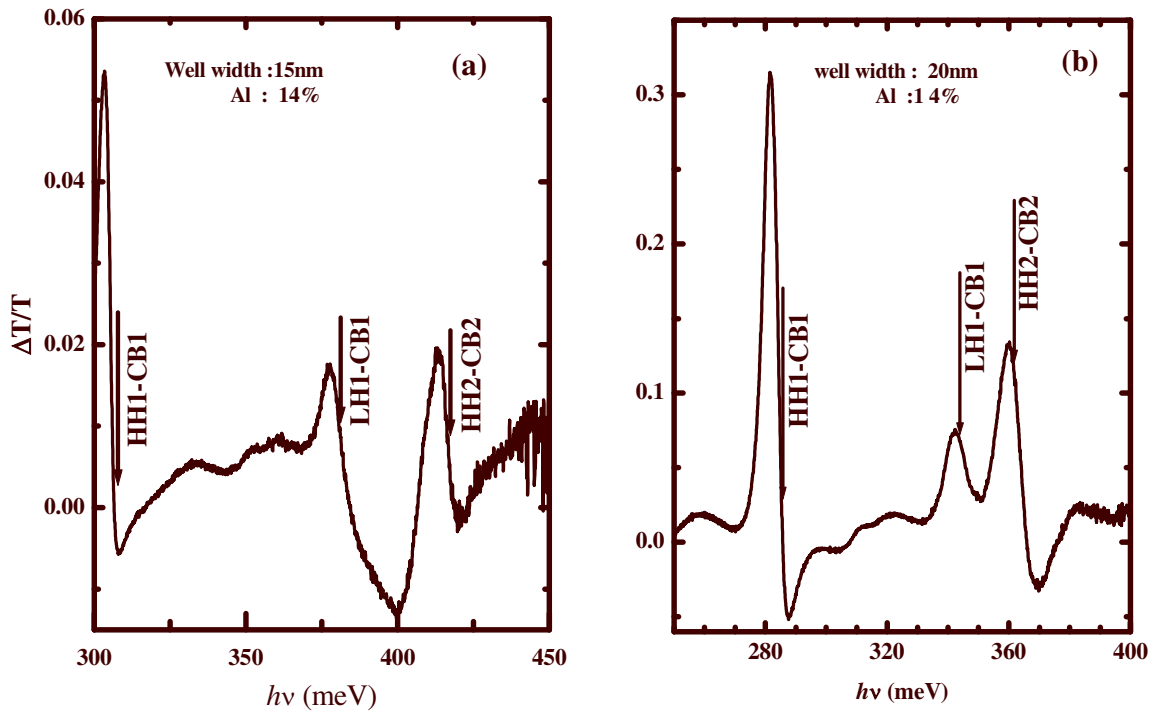


Figure 5.4: Differential transmission spectra (a): well width of 15nm and Al 14% in the barrier (b): well width of 20nm and Al 14% in the barrier.

5.4 Determination of Deformation potential parameters

(Method of Analysis)

The deformation potentials cannot be directly extracted from the excitonic spectra. First we need to know the heavy-hole and light-hole energy gaps. To determine these energy gaps for each sample, we use the observed heavy-hole ground state to the conduction-band ground state ($HH1-CB1$) and light-hole ground state to the conduction-band ground state ($LH1-CB1$) transition energies. These are listed in Table 5.2 for the 10nm, 15nm, and 20nm samples. The transition peak energy includes the contribution of confinement from both the valence and conduction bands. From these observed energies we then subtract the subband energies calculated for the conduction-band, heavy-hole, and light-hole quantum wells.

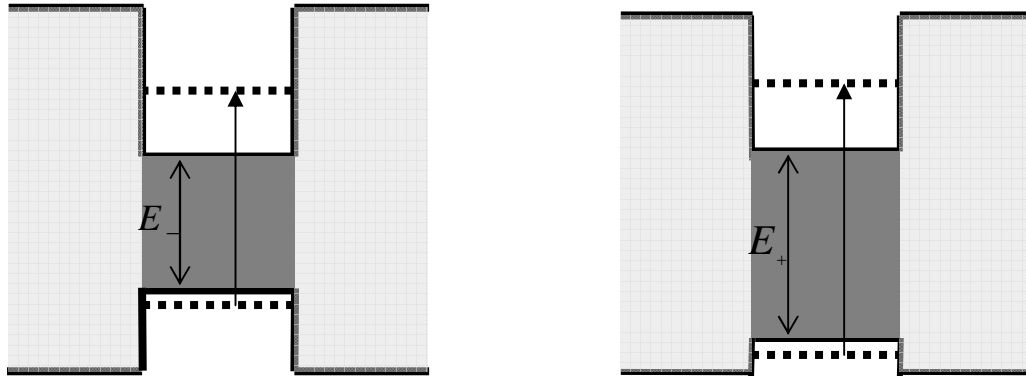


Figure 5.5: Schematic illustration of heavy hole and light hole gaps. E (Heavy-hole gap) = observed ($HH1-CB1$)-confinement subband energies. E_+ (Light-hole gap) = observed ($LH1-CB1$)-confinement subband energies.

Figure 5.6a displays an example of a typical differential transmission spectrum for a MQW structure. Solid arrows indicate observed transition features. Confinement energies, transitions and energy gaps are shown in Figure 5.6b.

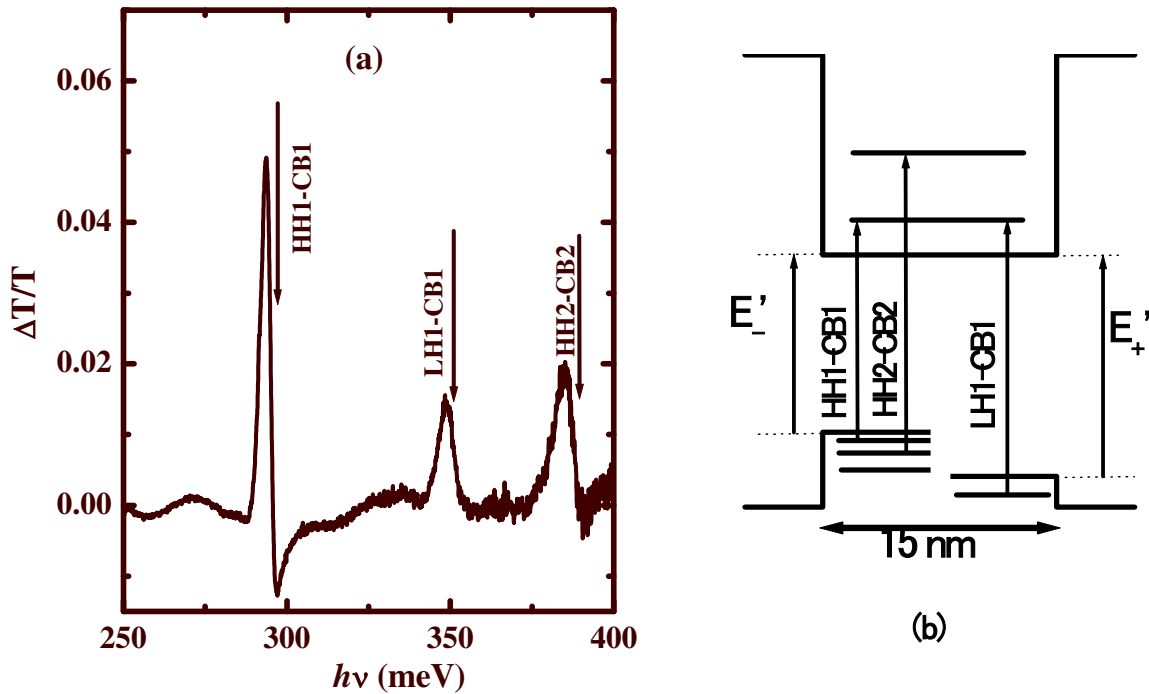


Figure 5.6: (a): Differential transmission spectrum of an InSb/ $\text{Al}_x\text{In}_{1-x}\text{Sb}$ MQW with Al concentration of 10% and well width of 15nm. (b): Energy-band configurations in a InSb/ $\text{Al}_x\text{In}_{1-x}\text{Sb}$ quantum well; The valence band is split into heavy- (HH) and light- (LH) hole bands as a result of the strain arising from the lattice mismatch between the two materials.

Well width	Al %	Theoretically predicted positions				Exp. observed positions	
		Heavy-hole gap (meV)	HH1-CB1 (meV)	Light-hole gap (meV)	LH1-CB1 (meV)	HH1-CB1 (meV)	LH1-CB1 (meV)
100 Å	8	247	303	283	346	305.4	349.4
	12	253	318	306	383	319	381.9
	16	259	330	328	415	332.4	414.6
	20	265	340	350	444	342.2	443.3
150 Å	7	246	279	277	322	286	326
	10	250	290	294	346	295	350.4
	14	256	297	317	374	306.4	382
	17	260	306	333	392	312.2	395
200 Å	5	243	266	265	294	263	290.6
	8	247	274	283	317	272	305.1
	11	252	280	300	337	280	318
	14	256	286	317	356	287	349

Table 5.2: Comparison of theoretically calculated transition energies with experimentally observed transition energies. Quantum well widths and nominal Al compositions are given in first and second columns respectively.

The band-offset ratio, which is a measure of the partition of the band gap difference in the conduction band, determines the quantum well depths in both the conduction and the valence bands. We use the conduction-band-offset ratio $Q_c = 0.62$ determined [37] from exciton spectroscopy in parabolic InSb quantum wells for the mismatch distribution. The band-offset ratio, Q_{cb} , is defined as the ratio of the depth of the conduction band square well, to the heavy-hole energy gap difference of the well and the barrier. Thus the well depths require the values of the heavy- and light-hole gaps.

To calculate the confinement energies for the ground state heavy holes, light holes and electrons we have used a four-band model described by Bastard [17]. In the calculation the nonparabolicity in the conduction band edge is taken into account. We used cyclotron effective mass $m_e = 0.0139$ for electrons (the band warping in the conduction band is negligible). The heavy and light-hole masses along the growth direction were obtained using Luttinger parameters.

$$m_{hh} = \frac{1}{(\gamma_1 - 2\gamma_2)} \quad m_{lh} = \frac{1}{(\gamma_1 + 2\gamma_2)}$$

From the Luttinger parameters (γ_1 and γ_2), m_{hh} is calculated to be close to 0.25 and m_{lh} to 0.015. Table 5.3 summarizes the calculated confinement energies for the 15nm samples. Figure 5.7 shows the theoretical predicted energies of the HH1-CB1 and LH1-CB1 transitions as a function of Al concentration. As mentioned earlier, the strain and nonparabolicity are included in the calculation and predicted energies are based on deformation potential values $a = -7.7$ eV and $b = -2.0$ eV [15].

Subband		Al Composition (x)			
		x = 0.07	x = 0.10	x = 0.14	x = 0.17
CB	N=1	29meV	33.2meV	36.7meV	40.5meV
	N=2	-	99.35meV	119meV	133.6meV
LH	N=1	15.4meV	18.2meV	20.5meV	22.9meV
HH	N=1	4.02meV	4.3meV	4.5meV	4.7meV
	N=2	17.05meV	17.8meV	18.4meV	19.6meV
	N=3	40.9meV	41.9meV	42.3meV	46.2meV
	N=4	-	-	79.0	85.9meV

Table 5.3: Calculated electron and hole (heavy and light) subband confinement energies for 15nm well width samples. N denotes the subband index. (Thus, theory predicts one CB subband, one LH subband and three HH subbands for sample with 7% Al).

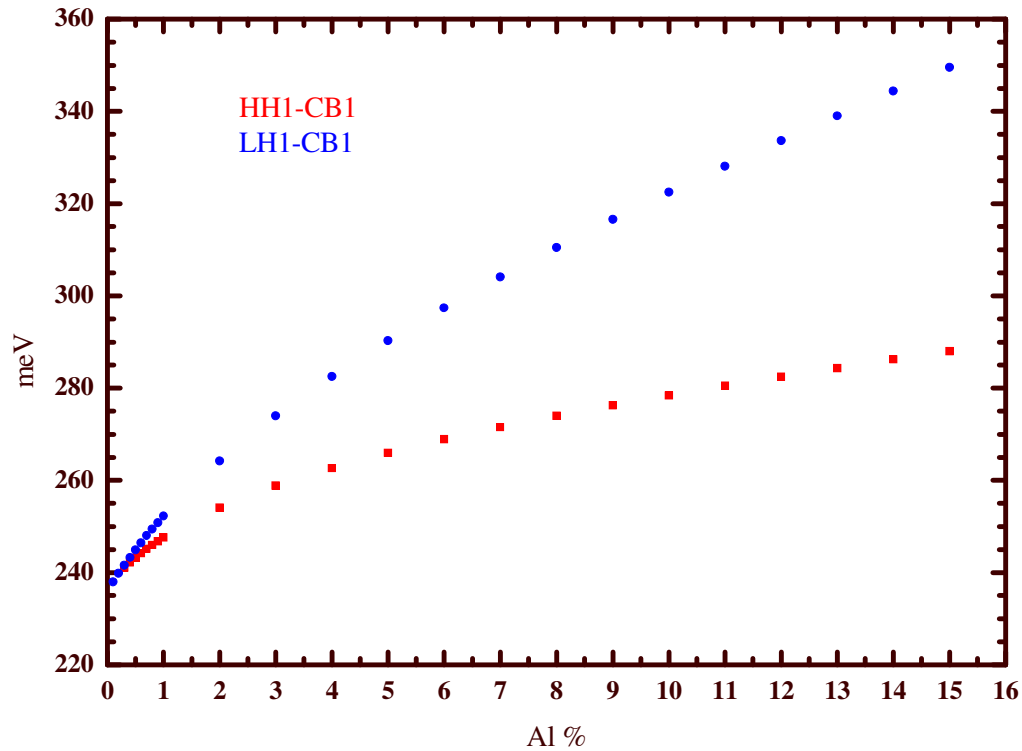


Figure 5.7: Theoretical predicted energies of the HH1-CB1 and LH1-CB1 transitions as a function of Al concentration for 20nm well width quantum well structures. Deformation potential values $a = -7.7$ eV and $b = -2.0$ eV are used in the calculation.

The process of determining the deformation potential parameters “a” and “b” is carried out in Fit.cpp, a C++ program written by Fred Brown [56]. When this program is run, the user requires various input parameters. The required initial values are observed transition energies, aluminum concentration, band gap for bulk InSb, number of monolayers of InSb making up the well and the initial values of “a” and

“b” from literature (Landolt-Bornstein values). These input parameters are read into the program from a file named “samples.in.” In determining E'_+ and E'_- , we initially use $a = -7.7$ eV and $b = -2.0$ eV and obtain approximate InSb band gaps under strain so as to determine the depths of the wells in both the valence and conduction bands. Then the program proceeds to solve for confinement energies for the heavy and light holes for each sample. By subtracting confinement energies from experimentally measured HH1-CB1 and LH1-CB1 transition energies more accurate new energy gaps are obtained. Using the new E'_+ and E'_- , we solve eq. (5.7) and (5.8) for the light holes and heavy holes to obtain new “a” and “b” simultaneously. The above procedure is iterated until convergence is achieved. Convergence is achieved rapidly because the subband energies are considerably smaller (of order 10%) than the gap energies. Since the ground state confinement energy is weakly dependent on the well depth, the new deformation potentials are very close to the values that would be obtained after several iterations.

Figure 5.8 presents the heavy- and light-hole energy gaps obtained using the iterative procedure described above with the experimental exciton transition energies as input data. The gaps are plotted against the in-plane strain $\epsilon_{//}$ determined from the mismatch between the InSb and the barrier in-plane lattice constants. (The figure also shows the corresponding barrier concentration values.) Three series of samples were used with well widths 10nm, 15nm, and 20nm. As we would expect, the gap values obtained are independent of the well widths. We found that this is not the case, however, when the well width is reduced to 5nm. As borne out by modeling, for such

thin wells (of the order of 10 monolayers) assuming a square well does not adequately reproduce the well's potential profile.

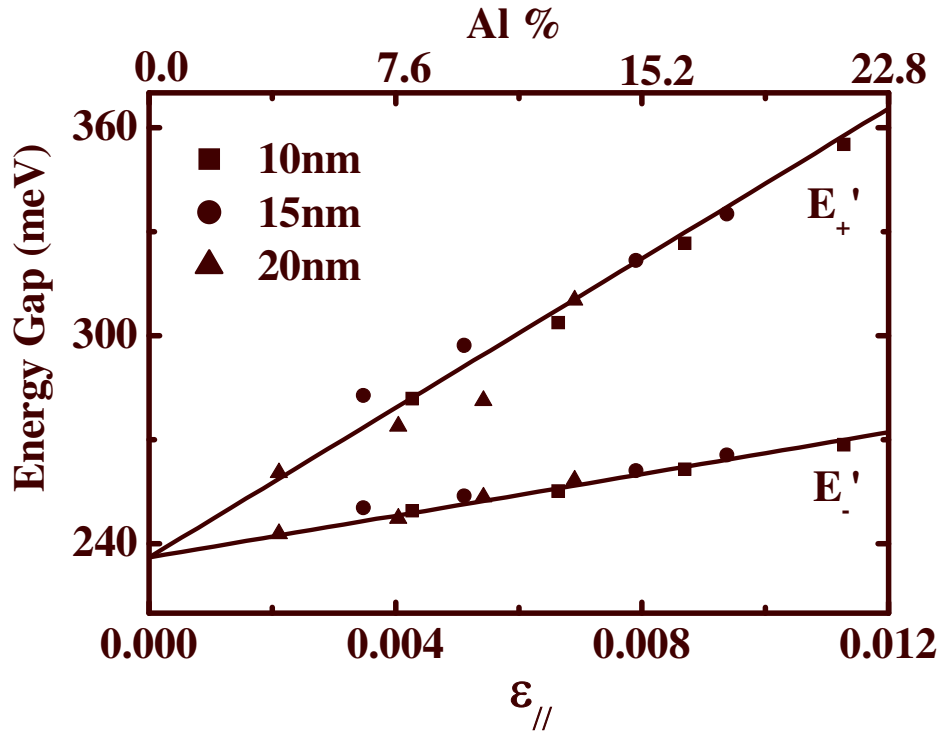


Figure 5.8: Light and heavy hole energy gap values obtained experimentally after the iteration procedure as a function of strain and barrier Al composition. Since subband energies have been subtracted, these deduced gaps reflect only the effects of strain.

Fitting the expressions from Eqs. (5.7) and (5.8) to the data of Figure 5.8 gives experimentally derived values for the deformation potentials “a” and “b.” We find a

= -7.4 ± 0.2 eV and $b = -1.8 \pm 0.1$ eV [57]. For a, recommended values range from -7.3 eV [11] to -7.7 eV [15] and for b the value -2.0 eV is recommended [11,15].

As discussed earlier we have obtained heavy hole and light hole band gaps for three series of samples with different well thicknesses. Next we obtained a and b values by fitting each set of data separately. Figure 5.9 presents the best fitting curves and a and b values for each series. By averaging, we find a (ave) = -7.44 eV and b (ave) = -1.83 eV. These results are in good agreement with the previously obtained values.

In summary, we have studied the effects of residual strain in InSb epitaxial films using the spectroscopic method. We found that residual strain induced by the mismatch of lattice constants has a strong influence in determining the energies of excitonic transitions. We have developed an alternate method to determine the deformation potential parameters by exploiting the effect of exciton transitions on the different strain dependence of the light and heavy hole edges.

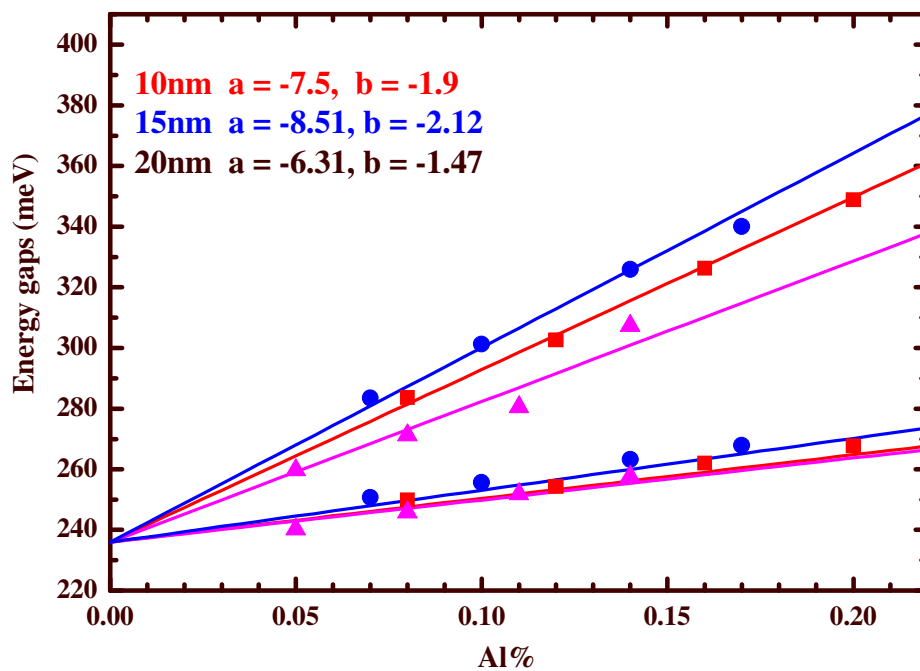


Figure 5.9: Light and heavy hole energy gap values as a function of barrier Al composition. Values of a and b are estimated from the best fit of the theory to the data. The solid lines in the figure represent the best-fit theoretical curves for well widths of 10nm, 15nm and 20nm.

Chapter 6

Excitons in magnetic fields: Magnetoexcitons

Excitons play an important role in optical properties of quantum well systems. An optical spectroscopy experiment in the presence of an external magnetic field is a good tool to explore these properties. In this chapter, I will focus attention on the excitons in the presence of an applied magnetic field for $\text{Al}_x\text{In}_{(1-x)}\text{Sb}/\text{InSb}$ quantum wells. I present results of the influence of a magnetic field on the excitonic spectrum, comparing theoretical and experimental results.

6.1 Introduction

As discussed in Chapter 2, the Coulomb interaction between electrons and holes in a semiconductor leads to the formation of excitons. Investigation of these excitonic states is of considerable interest; it can provide us with much information on excitonic properties. In particular, an external perturbation such as an applied magnetic field perpendicular to the quantum wells is a powerful tool which is expected to provide information on carrier subbands and exciton states. The importance of excitons was first clearly shown in the measurements of Edwards and Lazazzera on the direct edge of Ge [58]. Since then magneto-optical studies of excitons in quantum well structures have been carried out by many authors [59-65]. Rich spectral features due to the field dependent shift and splitting of the exciton absorption lines are seen in experiments. To understand the behavior of carriers in

quantum wells under magnetic fields, one needs to consider perturbations, such as confinement, magnetic fields, and Coulomb interactions between electron and hole.

6.2 Magnetic Field Limit: Are we in the high-field or low-field limit?

The relative importance of the magnetic field against the Coulomb energy is often represented by a dimensionless parameter γ which is defined as the ratio of the cyclotron quantization energy of the ground state to the Rydberg:

$$\gamma = \frac{\hbar \omega_c}{2R_y^*} = \frac{\hbar eB}{2R_y^* \mu}.$$

Here B is the magnetic field in Tesla, μ is the reduced effective mass, e is the charge of the electron, \hbar is the Planck's constant divided by 2π and R_y^* is the effective Rydberg, $R_y^* = \frac{\mu R_y}{m_e \epsilon^2}$, and ϵ is the dielectric constant.

In the weak field limit ($\gamma \ll 1$) the Coulomb energy dominates and the magnetic field can be treated as a perturbation. Hence, in the low magnetic field limit, the cyclotron energy of the electrons and holes is smaller than the binding energy of the corresponding exciton and the exciton shows a diamagnetic shift with increasing magnetic field. In the strong field limit $\gamma \gg 1$ and in this limit the cyclotron energy is large compared with the Coulomb energy and electrons and holes are under cyclotron motion. Equivalently, in the strong magnetic field limit, magnetic length \ll Bohr radius i.e. $l_B \ll a$.

where $l_B = \sqrt{\frac{\hbar}{eB}}$ and $a_B^* = \frac{\epsilon m_e a_B}{\mu} = \frac{4\pi\hbar^2 \epsilon}{\mu e^2}$. Perturbation from Coulomb interactions generates bound states belonging to Landau levels. Hence in the high field limit, excitonic states tend to show Landau-level-like behavior.

In Table 6.1 we list the typical values for the effective Rydberg and the effective Bohr radius for the Hydrogen atom, GaAs and InSb. As γ becomes unity at $\sim 0.13\text{T}$ in InSb, the available magnet (0 to 7.7T) allows us to investigate the magneto-optics in the strong magnetic-field regime.

	H atom	GaAs	InSb
ϵ	1.0	12.5	17.5
m_e^*/m_0	1.0	0.067	0.014
m_h^*/m_0		0.34	0.25
Ry* (meV)	$1.36 \cdot 10^4$	4.8	0.6
a_B^* (Å)	0.53	~ 120	~ 600
γ	$4.25 \cdot 10^{-6}$ B (T)	~ 0.2 B (T)	~ 7.43 B (T)

Table 6.1: Comparison between different characteristic parameters for the Hydrogen atom, GaAs and InSb.

6.3 Experiment

In the experiments, three InSb/AlInSb MQW samples were measured with different well widths and different alloy compositions. The compositions were from $x = 0.10$ to 0.17 and the well widths were 5nm and 15nm. The barrier widths were 50nm and they were thick enough to neglect the interference of confined-state wave functions between neighboring wells. The multiple well layer structure in the sample enhances absorption and reduces the intensity of the Fabry-Perot interference. In addition, measurements were performed on a parabolic quantum well structure. The sample structures for a 5nm MQW and a 50nm parabolic well are schematically shown in Figure 6.1 and 6.2.

The apparatus to perform the magneto-optical measurements is described in section (3.5). The backside of the samples was polished and wedged at 4° . Then the samples were mounted in the Faraday configuration at the center of a superconducting magnet in a liquid He dewar. The sample was illuminated by a globar source via an internally gold-plated light pipe arrangement connected to the exit port of a Bruker 66V/S Fourier transform spectrometer. The light transmitted through the samples was detected by an InSb detector. The transmission of each sample as a function of photon energy was measured at a constant magnetic field. These measurements were taken at two different temperatures (4.2K and 20K). Temperature was measured through connection to a Lakeshore Cryotronics, Inc. model 321-autotuning-temperature controller.

InSb cap layer	100Å
10% AlInSb layer	500Å
InSb well	50Å
10% AlInSb spacer	500Å
InSb well	50Å
10% AlInSb barrier	500Å
10% AlInSb layer	~2.0 μm
10% AlInSb/InSb SLS10*(25Å+25Å)	
10% AlInSb buffer-1μm	
GaSb layer	130Å
AlSb nucleation layer~5000Å	
GaSb buffer layer	1200Å
GaAs (001) substrate	

Figure 6.1: Layer structure of sample S656

InSb cap layer	100Å
25* 9% AlInSb /InSb parabolic wells 500Å-wells and 500Å alloy spacers	
One 9% AlInSb/InSb para.well	
9% AlInSb spacer	~2.0 μm
9% AlInSb/InSb SLS10*(25Å+25Å)	
9% AlInSb buffer	-1μm
GaSb layer	130Å
AlSb buffer	~0.85 μm
GaSb buffer layer	1100Å
GaAs (001) substrate	

Figure 6.2: Layer structure of sample S578

In the experiment, data was collected from 0 to 7.5 T at each 0.1 T increment. After finding that it was not efficient to take differential spectra for each and every 0.1T, another technique was used to see possible magneto-exciton effects more clearly. To achieve this, the absorption spectrum recorded at $B \neq 0$ was divided by the absorption spectrum recorded at $B = 0$. Nevertheless, as a check, differential spectra at every 1T measurement were obtained and compared to $B(T)/B(0)$ spectra at same field. It was found that they follow a similar pattern with the magnetic field. In the following section I present the experimental results obtained from the above methods.

6.4 Magnetoexciton Transitions

Figures 6.3a and 6.3b show the raw transmission spectra as well as differential ($\Delta T/T$) spectra at $B = 0.5T$ for the sample of 15nm well width with 10% Al in the barrier. As an important feature, differential spectra show more peaks and, therefore, weak features which are difficult to detect in the raw transmission spectra show up.

In our samples, at $B = 0$, several excitonic transitions between quantum well hole subbands (heavy hole and light hole) and electrons subbands are visible as minima. Figure 6.4 shows an example of the effect of applying a magnetic field perpendicular to the quantum well planes in the 15nm sample. When the magnetic field is applied, the exciton absorption peaks shift to higher energies. In addition, when B is increased, new features become clearly resolved in the spectra. For B exceeding 0.5T, the traces are dominated by a series of Landau level transitions

evolving from the HH1-CB1 exciton. These features will be explained in detail for each sample later in this chapter.

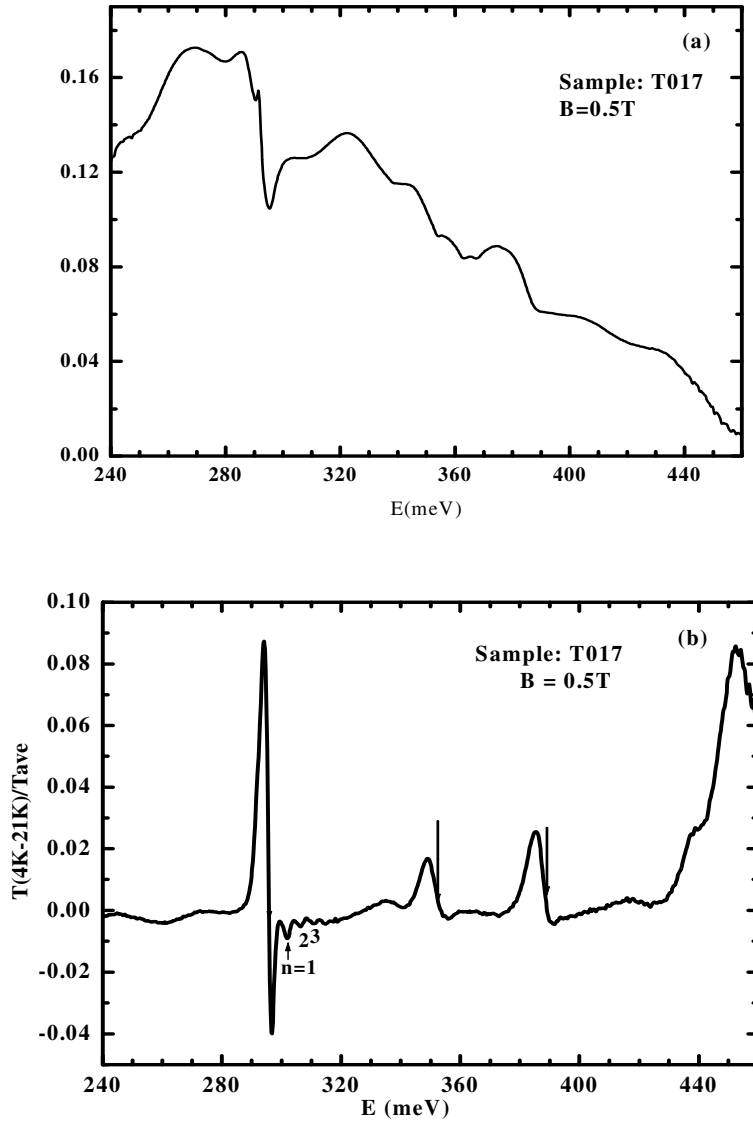


Figure 6.3: (a) Raw transmission spectra at $B = 0.5\text{T}$ (b) Temperature differential spectra at $B = 0.5\text{T}$. Note that the identified excitonic transitions are marked by arrows and the absorption peaks due to Landau levels are numbered by n in the figure.

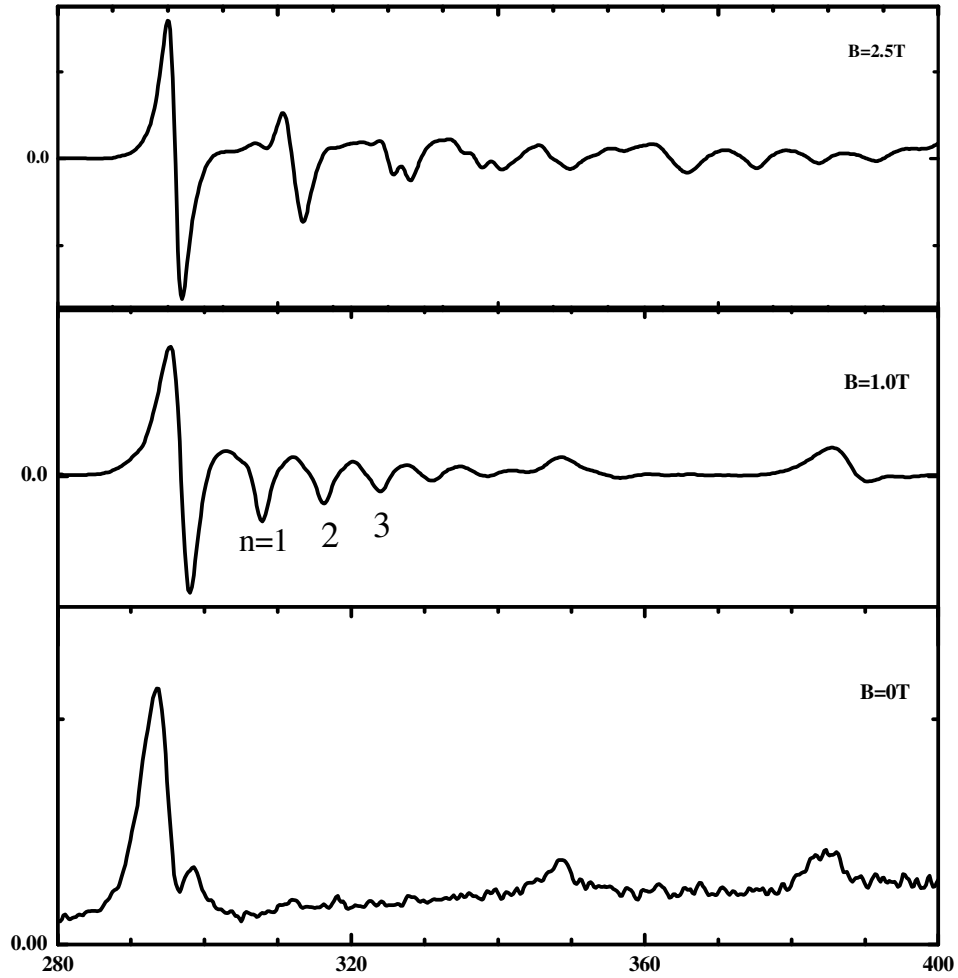


Figure 6.4: Magnetoabsorption spectra of InSb/Al_{0.10}In_{0.90}Sb MQW (same sample as Figure 6.3) at various magnetic fields. With increasing field, the exciton lines shift to higher energy. Note that Landau level associated peaks are indicated by numbering with n .

6.5 Theoretical Model

In order to interpret the observed interband magneto-optical transitions between the hole and the electron subbands we need calculations of the magnetic field dependence of these transitions. Quantum confinement, magnetic field, and electron-hole interaction (excitonic effects) affect the optical properties of quantum wells significantly. Therefore, it is important to include all of these mechanisms in the analysis of the spectra. In 1955, Luttinger and co-workers proposed a theory to calculate magnetic energy levels for Ge [19]. After that, Pidgeon and Brown (1966) modified the theory by calculating the Landau levels of the valence and conduction bands in an applied magnetic field [66]. In 1978, Weiler *et al.* further developed this method [67].

Our theoretical approach is based on the Pidgeon-Brown [68] effective mass model of narrow-gap semiconductors in a magnetic field which includes the conduction electrons, heavy holes, light holes, and split-off holes for a total of eight bands when spin is taken into account. As mentioned earlier, for the small bandgap materials the strong interaction between the conduction and valence band introduces non-parabolicity. The effect of nonparabolic conduction and light-hole bands and the anisotropy (warping) of the conduction and valence bands are included in the model. The interaction of higher bands with this system is included in the effective mass equation to order k^2 , and the resulting 8×8 equation is diagonalized for the eigenvalues and eigenvectors of the system. Following the Pidgeon and Brown model, the eight Bloch basis states are separated into an upper and a lower set.

The Bloch basis states for the upper set are:

$$\begin{aligned}
 |1\rangle &= \psi_{1/2,1/2}^6 = |S \uparrow\rangle \\
 |3\rangle &= \psi_{3/2,3/2}^8 = \frac{-i}{\sqrt{2}} |(X + iY) \uparrow\rangle \\
 |5\rangle &= \psi_{3/2,-1/2}^8 = \frac{i}{\sqrt{6}} [(X - iY) \uparrow + 2Z \downarrow] \\
 |7\rangle &= \psi_{1/2,-1/2}^7 = \frac{-i}{\sqrt{3}} [(X - iY) \uparrow - Z \downarrow].
 \end{aligned}$$

They correspond to electron spin up, heavy hole spin up, light hole spin down and split-off hole spin down respectively. The symbol \uparrow means spin up and \downarrow means spin down. S is the conduction-band function which transforms as an atomic s function. X, Y, Z are the valence-band functions which transform as atomic p functions under the operations of the tetrahedral group at the point Γ . S states are the major part of the conduction band, $|3/2, \pm 3/2\rangle$ and $|3/2, \pm 1/2\rangle$ states are HH and LH topmost valence band, and $|1/2, \pm 1/2\rangle$ states are the split-off band.

The Bloch basis states for the lower set are:

$$\begin{aligned}
 |2\rangle &= \psi_{1/2,-1/2}^6 = |S \downarrow\rangle \\
 |4\rangle &= \psi_{3/2,1/2}^8 = \frac{-i}{\sqrt{2}} |(X - iY) \downarrow\rangle \\
 |6\rangle &= \psi_{3/2,-3/2}^8 = \frac{-i}{\sqrt{6}} [(X + iY) \downarrow - 2Z \uparrow] \\
 |8\rangle &= \psi_{1/2,1/2}^7 = \frac{-i}{\sqrt{3}} [(X + iY) \uparrow + Z \downarrow].
 \end{aligned}$$

These correspond to electron spin down, heavy hole spin down, light hole spin up and split-off hole spin up respectively.

By assuming B is in the (110) plane, the effective-mass Hamiltonian H can be written as the sum of two parts

$$H = H(0) + H(1).$$

Here (H_1) is a small part arising from the anisotropy of the valence band and is treated by second-order perturbation theory. $H(0)$ is the large part and also part of the anisotropy is included in $H(0)$.

$$H(0) \approx \begin{bmatrix} H_a & 0 \\ 0 & H_b \end{bmatrix}.$$

$$H_a = E_a |a\rangle$$

$$H_b = E_b |b\rangle$$

Here E_a, E_b are the eigenvalues, and a and b are the effective mass wave functions which are linear combinations of the harmonic oscillator-type functions ϕ_n .

H_a and H_b are shown in numerical form in Appendix (B).

a and b can be expressed in matrix form

$$|a\rangle = \begin{bmatrix} a_1 \phi_n \\ a_3 \phi_{n-1} \\ a_5 \phi_{n+1} \\ a_7 \phi_{n+1} \end{bmatrix} \quad \text{and} \quad |b\rangle = \begin{bmatrix} b_2 \phi_n \\ b_6 \phi_{n-1} \\ b_4 \phi_{n+1} \\ b_8 \phi_{n-1} \end{bmatrix}$$

where a_1, a_2, \dots and b_1, b_2 .etc., are the eigenvectors.

It is clear that for $n \geq -1$, $a_1 = a_3 = b_2 = b_6 = b_8 = 0$ and for $n = 0$, $a_3 = b_6 = b_8 = 0$.

Then the complete wave function can be expressed as

$$\psi_a(n) = a_1 u_1 \varphi_n + a_3 u_3 \varphi_{n-1} + a_5 u_5 \varphi_{n+1} + a_7 u_7 \varphi_{n+1}$$

$$\psi_b(n) = a_2 u_2 \varphi_n + a_6 u_6 \varphi_{n-1} + a_4 u_4 \varphi_{n+1} + a_8 u_8 \varphi_{n-1}.$$

The parameters used in this model are the energy gap, E_g , the spin-orbit splitting, Δ , the interband coupling energy, E_p , the valence band effective mass and g-factor parameters, $\gamma_1, \gamma_2, \gamma_3, \kappa$ and q , and the conduction band effective mass and g-factor parameters, F and $N1$ [67,68]. To apply the Pidgeon-Brown model to a quantum well system, the bulk energy gap is replaced by an effective gap which is the energy separation between the lowest conduction and highest valence subbands. E_g, Δ, E_p have the units of energy and $\kappa, q, N1, F$ and γ 's are dimensionless.

6.6 Selection Rules

To calculate the interband transition energies from the Landau levels, one must need the selection rules for transitions between the valence and conduction bands. According to Weiler et al [68], the selection rules for interband transitions are:

$$\sigma_L : a_n \rightarrow a_{n+1}, b_n \rightarrow b_{n+1}$$

$$\sigma_R : a_n \rightarrow a_{n-1}, b_n \rightarrow b_{n-1}$$

$$\pi : a_n \rightarrow b_{n+1}, b_n \rightarrow a_{n-1}$$

Here σ_L and σ_R are left and right circular polarization respectively. π refers to the E //B polarization. Weiler et al. have obtained these selection rules before renumbering the valence bands. In their study, they were concerned with conduction band states

only. Hence such renumbering is not necessary. In the Pidgeon and Brown approach, the valence band states are renumbered as $n \rightarrow n+1$. The selection rules for interband transitions are given by $\Delta n = 0, -2$. In our experiment, the light incident on the sample was unpolarized. Hence, incident light contains both components (σ_L and σ_R) and we expect σ_L and σ_R transitions. In the experiment the applied magnetic field, B (T) was not tilted and therefore there is no π polarization component resulting in the absence of any spin flip transitions.

The Pidgeon and Brown model does not take into account any excitonic effects. For the purpose of understanding the magneto-optical spectra properly, however, it is essential to take the excitonic effects into account. To overcome this drawback, Weiler et al. [69] included the exciton correction term in an approximate way.

$$\Delta E(n, B) \approx 1.6R \left[\frac{\gamma}{(2n+1)} \right]^{1/3}$$

Here γ is the reduced magnetic field, n is the Landau quantum number of the

conduction band final state and R is the reduced effective Rydberg. ($\gamma = \frac{1}{2} \frac{\hbar \varpi_c}{R}$,

$$\hbar \varpi_c = \frac{\hbar e B}{\mu} = \frac{2m_e \mu_B}{\mu} \quad \text{and} \quad R = \left(\frac{R_0}{\varepsilon^2} \right) \frac{\mu}{m} .$$

where m , μ_B , and R_0 are, respectively, the free-electron mass, the Bohr magneton, and the Rydberg constant. μ is the reduced electron-hole mass and ε is the dielectric constant).

6.7 Theoretical Results

The calculated Landau levels for the first conduction subband are shown in Figure 6.5.

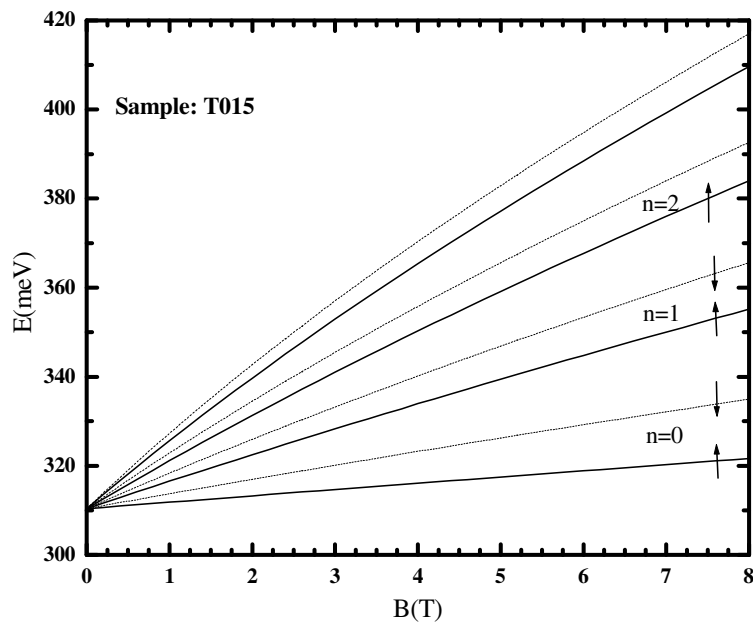


Figure 6.5: Theoretical predictions for the Landau levels in the conduction band of the sample with well width 15nm and 17% Al in the barrier. Solid lines and dashed lines denote spin up and spin down states respectively.

For III-V systems, it is well known that the valence-band structure is relatively complex and very different from the conduction band structure. Figure 6.6 shows the fan chart of Landau levels evolving from the top most HH subband. When the

magnetic field increases, the spin-split states change their order. For an example, for fields greater than about 8T, spin up $n = 2$ Landau level has higher energy than the spin down $n = 2$ level. The nonlinear dependence of the Landau levels on the magnetic field is due to the nonparabolicity of the system.

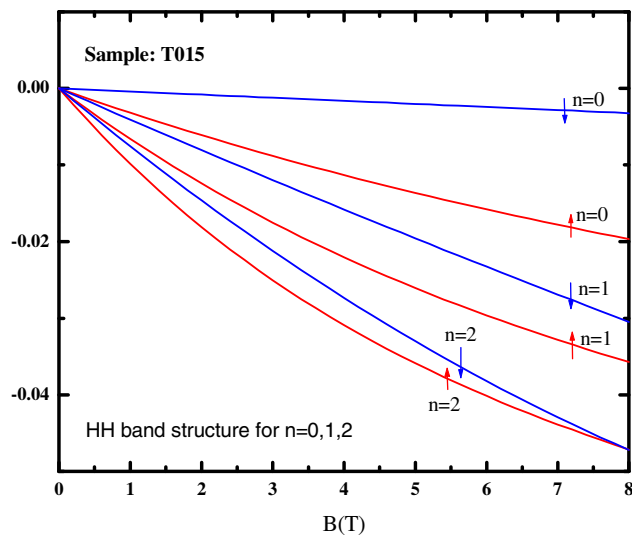


Figure 6.6: Calculated Landau-level structure for heavy holes in the valence band of an InSb/AlInSb QW structure with 15nm wells. Note that hole states are labeled as n , and n is the Landau quantum number.

6.8 Comparison between Theory and Experiment

6.8.1 Sample (1): S656

Sample S656 has a 5nm well with 10% Al in the barrier and 25 periods. Theory predicts one heavy hole, one light hole and one conduction band bound state for this sample. Predicted subband energies for CB1, HH1, and LH1 are 83, 24.5, and 23.7 meV respectively. Calculated barrier heights for CB, HH and LH are 115, 70.5 and 26.5 meV respectively. These details are schematically depicted in Figure 6.7. The separation between HH1-CB1 and LH1-CB1 is around 43meV. Since heavy-hole and light-hole transitions are well separated, the effect of the mixing on these two states is minimal.

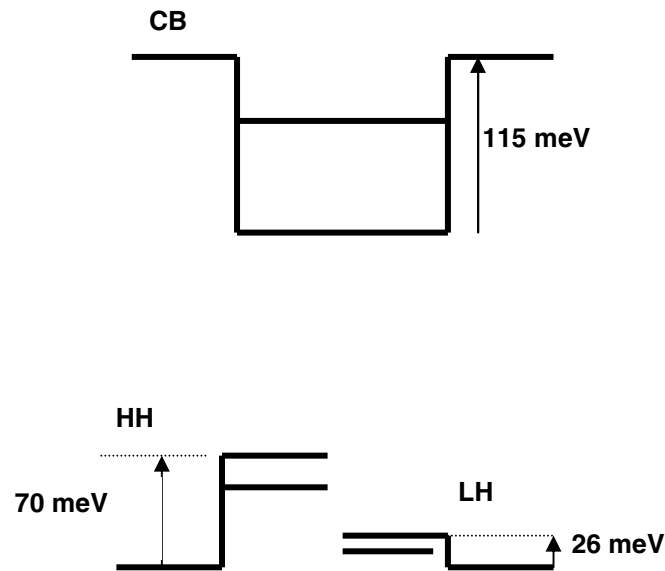


Figure 6.7: Schematic potential profiles for electrons, heavy holes and light holes in a 5nm well.

We now relate the experimental data from sample S656 to a fan chart diagram for transitions between Landau levels of the conduction and valence bands. In Figure. 6.8, we have plotted the energy of the absorption peaks as a function of the magnetic field. The calculated transitions between Landau levels with $n_e = n_h$ are shown in the figure by solid lines. Here $n_{e(h)} = 0,1,2,\dots$, is the Landau-level number for the conduction (valence) band. When extrapolated to lower fields, these lines almost converge to the same zero field energy. This convergence point energy agrees with the energy of the HH1-CB1 state at zero field.

As shown in Figure 6.8 experimental transition lines have varying magnetic field dependence. The heavy-hole ground state shows relatively weak magnetic field dependence and no spin splitting for the $n = 0$ state in the studied magnetic field range. At 3.8T the $n = 1$ state starts to split. As the magnetic field increases, the intensity of the low energy peak decreases, while the higher energy peak intensity increases. This behavior can be clearly seen at ~ 410 meV and ~ 430 meV (see Figure 6.10). The origins of these features are unclear at this point and cannot be explained with the current theoretical model. This observation led us to think about possible anticrossing behavior.

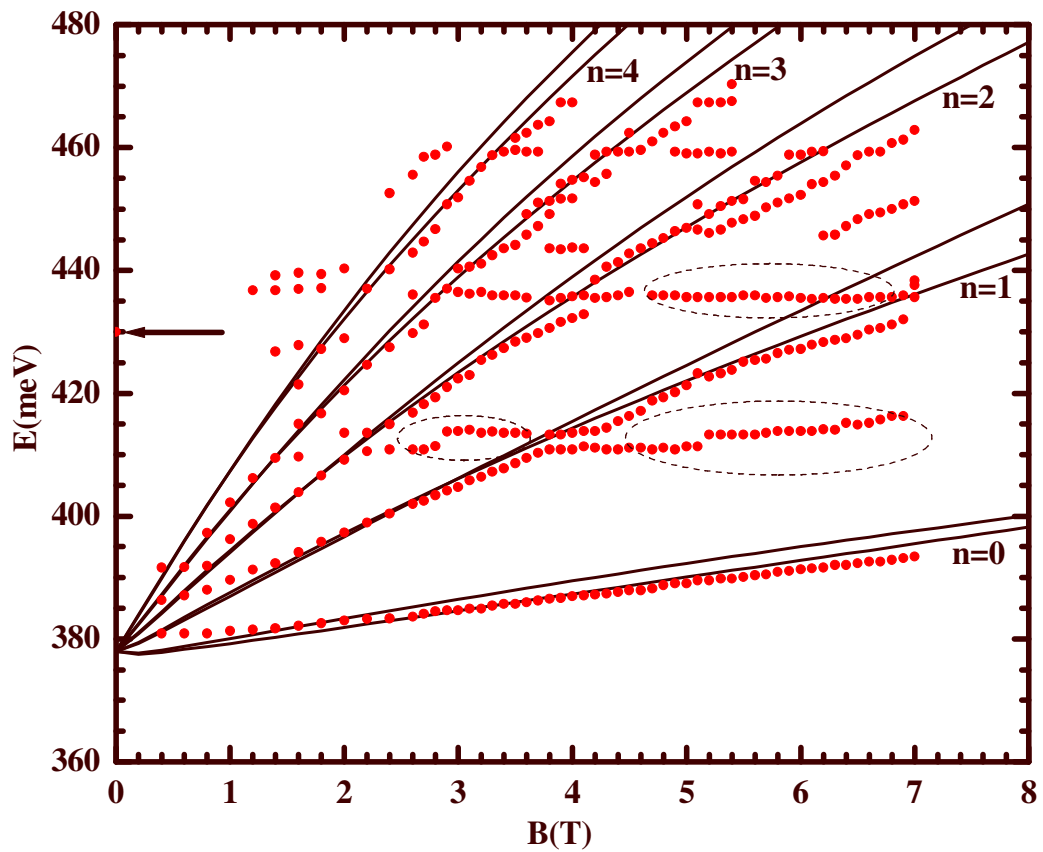


Figure 6.8: Experimental transition energies(points) for sample S656 (5nm well width) plotted against the magnetic field. LH1-CB1 excitonic transition at zero magnetic field is marked by an arrow. Note that solid lines are from the theoretical model and transitions up to $n = 4$ are clearly observed.

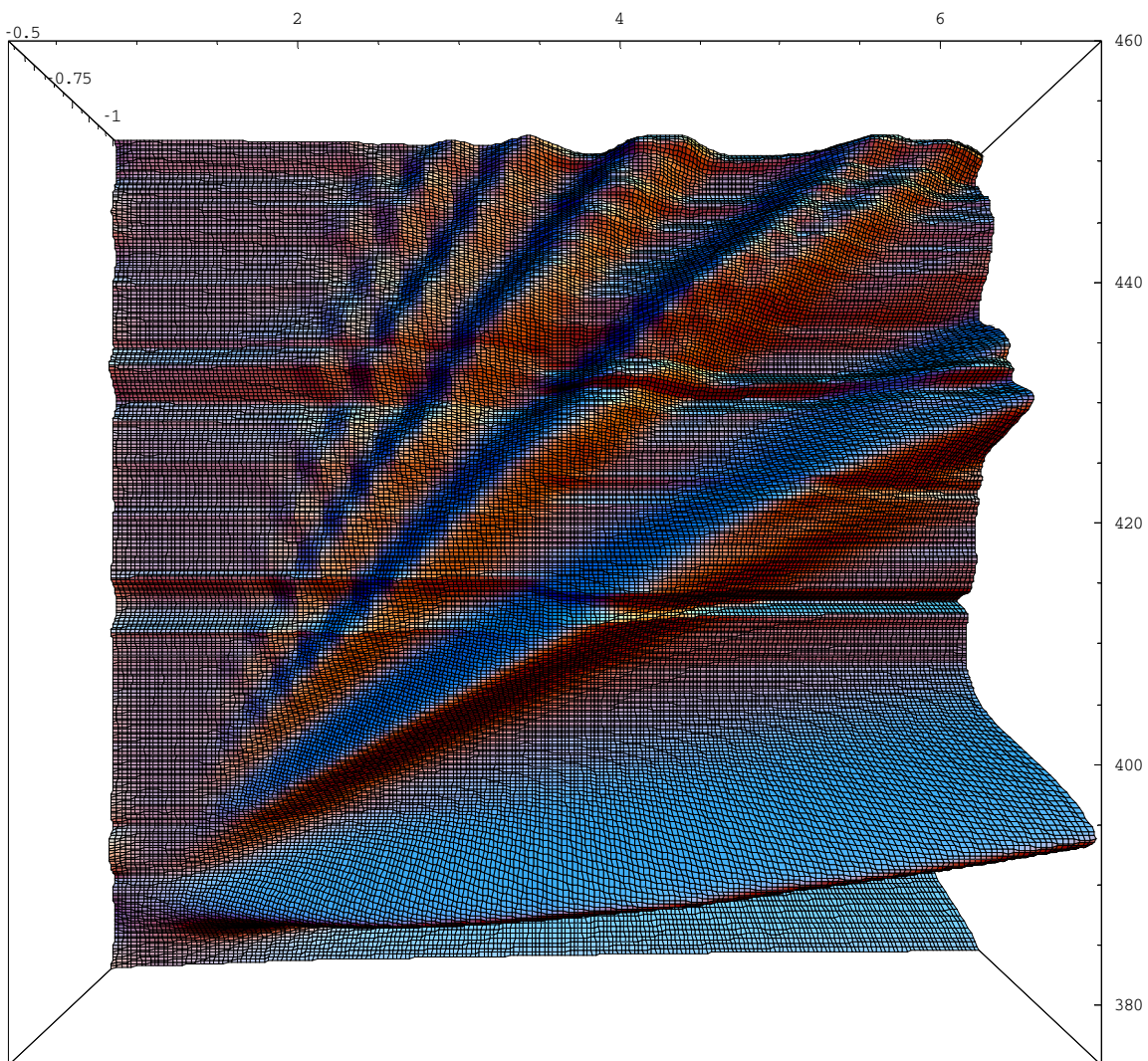


Figure 6.9: Experimental magneto-absorption spectra of sample S656 for various magnetic fields.

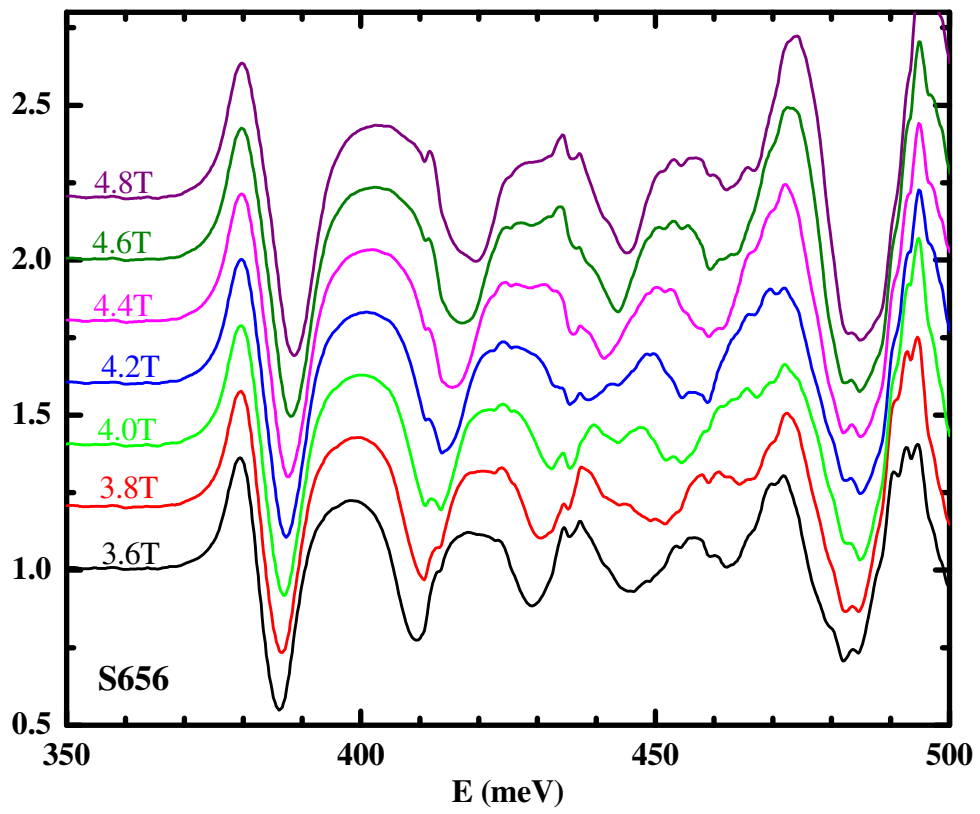


Figure 6.10: A series of transmission traces as a function of magnetic field. The traces are displaced upward for clarity.

An anticrossing behavior between excited states of the heavy-hole exciton and the ground state of the light-hole exciton has been observed in GaAs /GaAlAs system [63, 70]. Recently, anticrossings involving bright and dark excitons in InGaAs/GaAs quantum wells have been observed [71]. Authors of this report claim that the Coulomb interaction plays an important role in understanding the anticrossing behavior. However, the origins of anticrossing interactions in high magnetic fields are not completely understood. In addition to the Coulomb interaction, in-plane strain could be responsible for the origin of anticrossing features. Figure 6.11 displays the magnetoexciton spectral line positions for $\text{In}_{0.2}\text{Ga}_{0.8}\text{As}/\text{GaAs}$ MQWs at 4.2K for various fields up to 30T. In the figure, H_n^N (L_n^N) represents the optically active (bright) HH (LH) exciton states and D_n^N denotes the optically inactive (dark) exciton states. Here N is electron and hole Landau quantum number and $N = 0, 1, 2, \dots$. And n is the electron and HH (LH) QW energy level. Anticrossing behavior between the H_1^1 - D_3^0 and H_1^2 - D_3^1 lines are clearly seen.

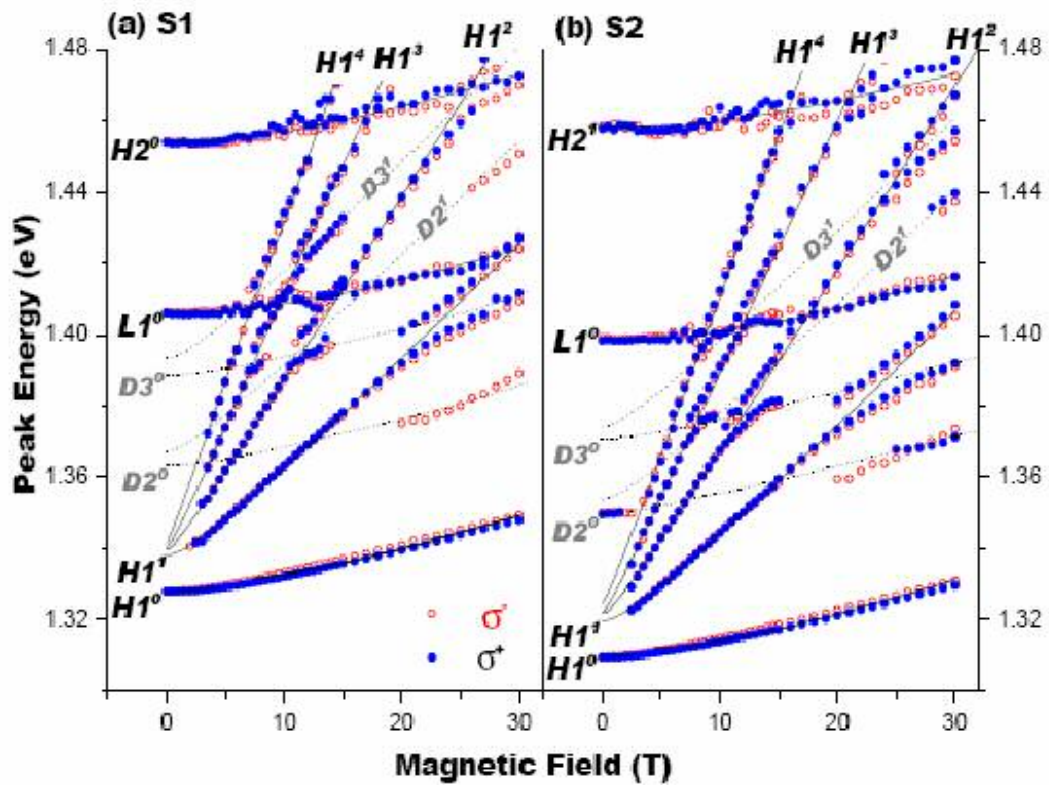


Figure 6.11: Magnetoexciton spectral line positions in samples S1 and S2 [71].

6.8.2 Sample (2): T017

The next sample studied was a 15nm MQW with 10% Al in the barrier and 40 periods. When the quantum well width increases the number of confined subbands increases. T017 has two conduction band bound states, three heavy-hole states and one light-hole state. Figure 6.12 shows magnetic field dependence from 0T to 2.5T. In the absence of external magnetic fields, the spectrum contains three well-defined peaks at 295, 350 and 388 meV. They are identified as HH1-CB1, LH1-CB1, HH2-CB2 transitions. The energy splitting between HH1-CB1 and LH1-CB1 is ~ 55 meV.

At 0.5 T, Landau level transitions are seen to evolve from HH1-CB1 edge. These features become stronger with increasing magnetic field. Landau level transitions evolving from the LH1-CB1 transitions first become visible at about 1.5T. Nevertheless, these transitions are rapidly dominated by the heavy-hole transitions. As shown in Figure 6.12-e, at 2.0T, the LH1-CB1 exciton resonance merged into the HH1-CB1 exciton resonance. Note that after 2.0T, LH1-CB1 transitions diminish as the magnetic field increases.

It has been established that the exciton oscillator strength enhances with increasing magnetic field [72]. However, enhancements of the oscillator strength of heavy-hole and light-hole excitons are different. The light-hole exciton has rather small oscillator strength. Therefore, the transitions associated with Landau levels that evolve from HH1-CB1 are stronger than those that evolve from light hole states.

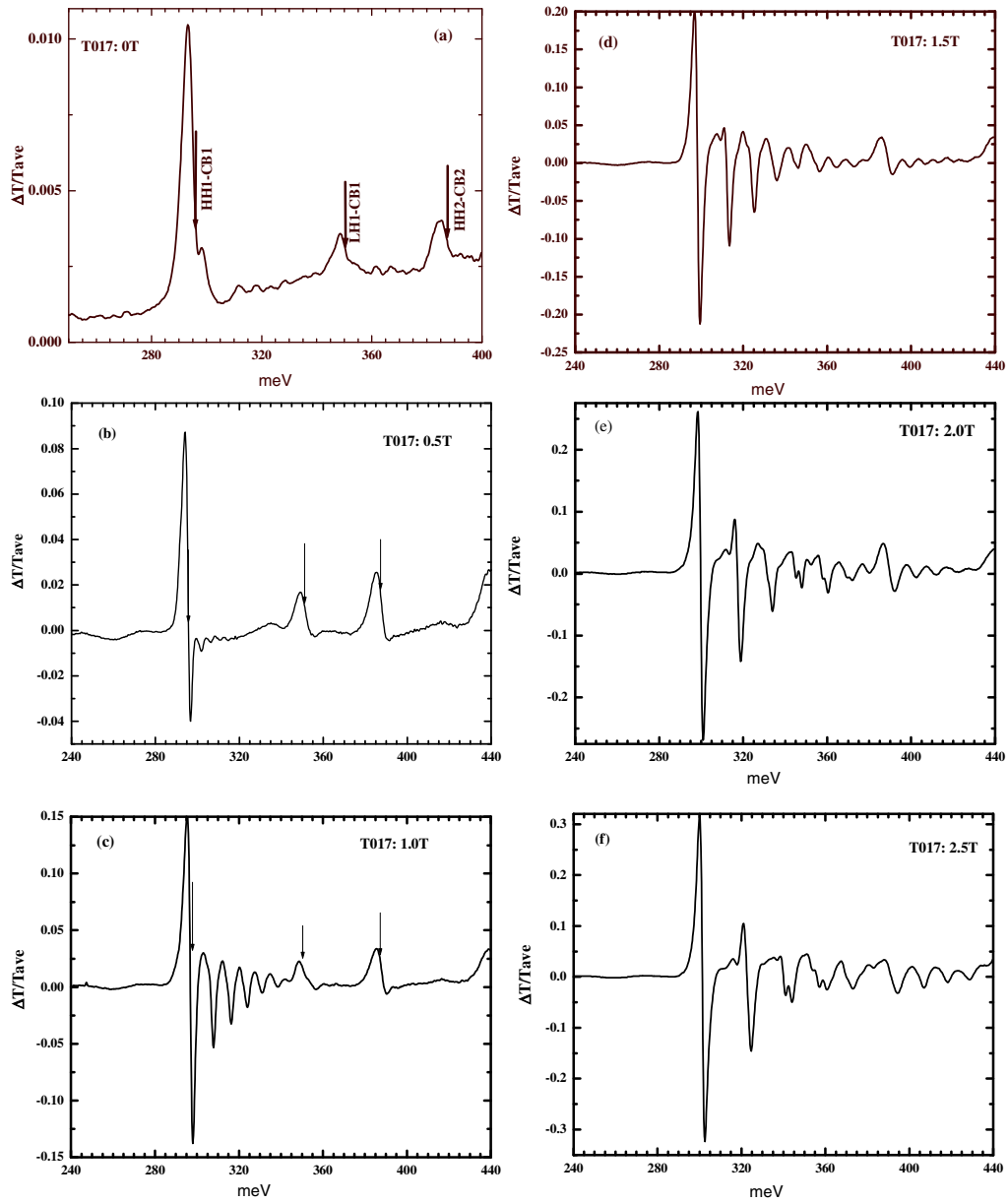


Figure 6.12: The evolution of the exciton states under applied magnetic field.

Figure 6.13 shows the influence of the magnetic field on the absorption spectra of the sample T017. The spectra contain strong and weak peaks; they are unevenly spaced and have different intensities. This complicated structure reflects the complexity of the valence band.

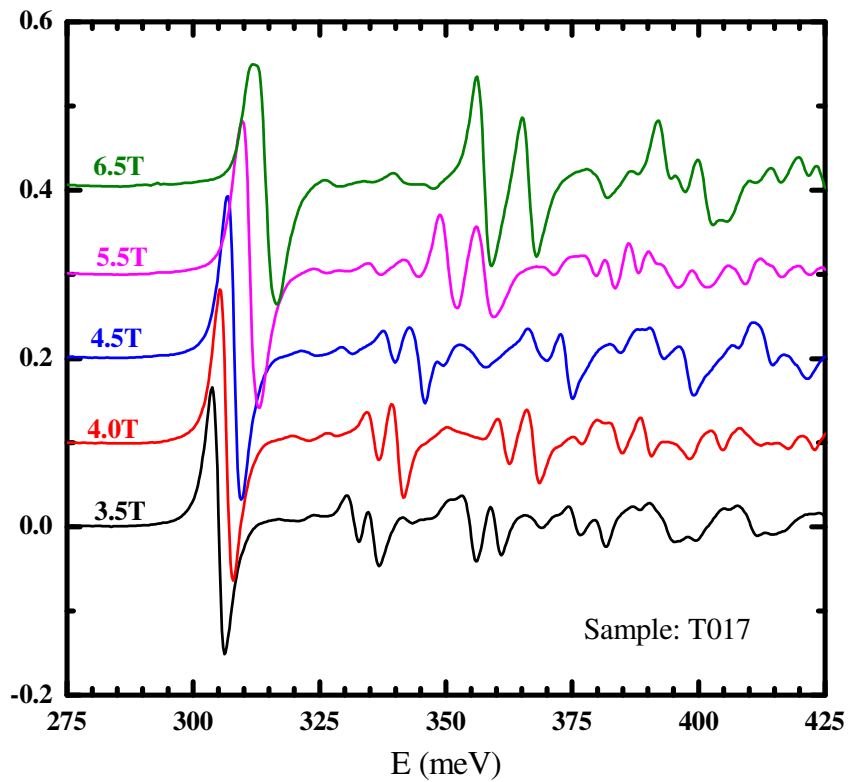


Figure 6.13: Observed spectra from a MQW sample of 15nm well width and 10% Al in the barrier for magnetic fields from 3.5T to 6.5T at 4.2K.

As shown in the fan diagram in Figure 6.14, the traces are dominated by a series of Landau level transitions evolving from the HH1-CB1 exciton. For sample T017, the Landau-transitions seen in the data persist down to low magnetic fields ($\sim 0.5\text{T}$) and transitions up to $n = 7$ are clearly observed. After 2.6T , additional weak lines appear between the main features. These transitions have not been identified. At $B = 4.8\text{T}$ spin-induced splitting of the exciton resonance from Landau level $n = 1$ is observed. The splitting energy increases with increasing magnetic field. For higher Landau levels, spin splitting is resolved at lower fields. For instance, the $n = 2$ Landau level spin-splitting is resolved at 2.6T and $n = 3$ at around 2T . The spin splitting could not be resolved for the $n = 0$ state in the range of fields studied. Furthermore, from the fan chart we note that spin-split states are predicted to change their order with increasing magnetic field. For example, for $n = 1$ state spin energies show general behavior below 2.5T . After 2.5T for $n=1$, the spin up state has higher energy than the spin down state. For $n = 2$ and 3 , spin-split states change their order at 1.5T and at 1T respectively.

It is clear from Figures 6.14 and 6.15 that the magneto-absorption spectra for sample T017 is more complicated than that of sample S656 and therefore, a question arises of how to explain the features. The interpretation of the magneto-absorption line spectra is complicated because of the complex valence band structure. Compared to the 5nm well, in T017 (15nm) the eigen states of heavy-hole and light-hole are closer in energy. This can enhance the mixing of heavy and light-hole states. So we

tentatively attribute the additional transitions to mixing of the heavy and light-hole states.

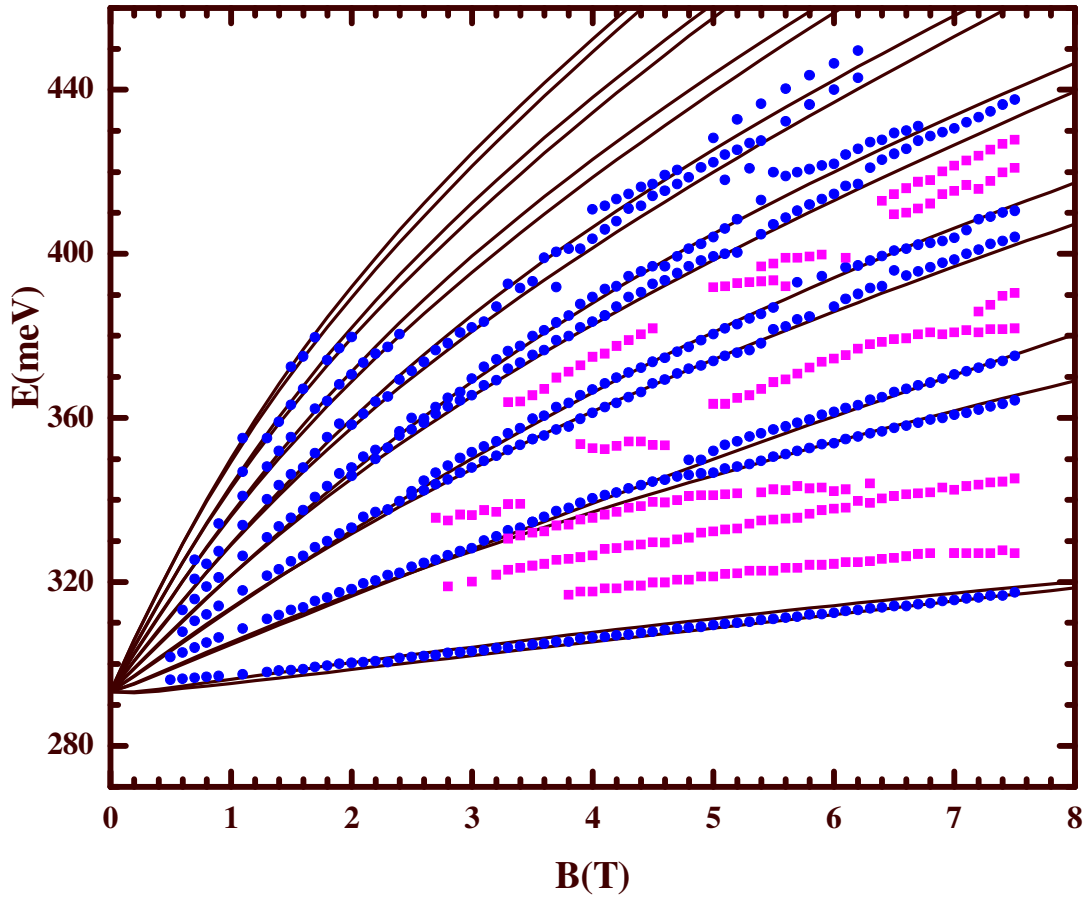


Figure 6.14: Comparison between the calculated (solid lines) and the experimental transition energies. Points and squares represent the observed strong and weak features respectively. The nonparabolic effects of the conduction and valence bands are shown by the curvature of the lines.

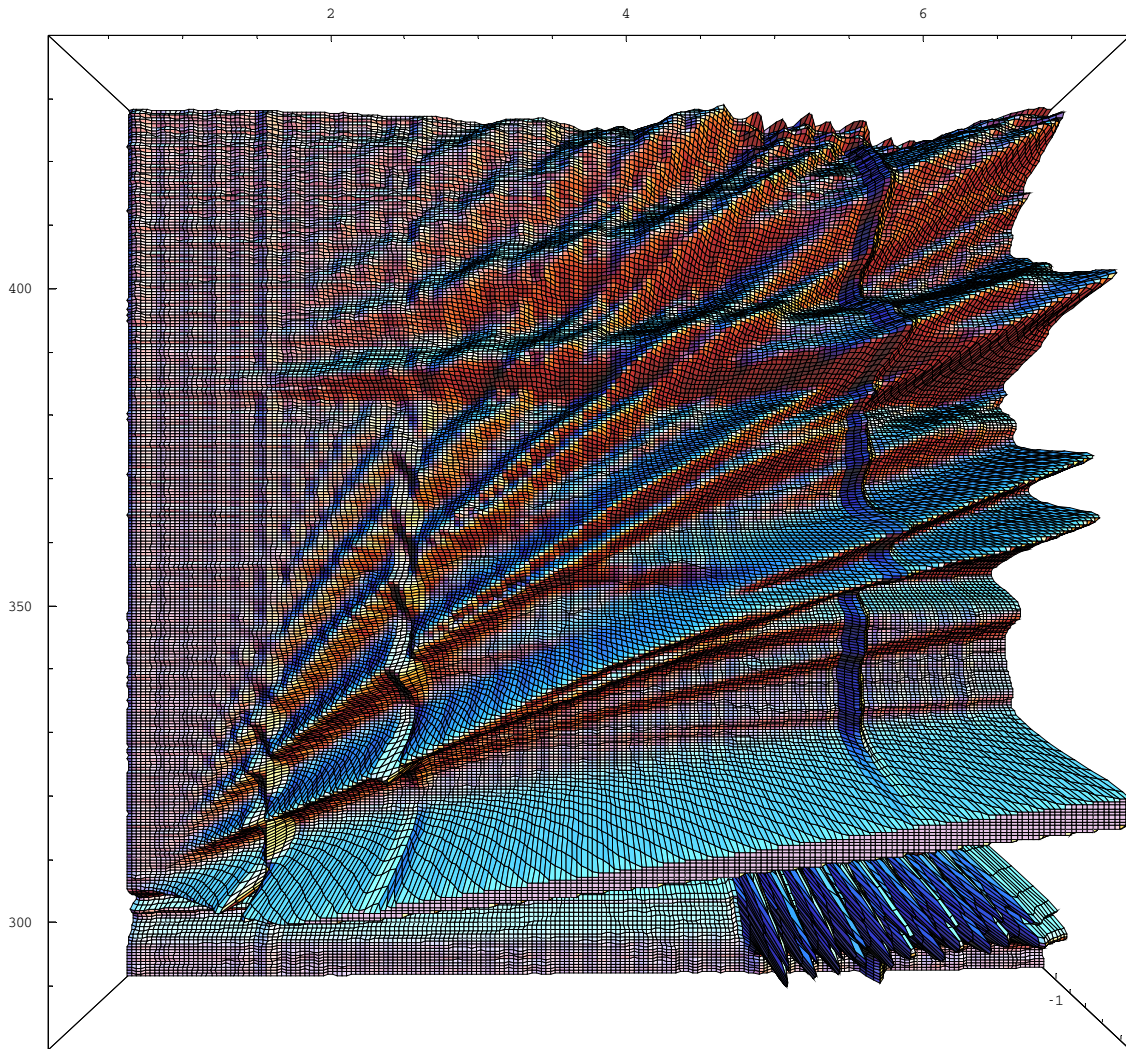


Figure 6.15: Experimental magneto-absorption spectra of sample T017 for various magnetic fields.

6.8.3 Sample T015

Sample T015 has 15nm wells with 17% Al in the barrier and 40 periods. The only difference between T017 and T015 is the Al composition in the barrier. By increasing the Al concentration in the barrier, the separation between heavy and light-hole subbands is increased. T015 has two conduction band bound states, three heavy hole states and one light hole state. The predicted energy separation between HH1-CB1 and LH1-CB1 is $\sim 87\text{meV}$. Compared to S656 and T017, data taken for T015 sample was noisy. In addition, the line shape of the excitonic transition is broader. Therefore, it was difficult to resolve weak features that were observed in sample T017. We were also not able to observe any transitions from the light hole band. However, one can resolve transitions from HH1-CB1 and HH2-CB2. Figure 6.16 shows the energy of the identified peaks as a function of the magnetic field. The higher energy lines extrapolate to the energy of the HH2-CB2 state at zero field. The Pidgeon and Brown model was used to compare the data for HH1-CB1 transitions. Figure 6.17 depicts the fan diagram for T015. The fan diagrams for sample T015 and T017 are similar, except that the effective band gap for T015 is about 15meV higher, which is due to the difference in aluminum concentration. However, the main features for T015 follow similar behavior as T017 although the over-all fan diagram is not complicated because the weak features are not resolved.

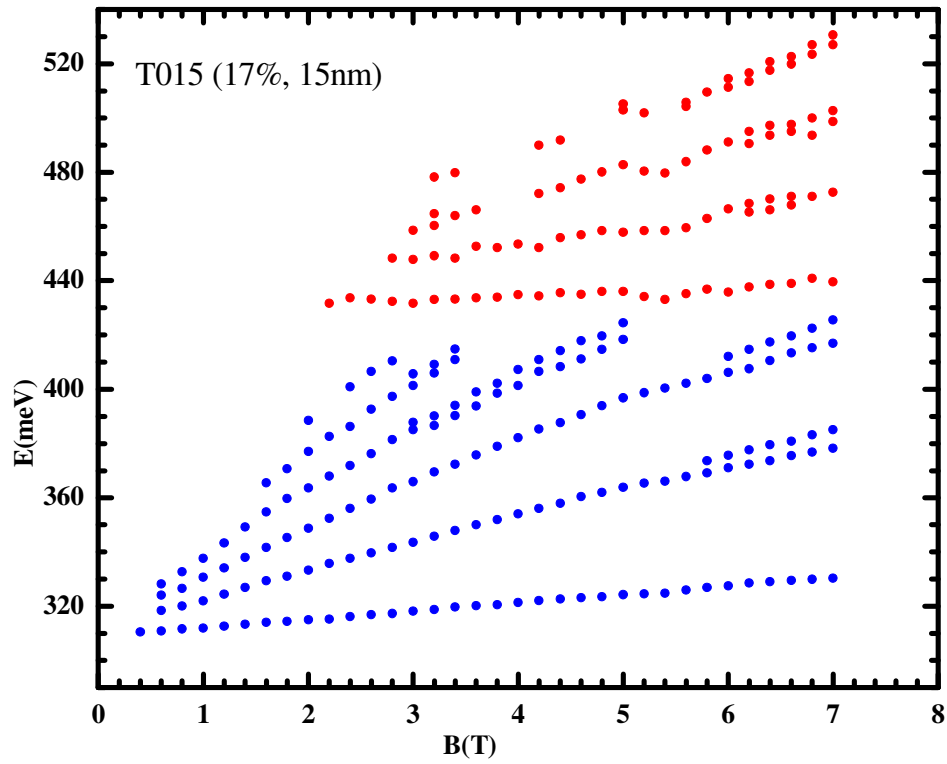


Figure 6.16: The experimental peak positions as a function of magnetic field for the sample with well width 15nm and 17% Al in the barrier.

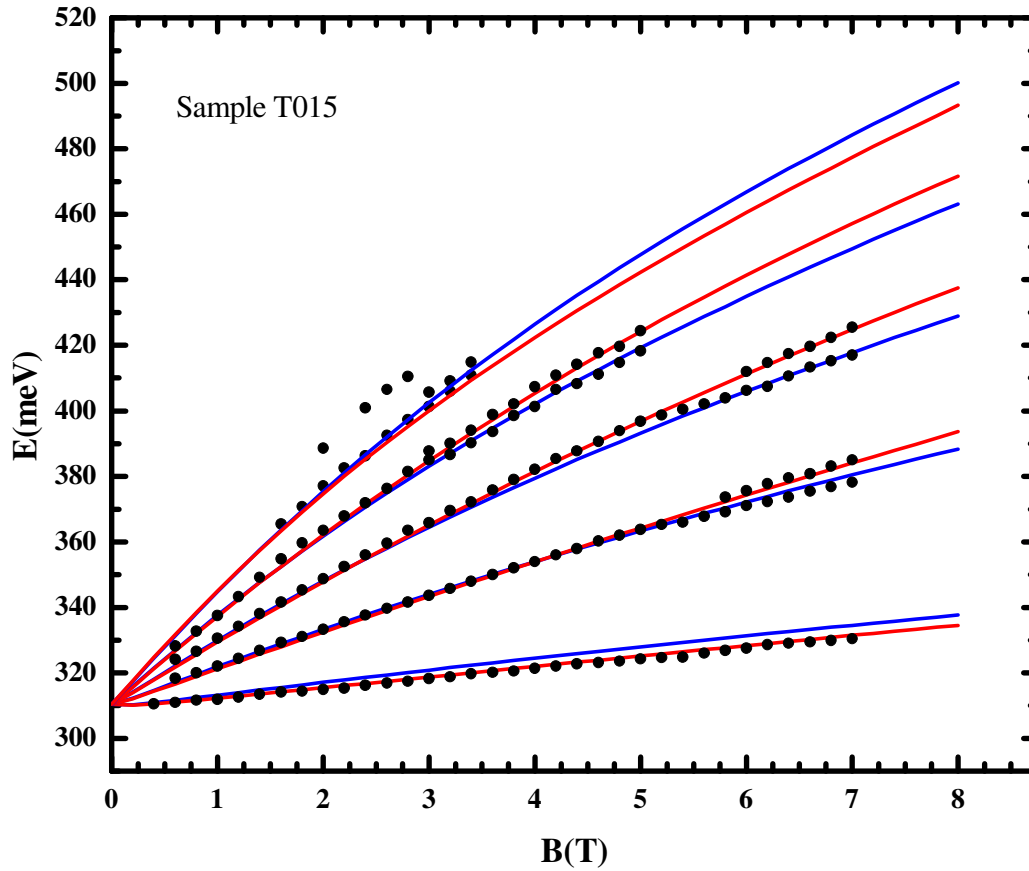


Figure 6.17: Comparison between the calculated (solid lines) and the experimental transition energies. Solid lines represent the theoretically generated results.

However, comparing the energies of the calculated transitions with the experimental observations, we find a fairly good agreement between current theory and experiment except for the above mentioned unidentified features. A more

rigorous exciton model is required for a quantitative description of the unidentified exciton states in the spectra.

6.9 Parabolic Quantum Wells

In recent years, the progress in molecular beam epitaxial growth techniques has offered the possibility to obtain low-dimensional semiconductor structures with various well shapes. In particular, using the digital growth method as described in [73], one can fabricate quantum well structures with a confining potential which accurately approximates a parabolic shape. Since the first fabrication of parabolic quantum wells (PQW), there has been a continued interest in these structures. Parabolic quantum wells were first successfully studied in optical experiments by Miller, Gossard, Kleinman, and Munteanu [73]. The PQW structure could be of importance in applications due to its unique electronic features, the fact that the ground state is more confined than the excited states, and because of its distinctive potential profile. Most interesting is the fact that in such systems forbidden transitions can be observed.

The parabolic potential is of the form $V(z) = \frac{1}{2}kz^2$. Here k is the spring constant and z is the spatial coordinate in the growth direction. In the limit of an infinite well, an electron behaves like a simple harmonic oscillator and has equally spaced energy levels $E_n = (n - \frac{1}{2})\hbar\varpi$, $n = 1, 2$ etc., and $\varpi = \sqrt{\frac{k}{m^*}}$. Figure 6.18 shows

a schematic of a parabolic well with finite barriers. If E_n is not too close to the top of the barrier, the simple harmonic oscillator is still a good approximation. Then the potential at the interface is $V = Q_{cb}\Delta E_g^{hh} = \frac{1}{2}kz^2$ (at $z = L_w/2$). Here ΔE_g^{HH} is the heavy-hole gap difference for the two semiconductors and L_w is the well width at the barrier edge (well width of parabolic quantum well samples) and Q_{cb} is the band

offset ratio. Therefore, $k = \frac{8Q_{cb}\Delta E_g^{hh}}{L_w^2}$.

Thus, the n^{th} conduction subband energy can be expressed as

$$E_{cb}^n = \left(n - \frac{1}{2}\right) \frac{2\hbar}{L_w} \left(\frac{2Q_{cb}\Delta E_g^{hh}}{m_e^*} \right)^{\frac{1}{2}}.$$

For heavy holes in the valence band subband energy is given by

$$E_{hh}^n = \left(n - \frac{1}{2}\right) \frac{2\hbar}{L_w} \left(\frac{2(1 - Q_{cb})\Delta E_g^{hh}}{m_{hh}^*} \right)^{\frac{1}{2}}.$$

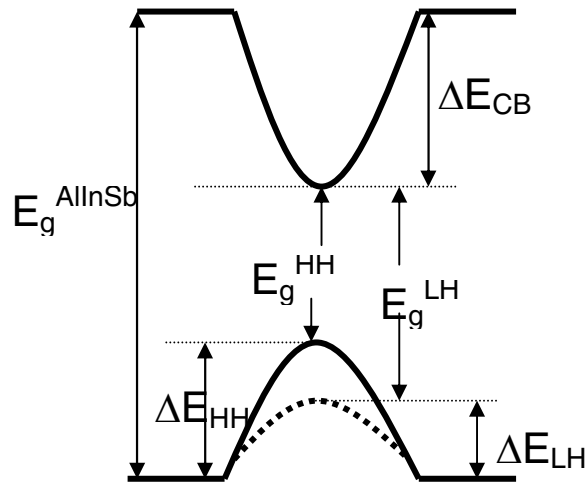


Figure 6.18: Schematic of the potential energy profile of a Parabolic Quantum Well.

6.9.1 Sample: S578

There are more confined subbands in a parabolic QW than in a square QW with the same energy well width. Sample S578 is a 50nm PQW with 9% Al in the barrier. Figure 6.19 shows the differential transmission spectra at zero magnetic field. One of the more striking characteristics of the data in Figure 6.19 is the observation of “forbidden transitions,” transitions with $\Delta n = 2$ but parity allowed [74].

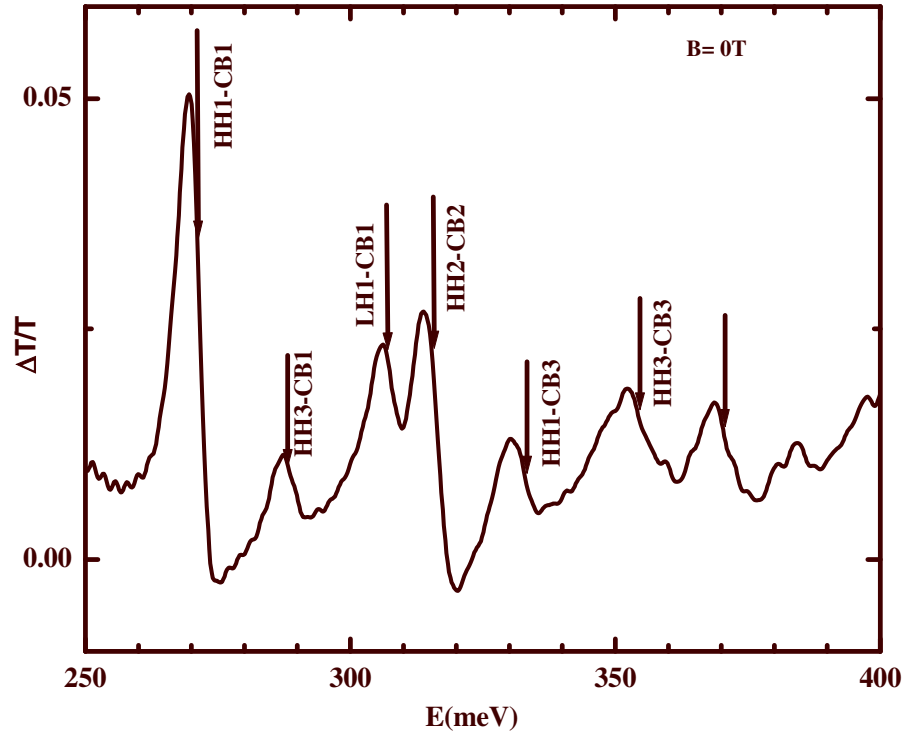


Figure 6.19: Differential spectrum measured on parabolic QW of width 500\AA and 9% Al in the alloy layer at $B = 0\text{T}$. A number of transitions, including forbidden transitions, are observed.

When we apply a magnetic field parallel to the growth direction of the PQW, the peaks exhibit an energy shift and a splitting. In Figure 6.20 the experimental peak positions are plotted versus magnetic field. Each state shows qualitatively different energy shifts. In contrast to the square well samples, data from PQW sample shows

spin splitting for the $n = 0$ HH1-CB1 state. As depicted in the Figure 6.21, at 5T the ground state splits into doublets.

Currently, we do not have a theory for the valence band structure in PQW systems. With this drawback in mind, we nevertheless tried to fit our data using the Pidgeon and Brown model which calculates transition energies for square well systems. It is clear that most of the observed features cannot be explained using this square well model. It would be very interesting to analyze the data with a more realistic calculation so that one could study the energy of various excitonic states confined in PQWs in some detail.

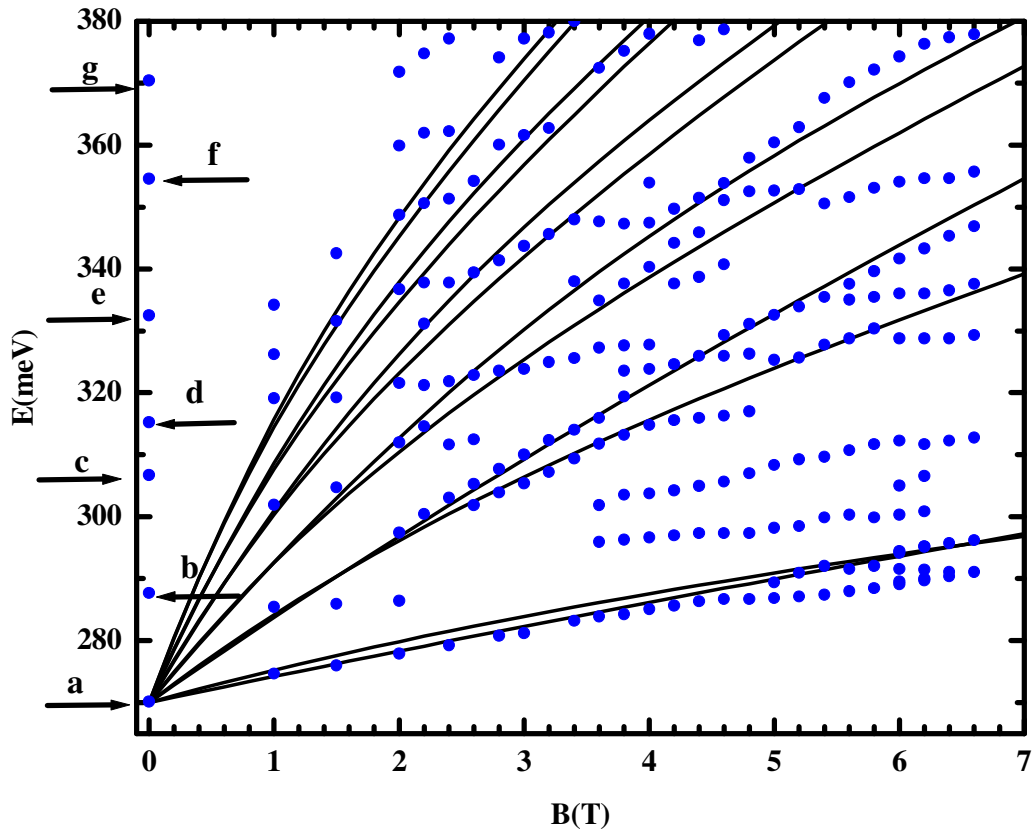


Figure 6.20: Circular marks represent the energy of the peak position from transmission spectra. Solid lines represent theoretically generated results of allowed transitions, based on the Pidgeon and Brown model. Identified excitonic transitions at zero magnetic field are marked from a to g and correspond to a: HH1-CB1, b:HH3-CB1, c:LH1-CB1, d:HH2-CB2, e: HH1-CB2, f: HH3-CB3 and g: HH2-CB4 respectively.

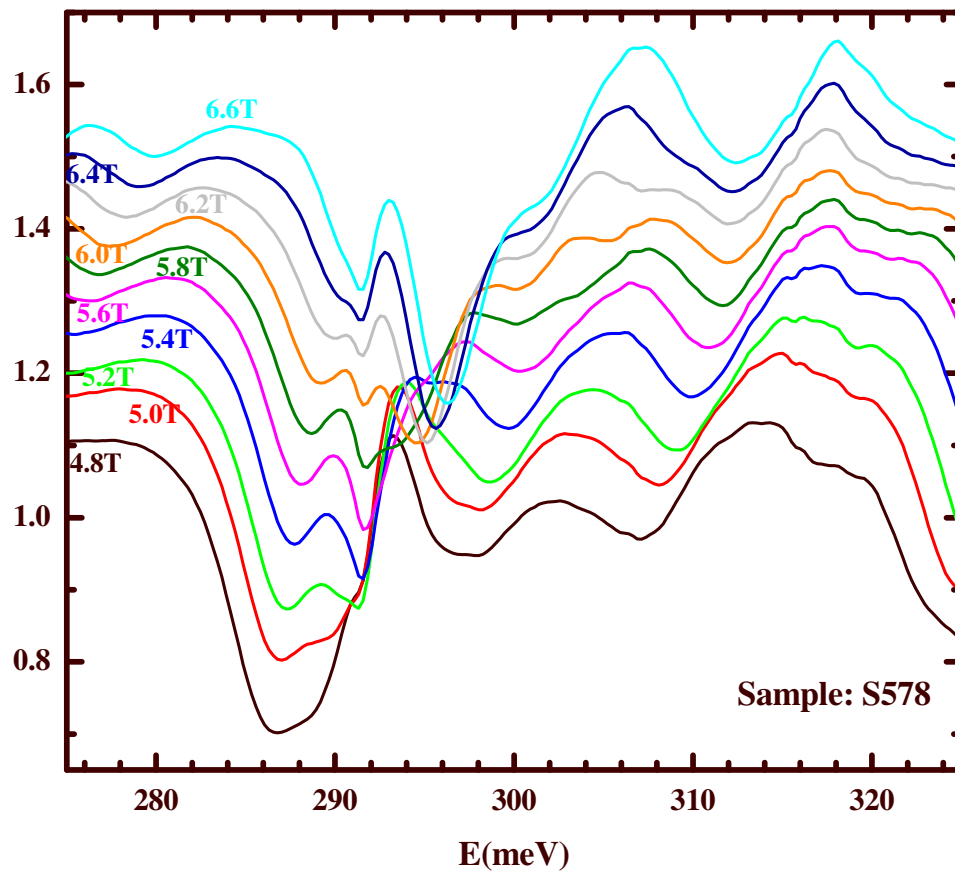


Figure 6.21: Transmission spectra for the PQW sample at various magnetic fields.

Spin splitting can be clearly seen.

Summary and Future Work

The motivation for the exciton studies was based on interest in material characterization and study of the band structure of the InSb quantum wells.

In this thesis, we have presented spectroscopic studies of InSb quantum wells using FTIR spectroscopy to probe the interband transitions. First we performed exciton measurements on InSb/AlInSb QWs with no external magnetic field. A four-band Kane model, including the strain and the nonparabolicity in our system, is used to reproduce experimental transitions. We have followed an alternate method to determine the deformation potential parameters by exploiting the different strain dependence of the light and heavy hole band edges. We find hydrostatic deformation potential parameter $a = -7.4 \pm 0.2$ eV and shear deformation potential parameter $b = -1.8 \pm 0.1$ eV and these values are closely agree with most previously reported values.

The second half of this thesis investigated optical properties of InSb-AlInSb MQW structures in a normal magnetic field. The study leads to an interpretation of optical transitions in undoped systems with different well widths and different Al composition in the barrier. In the magneto-optical investigations, the magnetoexcitons are clearly observed in the undoped MQWs, but are complicated by the band mixing effect. The field dependence of the spectral minima has been fitted within the Pidgeon and Brown model. In every sample, a reasonable agreement between the calculated and experimental results is achieved for most of the transitions. This enables us to identify most of the transitions by their predicted energy-field dependence. Moreover,

it is clear that there is no simple linear relationship between the energy shift of the peaks and the magnetic field.

However, there are some weak features in the experimentally observed spectra which cannot be explained using the current model. The possible reasons for these extra exciton spectral lines could be the strong coupling of heavy and light hole subbands or due to the strain present in the system. These features lead to a reinterpretation of existing experimental data and a more rigorous exciton model is required for a quantitative description of unidentified exciton states in the spectra. A good starting point to explore the nature of magnetoexcitons in InSb quantum wells in detail could be the Bauer-Ando theory for high magnetic fields. The Bauer-Ando formalism takes account of the effect of magnetic field together with the valence-band mixing and these authors have calculated the energy levels of magnetoexcitons in GaAs QWs in the presence of magnetic fields up to 10T within the framework of the effective mass approximation. They have shown that the mixing of the valence-band structure is important in interpreting the experimental magneto-optical results. It is the hope of this author that applying the above theoretical formalism to the InSb QWs will give a better understanding of behavior of magnetoexcitons in InSb QWs.

References

- [1] A. Oral, M. Kaval, M. Dede, H. Masuda, A. Okamoto, I. Shibasaki, and A. Sandhu, *IEEE Trans. Magn.* **38**, 2438 (2002).
- [2] J. Heremans, D. L. Partin, C. M. Thrush, and L. Green, *Semicond. Sci. Technol.* **8**, S424 (1993).
- [3] S.A. Solin, D. R. Hines, A.C.H. Rowe, J.S. Tsai, Yu. A. Pashkin, S. J. Chung, N. Goel, and M. B. Santos, *Appl. Phys. Lett.* **80**, 4012, (2002).
- [4] V.P. Kunets, W.T. Black, Yu. I. Mazur, D. Guzun, G.J. Salamo, N. Goel, T.D. Mishima, D.A. Deen, S.Q. Murphy, and M.B. Santos, *J. Appl. Phys.* **98**, 014506 (2005).
- [5] T. Ashley, A. R. Barnes, L. Buckle, S. Datta, A. B. Dean, M. T. Emeny, M. Fearn, D. G. Hayes, K. P. Hilton, R. Jefferies, T. Martin, K. J. Nash, T. J. Phillips, W. H. A. Tang, P. J. Wilding, and R. Chau, *The 7th International Conference on Solid-State Integrated Circuit Technology* (2004).
- [6] G.A. Khodaparast, R.E. Doezema, S.J. Chung, K.J. Goldammer, and M.B. Santos, *Phys. Rev. B* **70**, 155322 (2004).
- [7] H.Chen, J. J. Heremans, J. A. Peters, J. P. Dulka, A. O. Govorov, N. Goel, S. J. Chung and M. B. Santos, *Appl. Phys. Lett.* **86**, 032113, (2005).
- [8] <http://www.ioffe.rssi.ru>
- [9] N.W. Ashcroft and N.D. Mermin, *Solid State Physics*, Saunders College Publishing, Orlando, (1976).
- [10] Y.P. Varshni, *Physica* **34**, 149 (1967).
- [11] I. Vurgaftman, J.R. Meyer, and L.R. Ram-Mohan, *J. Appl. Phys.* **89**, 5815 (2001).
- [12] C. Weisbuch and B. Vinter, *Quantum Semiconductor Structures Fundamentals and Applications*, Academic Press, Inc., San Diego (1991).
- [13] E.O. Kane, *J. Phys. Chem. Solids*, **1**, 249 (1957).
- [14] S.L. Chuang, *Physics of Optoelectronic Devices*. Wiley & Sons, Inc. (1995).

- [15] Landolt-Bornstein, in Numerical Data and Functional Relationships in Science and Technology, edited by O. Madelung, Group III, Vol. **22** (Springer, Berlin, 1987).
- [16] C. Hermann and C. Weisbuch, Phys. Rev. B. **15**, 823 (1977).
- [17] G. Bastard, *Wave Mechanics Applied to Semiconductor Heterostructures* (Les Editions Physique, Les Ulis) 1988.
- [18] G. Bastard, J.A. Brum, and R. Ferreira, Solid State Physics, Volume **44**, 229 (1991).
- [19] J. Luttinger and W. Kohn, Phys. Rev. **97**, 869 (1955).
- [20] I.M. Tsidilkovski, *Band Structure of Semiconductors*, International Series in the Science of the Solid State, Volume **19**, Pergamon Press.
- [21] G.H. Wannier, Phys. Rev. **52**, 191(1937).
- [22] C.F. Klingshirn, *Semiconductor Optics*, (Springer-Verlag, Berlin, 1997).
- [23] A.H. McDonald and D.S. Ritchi, Phys. Rev. B **33**, 8336 (1986).
- [24] O. Akimoto and H. Hasegawa, J. Phys. Soc. Jpn. **22**, 181 (1967).
- [25] M. Shinada, S. Sugano, J. Phys. Soc. Jpn. **21**, 1936 (1966).
- [26] F. Stern, W. E. Howard, Phys. Rev. **163**, 816 (1967).
- [27] P.Y. Yu and M. Cardona, *Fundamentals of Semiconductors: Physics and Materials Properties* (Springer, New York, 2001), 3rd edition.
- [28] R.S. Knox, "Theory of excitons", in Solid State Physics (Academic Press, New York, 1963), Vol. supplements 5.
- [29] J. Singh, *Electronic and optoelectronic properties of semiconductor structures*, Cambridge University Press (2003).
- [30] S.J. Chung, K. J. Goldammer, S.C. Lindstrom, M. B. Johnson, and M. B. Santos, J. Vac. Sci Technol. B **17**, 1151 (1999).
- [31] K.J. Goldammer, W.K. Liu, G.A. Khodaparast, S.C. Lindstrom, M.B. Johnson, R.E Doezema and M. B. Santos, J. Vac. Sci Technol. B **16**,1367 (1998).
- [32] J.B. Bates, Science **191**, 31 (1976).

- [33] P.W. Atkins, Physical Chemistry, 5th Ed, 1994.
- [34] EQUINOX 55 User's manual.
- [35] S.W. McKnight, K. P. Stewart, H. D. Drew, and K. Moorjani, Infrared Phys. **27**, 327 (1987).
- [36] N. Dai, F. Brown, P. Barsic, G.A. Khodaparast, R.E. Doezema, M.B. Johnson, S.J. Chung, K.J. Goldammer, and M.B. Santos, Appl. Phys. Lett. **73**, 1101 (1998).
- [37] N. Dai, G.A. Khodaparast, F. Brown, R.E. Doezema, S.J. Chung, and M.B. Santos, Appl. Phys. Lett. **76**, 3905 (2000).
- [38] L. Vegard, Z. Phys. **5**, 17 (1921).
- [39] H. Nagai, J. Appl. Phys. **45**, 3789 (1974).
- [40] *PC-MRD User's Guide*, first edition, 1993, Published by Philips for use with version 1.0 of the PC-MRD Software.
- [41] D.K. Bowen and B.K. Tanner, *High Resolution X-ray Diffractometry and Topography*, Taylor & Francis Inc., 1998.
- [42] G.C. Osbourn, J. Appl. Phys. **53**, 1586 (1982).
- [43] S. S. Dosanjh, L.Hart, R. Nayak, and B.A. Joyce, J. Appl. Phys. **75**, 8066 (1994).
- [44] Z. Sobiesierski, S.A. Clark, R.H. Williams, A. Tabata, T. Benyattou, G. Guillot, M. Gendry, G. Hollinger, and P. Viktorovitch, Appl. Phys. Lett. **58**, 1863 (1991).
- [45] D.Y. Oberli, J. Shah, J.L. Jewell, and T.C. Damen, Appl. Phys. Lett. **54**, 1028 (1989).
- [46] M. C. Tamagaro, R. Hull, L. H. Greene, J.R. Hayes, and A.Y. Cho, Appl. Phys. Lett. **46**, 569 (1988).
- [47] P.J.A. Thijs, L.F. Tiemeijer, J.M. Binsma, and T. V. Dongen, Philips J. Res. **49**, 187 (1995).
- [48] E.P. O'Reilly, Semicond-Sci Technology **4**,121 (1989).
- [49] R. People, J. C. Bean, Appl. Phys. Lett. **47**, 322, (1985).

- [50] J. W. Matthews and A. E. Blakeslee, *J. Cryst. Growth* **27**, 118 (1974).
- [51] T.D. Mishima et al. unpublished.
- [52] T.Y.Wang and G. B. Stringfellow, *J. Appl Phys.* **67**, 344 (1990).
- [53] C.G. van de Walle, *Phys. Rev. B* **39**, 1871(1989).
- [54] F.H. Pollak, *Semiconductor and Semimetals*, (R.K. Willardson and A.C. Beer, eds.) Vol. **32**, Academic Press, 1990.
- [55] N. Dai, F. Brown, R. E. Doezema, S. J. Chung, and M. B. Santos *Phys. Rev.B* **63**, 115321 (2001).
- [56] F. Brown, Ph.D. Dissertation, The University of Oklahoma, 2001.
- [57] T. Kasturiarachchi, F. Brown, N. Dai, G.A. Khodaparast, R.E. Doezema, S.J. Chung, and M.B. Santos, *Appl. Phys. Lett.* **88**, 171901 (2006).
- [58] D.F. Edwards and V. J. Lazizzera, *Phys. Rev.* **120**, 420 (1960).
- [59] J.C. Mann, G. Belle, A. Fasolino, M. Altarelli, and K. Ploog, *Phys. Rev. B* **30**, 2253 (1984).
- [60] A. Petrou, G. Waytena, X. Liu, J. Ralston, and G. Wicks, *Phys.Rev.B***34**, 7436 (1986).
- [61] W. Ossau, B. Jakel, E. Bangert, G. Landwehr and G. Weimann, *Surf. Sci.* **174**, 188 (1986).
- [62] A.S. Plaut, J. Singleton, R.J. Nicholas, R.T. Harley, S.R. Andrews and C.T. Foxon, *Phys. Rev. B* **38**, 1323 (1988).
- [63] M. Potemski, L. Vina, G.E. W. Bauer, J.C. Mann, K. Ploog and G. Weimann, *Phys. Rev. B***43**, 14707 (1991).
- [64] D.C. Rogers, J. Singleton, R.J. Nicholas, C.B.T Foxon and K. Woodbridge, *Phys. Rev. B* **34**, 4002 (1986).
- [65] L. Vina, G.E.W. Bauer, M. Potemski, J.C. Mann, E.E. Mendez and W.I. Wang, *Surf. Sci.* **229**, 504 (1990).
- [66] C. R. Pidgeon and R. N. Brown, *Phys. Rev.* **146**, 575 (1966).
- [67] M.H. Weiler, R.L. Aggarwal and B. Lax, *Phys. Rev. B* **17** 3269 (1978).

- [68] C. R. Pidgeon, "Landau Level Spectroscopy" ed. G. Landwehr and E. I. Rashba, *Modern Problems in Condensed Matter Sciences*, Vol. **27. 1** (North-Holland, Amsterdam, 1991) pp.447-479.
- [69] M.W. Weiler, *Journal of Magnetism and Magnetic Materials*, **11**, 131 (1979).
- [70] Y. Iimura, Y. Segawa, G. E. Bauer, M. M. Lin, Y. Aoyagi, and S. Namba, *Phys. Rev. B* **42**, 1478 (1990).
- [71] Y. D. Jho, F. V. Kyrychenko, J. Kono, X. Wei, S. A. Crooker, G. D. Sanders, D. H. Reitze, C. J. Stanton, and G. S. Solomon, *Phys. Rev. B* **72**, 045340 (2005).
- [72] M. Sugawara, *Phys. Rev. B* **45**, 11423 (1992).
- [73] R.C. Miller, A.C. Gossard, D.A. Kleinmann, and O. Muntaneau, *Phys. Rev. B* **29**, 3740 (1984).
- [74] R.C. Miller, D.A. Kleinmann, and A.C. Gossard, *Phys. Rev. B* **29**, 7085 (1984).

Appendix A

Al Compositions from HRXRD Data

(1) 10nm Well width Samples

(a) Al composition from asymmetric measurements

Sample Name	Nominal Al %	Lattice parameters	Relaxed lattice parameter (a_L)	Percentage Relaxation	Calculated Al %
S809	8	c = 6.4514 a = 6.4498	6.4506	99.9%	8.4
S810	12	c = 6.4361 a = 6.4354	6.4358	99.9%	12.6
S812	16	c = 6.4225 a = 6.4201	6.4213	99.8%	16.8
S813	20	c = 6.4056 a = 6.4022	6.4040	99.8%	21.9

Table A1: Lattice parameters and Al compositions obtained from (-1-15) x-ray measurement for 10 nm MQW samples.

(2) 15nm Well width Samples

(a) Al composition from symmetric measurements

Sample name and nominal Al %	Diffraction Plane and sample orientation	Calculated out-of-plane lattice parameter (Å)	Average Al (%)
T018 (x = 7%)	(004), $\phi = 0^\circ$	6.4537	(a)7.7
	(004), $\phi = 180^\circ$	6.4520	
	(004), $\phi = 90^\circ$	6.4469	(b)8.6
	(004), $\phi = 270^\circ$	6.4527	
T017 (x = 10%)	(004), $\phi = 0^\circ$	6.4268	(a)9.7
	(004), $\phi = 180^\circ$	6.4652	
	(004), $\phi = 90^\circ$	6.4682	(b)9.9
	(004), $\phi = 270^\circ$	6.4209	
T016 (x = 14%)	(004), $\phi = 0^\circ$	6.4386	(a)14.3
	(004), $\phi = 180^\circ$	6.4209	
	(004), $\phi = 90^\circ$	6.4209	(b)13.0
	(004), $\phi = 270^\circ$	6.4474	
T015 (x = 17%)	(004), $\phi = 0^\circ$	6.4268	(a)17.2
	(004), $\phi = 180^\circ$	6.4138	
	(004), $\phi = 90^\circ$	6.4267	(b)16.5
	(004), $\phi = 270^\circ$	6.4176	

Table A2: Lattice parameters and Al compositions obtained from (004) x-ray measurement for 15 nm MQW samples. In the fourth column, (a) represents the average composition value determined from $\phi = 0^\circ$ and $\phi = 180^\circ$ scans and (b) corresponds to the average composition value obtained from $\phi = 90^\circ$ and $\phi = 270^\circ$ scans.

(b) Al composition from asymmetric measurements

Sample Name	Nominal Al %	Lattice parameters (Å)	Calculated Al %
T018	7	c = 6.4566 a = 6.4200	6.6
T017	10	c = 6.4460 a = 6.4140	9.7
T016	14	c = 6.4279 a = 6.4097	15.0
T015	17	c = 6.4182 a = 6.3832	17.8

Table A3: Lattice parameters and Al compositions obtained from (-1-15) x-ray measurement for 15 nm MQW samples.

(3) 20nm Well width Samples

(a) Al composition from symmetric measurements

Sample name and nominal Al %	Diffraction Plane and sample orientation	Calculated out-of-plane lattice parameter (Å)	Average Al (%)
S948 (x = 5%)	(004), $\phi = 0^\circ$	6.4592	(a)5.6
	(004), $\phi = 180^\circ$	6.4613	
	(004), $\phi = 90^\circ$	6.4650	(b)5.2
	(004), $\phi = 270^\circ$	6.4583	
S949 (x = 8%)	(004), $\phi = 0^\circ$	6.4534	(a)7.5
	(004), $\phi = 180^\circ$	6.4536	
	(004), $\phi = 90^\circ$	6.4563	(b)7.1
	(004), $\phi = 270^\circ$	6.4534	
S954 (x = 14%)	(004), $\phi = 0^\circ$	6.4268	(a)14.0
	(004), $\phi = 180^\circ$	6.4356	
	(004), $\phi = 90^\circ$	6.4327	(b)14.0
	(004), $\phi = 270^\circ$	6.4297	

Table A4: Lattice parameters and Al compositions obtained from (004) x-ray measurement for 20 nm MQW samples. In the fourth column, (a) represents the average composition value determined from $\phi = 0^\circ$ and $\phi = 180^\circ$ scans and (b) corresponds to the average composition value obtained from $\phi = 90^\circ$ and $\phi = 270^\circ$ scans.

Appendix B

Table shows the Pidgeon Brown model Hamiltonians (after Weiler (1981)) H_a and H_b

$$\left[\begin{array}{cccc}
 E_g + s[(2n+1)F + N_1 + n + 1] & \sqrt{\frac{1}{2}nsE_p} & -\sqrt{\frac{1}{6}(n+1)sE_p} & \sqrt{\frac{1}{3}(n+1)sE_p} \\
 \sqrt{\frac{1}{2}nsE_p} & -s[(n-\frac{1}{2})(\gamma_1 + \gamma') + \frac{3}{2}\kappa] & s\gamma''\sqrt{3n(n+1)} & -s\gamma''\sqrt{6n(n+1)} \\
 -\sqrt{\frac{1}{6}(n+1)sE_p} & s\gamma''\sqrt{3n(n+1)} & -s[(n+\frac{3}{2})(\gamma_1 - \gamma') - \frac{1}{2}\kappa] & \frac{1}{\sqrt{2}}s[(2n+3)\gamma' - \kappa - 1] \\
 \sqrt{\frac{1}{3}(n+1)sE_p} & -s\gamma''\sqrt{6n(n+1)} & \frac{1}{\sqrt{2}}s[(2n+3)\gamma' - \kappa - 1] & -\Delta - s[(n+\frac{3}{2})\gamma_1 - \kappa - \frac{1}{2}]
 \end{array} \right]$$

$$\left[\begin{array}{cccc}
 E_g + s[(2n+1)F - N_1 + n] & \sqrt{\frac{1}{6}nsE_p} & -\sqrt{\frac{1}{2}(n+1)sE_p} & \sqrt{\frac{1}{3}nsE_p} \\
 \sqrt{\frac{1}{6}nsE_p} & -s[(n-\frac{1}{2})(\gamma_1 - \gamma') + \frac{1}{2}\kappa] & s\gamma''\sqrt{3n(n+1)} & -\frac{1}{\sqrt{2}}s[(2n+1)\gamma' + \kappa + 1] \\
 -\sqrt{\frac{1}{2}(n+1)sE_p} & s\gamma''\sqrt{3n(n+1)} & -s[(n+\frac{3}{2})(\gamma_1 + \gamma') - \frac{3}{2}\kappa] & -s\gamma''\sqrt{6n(n+1)} \\
 \sqrt{\frac{1}{3}nsE_p} & -\frac{1}{\sqrt{2}}s[(2n+1)\gamma' + \kappa + 1] & s\gamma''\sqrt{6n(n+1)} & -\Delta - s[(n-\frac{1}{2})\gamma_1 + \kappa + \frac{1}{2}]
 \end{array} \right]$$

All band parameters have the dimensions of energy, and are defined as follows:

$$E_p = \frac{2P^2}{\hbar^2}, \quad s = \frac{\hbar e B}{m}.$$

where P is the interband momentum matrix element, B is magnetic field strength in Tesla.

F is a higher (conduction) band parameter; $N1$ and κ contribute to the conduction-band and valence band g factors respectively. F , $N1$, κ and γ are dimensionless. γ and κ are related to the parameters defined by Luttinger as follows.

$$\gamma_1 = \gamma_1^L - \frac{2P^2}{3E_g}, \quad \gamma_2 = \gamma_2^L - \frac{P^2}{3E_g}, \quad \gamma_3 = \gamma_3^L - \frac{P^2}{3E_g} \quad \kappa = \kappa^L - \frac{P^2}{3E_g}.$$

$$\gamma' = \gamma_3 + (\gamma_2 - \gamma_3)[(3 \cos^2 \theta - 1)/2]^2,$$

$$\gamma'' = \frac{2}{3}\gamma_3 + \frac{1}{3}\gamma_2 + \frac{1}{6}(\gamma_2 - \gamma_3)[(3 \cos^2 \theta - 1)/2]^2.$$

θ is the angle between (100) and the magnetic field direction and for our case $\theta = 0$.